Optimization and characterization of THz-resonant metasurfaces for enhanced light-matter coupling

by

Amber Mozes

to obtain the degree of Master of Science
at the Delft University of Technology,
to be defended publicly on Monday July 26, 2021 at 14:00.

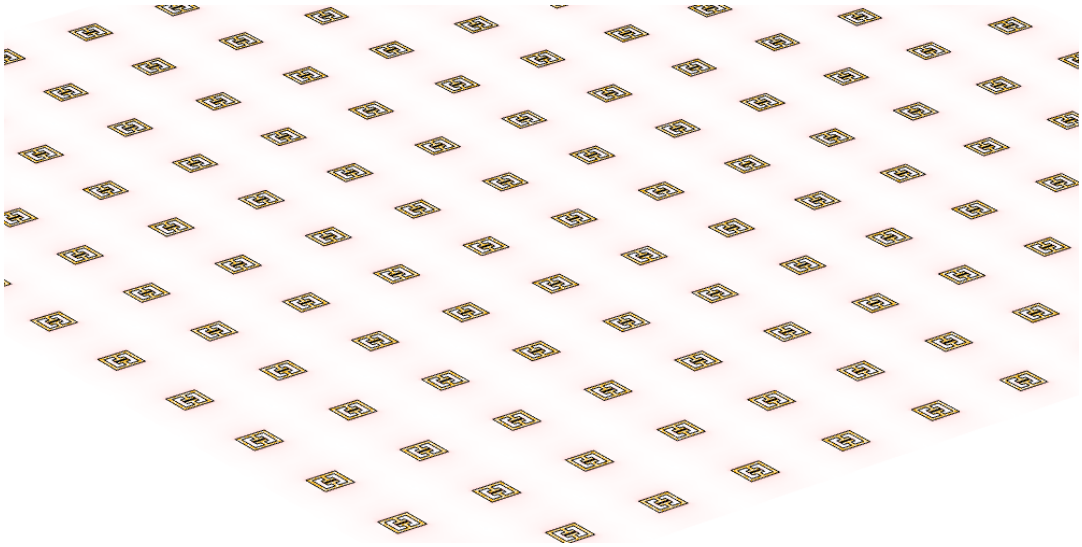

Student number:	4380045	
Project duration:	December 8, 2020 – July 26, 2021	
Thesis committee:	Dr. A. Caviglia,	TU Delft, supervisor
	Dr. T. van der Sar,	TU Delft
	Dr. A. Endo,	TU Delft
	M. Matthiesen,	TU Delft, daily supervisor

TU Delft

Abstract

Terahertz time-domain spectroscopy (THz-TDS) is an extremely useful method to probe material electrodynamics. The THz regime comprises rich physics, enabling to determine compositional, electronic and vibronic degrees of freedom through THz spectroscopy of a material under study. However, to study nanometre size thin films with THz-TDS, we need to overcome a large mismatch in length scales, since the THz wavelength is on the order of millimeters. A solution lies in the THz probing of metasurfaces, artificial materials made of conductive structures with length scales much smaller than the probing wavelength. Such a metamaterial induces enhanced electromagnetic field strengths near the surface, enabling nonlinear spectroscopy without the need for strong-field terahertz sources. Additionally, they provide sensitivity to the local (micron-scale) electrodynamic environment. In the ideal case, one can infer significant information about the thin film electrodynamics via the resonance frequency and dissipation in the metasurface.

This thesis project comprises the optimization of terahertz (THz) resonant electric split ring resonator (eSRR) metasurfaces for enhanced-light matter coupling, suitable for material characterization. Experimental characterization is combined with finite element simulations, to obtain the transmission spectra and near-field electric, magnetic fields and current densities. In simulation, the eSRR design is optimized to obtain an up to four times stronger response at resonance than the designs described in literature. The optimized design is studied on different substrates, revealing the ability to extract a resonance even close to a substrate Reststrahlen band. This thesis concludes with characterization of the metal-insulator transition of transition metal oxide $NdNiO_3$. From the resonance frequency and quality factor it is possible to track this phase transition from time-domain terahertz spectroscopy, thereby revealing the ability to probe extremely thin films, with an outlook on out of equilibrium studies.

Contents

1 Introduction **4**

I Principles of terahertz probing **8**

2 Theory of light-matter interaction **9**
2.1 Interaction with free carriers 9
2.2 Interaction with bound carriers 12
2.2.1 Interaction with phonons 12

3 Split ring resonators **15**
3.1 Frequency domain analysis of resonant response 16
3.2 Resonator equivalent circuit model 17

4 Time-domain spectroscopy: experimental methods **19**
4.1 Generation and detection 19
4.1.1 Generation 20
4.1.2 Detection 21
4.1.3 Purging 21
4.2 Experimental setup 22
4.3 Frequency domain analysis 24
4.3.1 Substrate measurements 24

5 Finite element calculations: simulation methods **26**
5.1 Maxwell equations 27
5.2 Mesh and materials 28

II Gold electronic split ring resonators **30**

6 Resonance characterization from simulations **31**
6.1 Electromagnetic response of conductive structures 32
6.2 LC resonance 33
6.3 Rayleigh resonance 34
6.4 Dipole resonance 35
6.5 Out of plane field distribution 36
6.6 Conclusion and discussion 36

7 Simulation and experiment **38**
7.1 Terahertz response of the metasurface 38
7.2 Polarization of incident electric field 40
7.3 Experimental transmission and reflection 41
7.4 Conclusion and discussion 41

III Optimizing metasurface **42**

8 Design considerations of eSRR **43**
8.1 Metasurface material and thickness . . . 44
8.1.1 Choosing a thickness . . . 44
8.2 Frequency regimes . . . 45
8.3 Packing regimes . . . 46
8.4 Conclusion and discussion . . . 47

9 Optimizing the resonant metasurface **49**
9.1 Geometry . . . 49
9.1.1 Resonator length . . . 49
9.1.2 Capacitor length . . . 50
9.1.3 Gap width . . . 50
9.1.4 Linewidth . . . 51
9.2 Rectangularity . . . 51
9.2.1 Resonator length in x direction . . . 51
9.2.2 Resonator length in y direction . . . 51
9.3 Periodicity . . . 52
9.3.1 Periodicity in x direction . . . 52
9.3.2 Periodicity in y direction . . . 52
9.4 Conclusion and discussion . . . 53

10 The optimized design **54**
10.1 LC resonance characterization . . . 55
10.2 Experimental characterization . . . 56
10.2.1 Comparison of designs . . . 57
10.3 Different substrates . . . 58
10.4 Temperature dependence eSRR on LAO . . . 59
10.5 Conclusion and discussion . . . 60

IV Probing phase transitions **62**

11 Transition metal oxide $NdNiO_3$ **63**
11.1 Perovskite structure . . . 63
11.2 Metal-insulator transition . . . 64
11.3 Control of the metal-insulator transition . . . 65

12 THz spectroscopy of $NdNiO_3$ **67**
12.1 Time-domain THz probing of MIT . . . 68
12.1.1 Frequency domain interpretation . . . 69
12.2 Metasurface probing of MIT . . . 70
12.3 Resonant response of metasurface . . . 73
12.4 Conclusion and discussion . . . 76

A Resonator fabrication and dimensions **77**

B Resonance characterization dipole at vertical incident field **78**

C Competing energy scales in transition metal oxides **79**

Chapter 1

Introduction

The field of condensed matter physics is heavily involved in characterization of material properties. We have used our knowledge of physics to engineer new materials and exploit their properties, which enabled the concept of 'technology'. Therefore, this field is not only driven by curiosity about the materials themselves, but also by the outlook on applications.

A very effective method to study complex materials is through its electrodynamics: the interaction with electromagnetic fields. Oscillating electromagnetic fields couple to elementary particles and collective modes in a material. Coupling to free carriers induces currents in the material, whereas coupling to modes enables for example vibrations or rotations of the lattice. With low-power beams, we can study the material in equilibrium. If we use powerful beams, we can excite specific modes in a material into non-linear response regimes, and even induce phase transitions [1]. The excitation happens on an ultrafast timescale, but by using ultrafast spectroscopy methods it is still possible to resolve the excitation process and determine the decay times.

In this thesis, we focus on terahertz (THz) spectroscopy. The THz regime comprises lots of physical phenomena that we can relate to compositional, electronic and vibronic material properties. Being electromagnetic waves, the properties and behavior of THz waves are governed by the Maxwell equations, just like the other waves [2]. However, due to their specific location on the electromagnetic spectrum (see Figure 1.1), THz waves are much more difficult to handle than waves adjacent to them.

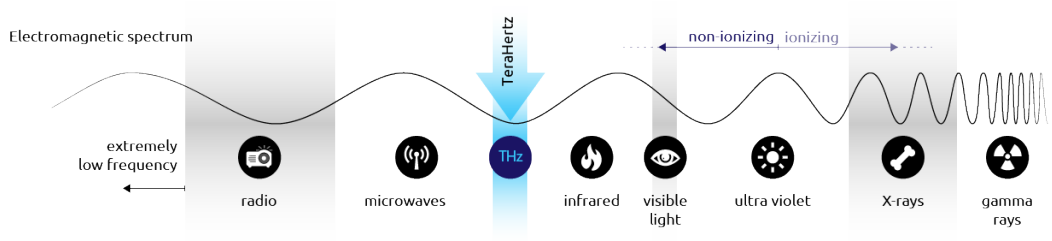

Figure 1.1: The electromagnetic spectrum. Terahertz frequencies (blue) form the middle ground between optics (right) and electromagnetics (left). The terahertz frequency band is located right between the more well-known bands of microwaves and infrared radiation. Figure from [3].

Historically, research on electromagnetic waves was divided into two different fields: optics and electromagnetics. Unfortunately, the approximations used to describe optical- or electrical waves do not always hold in the THz regime since THz waves do not fit simply into either category. New principles, new technologies, and new tools must be developed in order to generate, detect, understand and utilize THz waves.

Despite these difficulties, THz radiation also shows some promising advantages that have stimulated researchers to develop this frequency band for several applications, in our case

for material characterization. The response of a material at THz frequencies is related to absorption and dispersion at molecular level due to dipole-allowed rotational and vibrational transitions. Since these transitions are specific to the molecule, this enables spectroscopic fingerprinting in the THz range. Combined with imaging technology, inspection using THz waves provides both profile and composition information of the target. Additionaly, many physical processes take place on the energy and time scale of the THz regime, see Figure 1.2. Optical spectroscopy plays a crucial role because the relevant fundamental excitations of complex materials are spectrally accessible and the changes in the optical properties (under perturbation) are quite large [4].

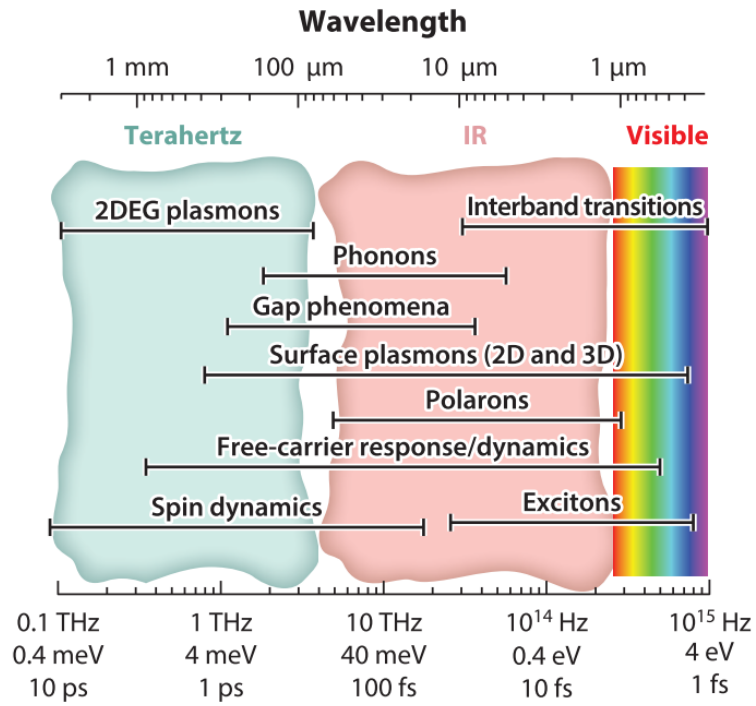

Figure 1.2: Fundamental excitations and corresponding energy and timescales of material electrodynamics in the THz range. Figure from [4].

The ultrafast spectroscopy method used in this thesis is terahertz time-domain spectroscopy (THz-TDS), measuring the electric field of pulses of electromagnetic radiation directly in the time-domain. By passage through a sample under study the propagated pulse will change in shape, see Figure 1.3. By sending a terahertz (THz) beam through a sample we can retrieve the interaction from the reflected or transmitted beam. Consequently, through Fourier analysis of the input and propagated pulses, the frequency-dependent absorption and dispersion of the sample can be obtained. Metals have high free carrier density, so sending a beam through such a material induces lots of currents. Due to this current, a large portion of the incident beam will be reflected and only little is transmitted. Dielectrics are known to be relatively transparent, and therefore transmit a lot, but also absorb quite a portion. Transparent materials will mainly transmit the beam, and therefore show little perturbation to the fields. Especially when we want to study thin films, it is difficult to extract the material response, since this also limits the length scale over which the THz beam is able to interact with a sample.

To be able to study thin films with THz-TDS, we need to overcome a large mismatch in length scales. Terahertz wavelengths are of the order of millimeters, which makes it difficult to study nanometer thick samples. Artificially engineered media known as 'metamaterials' offer a solution to this problem. Metamaterial is now a well-accepted term for an optical medium that is artificially engineered to interact with light in ways no natural materials can

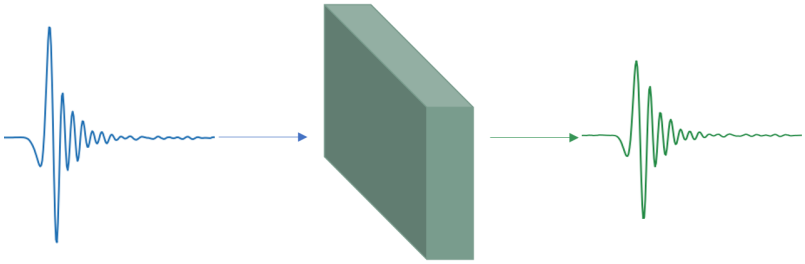

Figure 1.3: Transmission terahertz time-domain spectroscopy. We can study the properties of a thin film by studying its interaction with a short time pulse, containing frequencies in the terahertz regime. Due to interaction, the transmitted pulse (green) that propagated through our sample (green) is smaller than the incoming pulse (blue) and might change shape. We can relate these changes to the material properties of the sample.

[5]. Such a medium consists of conductive components placed in a periodic array with a lattice constant smaller than the wavelength at which interaction occurs.

Because of their sub-wavelength structuring, metamaterials do not diffract light and therefore act as a uniform medium that can be ascribed effective optical parameters. The individual components (also known as meta-molecules or meta-atoms) in the array are like the atoms of a material: structuring them in an array creates a new effective medium with optical properties that can be tuned based on the structure and materials involved. These structures can interact with electromagnetic waves exhibiting a tailored response to the electrical component of radiation that does not occur in natural materials, and provide a flexible platform facilitating observations of phenomena that would otherwise be difficult to detect. Since the materials involved have a strong impact on the resulting medium parameters, this allows us also to reversely study material properties from the behaviour of the metamaterial.

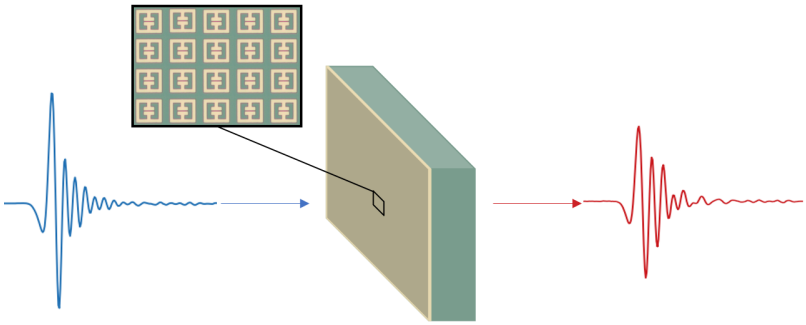

Figure 1.4: Time-domain terahertz spectroscopy of sample with metasurface. The transmitted pulse (red) is not only smaller than the incident pulse (blue), but also changed shape due to the metasurface coupling to a specific frequency that disappears from the transmitted spectrum.

This thesis focuses on the design and characterization of a specific metamaterial, consisting of electric split ring resonators (eSRR) assembled in a periodic array shown in Figure 1.4. Such a resonant metamaterial (also known as frequency selective surface) only couples to a specific frequency in the terahertz spectrum. The enhanced light-matter interaction results in a resonant decrease in transmission, characteristic of an effective permittivity and complex conductivity with a corresponding resonance frequency and quality factor. These resonant eigenmodes have strong near-field distributions confined to small volumes, shown in Figure 1.5. Consequently, they are highly sensitive to the local (micron-scale) electrodynamic environment. From changes in the resonance quality and frequency of these modes, one can therefore deduce information about the thin film which is not visible in spectroscopy of a blanket film. Furthermore, because the eigenmodes involve strongly localized fields, they open up

an avenue of nonlinear spectroscopy which is difficult to achieve with free-space methods due to the technological limitation of weak THz sources.

This resonant metasurface mode can couple to collective modes in the substrate, such as phonon modes representing a vibration of the lattice [6, 7]. Cavity control to the field of nonlinear phononics enables non equilibrium quantum optical engineering of new states of matter.

Figure 1.5: Simulated field strengths in an electric split ring resonator at resonance. Enhanced electric field (left) in the gap is a result of the induced current in the resonator arms, that oscillates in time. The magnetic response is suppressed and the magnetic field densities (right) are zero when averaged over the structure.

The resonant response is determined by the resonator geometry, periodic distribution, and material properties of both resonator and substrate underneath. If we understand the geometric contributions, we can use this to determine material parameters at the resonance frequency. I have optimized both geometry and spatial distribution to obtain a narrow resonant response for enhanced sensitivity. This narrow response leaves the rest of the frequency spectrum unaffected, such that we can simultaneously resolve excitations or collective modes within our measurement bandwidth. Also, since the eSRRs are small, a significant portion of the THz pulse is transmitted, making it possible to measure the resonant response in transmission even for very conductive materials, something which is not possible for blanket conducting films which act as mirrors. This creates an advantage for dynamical studies of (super)conducting materials.

This thesis is structured as follows: In Part I, the theory of material electrodynamics and concept of split ring resonators is introduced, after which we discuss the experimental and simulation methods carried out in this project. In the second part we characterize the resonant response of an eSRR by combining these methods. In Part III, the optimization process of the eSRR is explained and the optimized design is characterized. Finally, Part IV is dedicated to applying our metamaterial as a sensor for probing the metal-insulator transition in $NdNiO_3$.

Part I

Principles of terahertz probing

Chapter 2

Theory of light-matter interaction

In the same way that visible light can create a photograph, radio waves can transmit sound, and X-rays can see shapes within the human body, terahertz waves can create pictures and transmit information. Being electromagnetic waves, the properties and behavior of THz waves are governed by the Maxwell equations, just like the other waves [2]. Passage through a medium will perturb the THz wave, depending on the wavelength of the incident field and optical properties of the medium. From an optical point of view, the most important property of a material's response to a THz wave is its refractive index $\tilde{n} = n + i\kappa$ [2]. Propagation of a monochromatic wave through a material over a propagation distance l is described as:

$$E_T = E_0 e^{inkl} e^{-\kappa kl} \tag{2.1}$$

where E_T is the transmitted electric field strength, E_0 the incident electric field strength and k the wave number of the incident wave. The decay of amplitude and delay of phase caused by propagation through the material can be directly extracted from the imaginary and real parts of its refractive index respectively. In electrodynamics, a material's response is described by the material permittivity and permeability, and these response functions are related to optical phenomena as $\tilde{n} = \sqrt{\epsilon\mu}$. The dielectric function (or permittivity) $\epsilon(\omega)$ describes how easily an electric field can penetrate the medium, whereas the permeability μ reveals the magnetic response. Terahertz spectroscopy measures the incident and propagated electric fields to obtain the transmission, absorption and reflection from which we can extract these optical parameters.

Most materials do not have a flat spectrum throughout the entire frequency range, and there are different ways in which a terahertz wave can interact with a material. In materials with high carrier density, such as conductors and semiconductors, the interaction with free carriers will dominate. But also bound carriers are subject to interaction. At specific energy levels, corresponding to a specific frequency, resonant modes affect the optical parameters for waves whose frequency is in the vicinity of a resonance. In this chapter I will explain how these interactions affect the frequency dependent optical properties that we extract from our THz spectroscopy measurements.

2.1 Interaction with free carriers

For example in semiconductors and conductors interactions with the free carriers will dominate due to their high free-carrier density. This wave free-electron interaction can be solved using the classical Drude model. The carriers behave independent of each other with no other interaction than through collisions, which are considered to be instantaneous events. A free carrier driven by an electric wave is described by the following equation of motion:

$$m^* \frac{d^2x}{dt^2} + \frac{m^*}{\tau}\frac{dx}{dt} - qE = 0 \tag{2.2}$$

where m^* denotes effective mass of the carrier, q is the charge of the carrier, and E is the electric field [2]. When in equilibrium, the average collision time τ can be described as:

$$\tau = \frac{m^*\mu}{q} \tag{2.3}$$

where μ is the carrier mobility. The electric field induces a polarization of the material formed by carrier displacement:

$$P = (\epsilon - \epsilon_\infty)\epsilon_0 E = Nqx \tag{2.4}$$

where ϵ_∞ is the high frequency relative permittivity of the material, N is free carrier density, ϵ_0 is permittivity in a vacuum, and ϵ is the relative permittivity of the material at the frequency of the interacting electromagnetic wave, also known as the dielectric function. The equation of motion can therefore be derived to a polarization equation:

$$\frac{d^2P}{dt^2} + \gamma\frac{dP}{dt} - \frac{Nq^2}{m^*}E = 0 \tag{2.5}$$

where $\gamma = 1/\tau$ denotes the coherent decay factor of the electrons in the material. Taking the Fourier transform of an electromagnetic wave reveals that any wave can be described as the sum of a series of monochromatic waves. Therefore the interactions between wave and material can also be described as the sum of a series of monochromatic waves interacting with the material. Each individual monochromatic wave can be described as a simple harmonic oscillation $E = E_0 e^{-i\omega t}$, and the same holds for its induced polarization $P = \chi\epsilon_0 E_0 e^{-i\omega t}$, where χ is the electric susceptibility of the material defined as $\epsilon = \epsilon_\infty + \chi$. Solving the polarization equation with this knowledge results in an expression for the complex permittivity of the material at a certain frequency:

$$\epsilon(\omega) = \epsilon_\infty - \frac{\epsilon_\infty {\omega_p}^2}{\omega^2 + i\omega\gamma} \tag{2.6}$$

with

$$\omega_p = \sqrt{\frac{Ne^2}{m^*\epsilon_\infty\epsilon_0}} \tag{2.7}$$

which is called the plasma oscillation frequency (POF) of the material, proportional to the squareroot of the carrier density in the material. Metals have very high free carrier density, and therefore a POF in the UV frequency range (see Figure 2.1). The carrier density in semiconductors varies per material and for different environmental conditions such as doping and temperature. When the wave frequency is much higher than the POF of the material, the dielectric constant is real and positive and the material is transparent. On the other hand when wave frequency is lower than the POF of the material, the dielectric constant shows more complex behavior with the negative real part, and the material is opaque.

We can also express the refractive index in terms of the POF. For a non-ferromagnetic material, the magnetic permeability $\mu \approx 1$. In this case the refractive index of the material is $\tilde{n} = \sqrt{\epsilon}$. If the average collision time is much longer than the period of the electromagnetic wave ($\omega \gg \gamma$), we can approximate $\gamma \approx 0$. The complex refractive index of the material is

$$\tilde{n} = n_\infty\sqrt{1 - \frac{{\omega_p}^2}{\omega^2}} \tag{2.8}$$

where $n_\infty = \sqrt{\epsilon_\infty}$ is defined as the high frequency refractive index of the material. If the frequency of the wave is lower than the POF of the material, the refractive index has a purely imaginary value and the EM wave decays when propagating through such a material. When the wave frequency is higher than ω_p, no attenuation occurs for the propagating EM wave

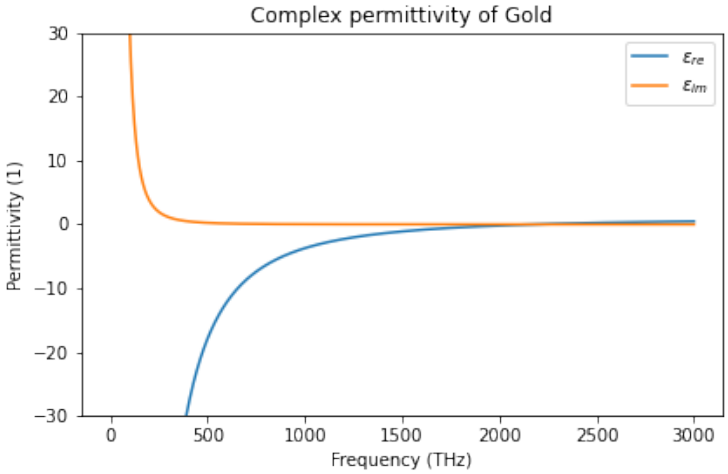

Figure 2.1: Complex permittivity of gold based on literature values [8]. Above the plasma oscillation frequency of 2.17 PHz (2170 THz) the material becomes opaque [9].

and the refractive index has a real value. Note however that the THz wave has a relatively low frequency for which $\omega \gg \gamma$ will not always be satisfied. As a result the refractive index of a material may depart from Equation 2.8.

Material interaction with THz waves is affected by carrier properties, such as density, effective mass and mobility. Therefore it is also possible to use THz spectroscopy to characterize these carrier properties in a material. For example the impedance at carrier wave frequencies that can be used for high speed devices. The complex conductivity $\tilde{\sigma}$ can be related to permittivity as:

$$\epsilon = \epsilon_\infty + i\frac{\tilde{\sigma}}{\omega\epsilon_0} \tag{2.9}$$

Combining this with Equation 2.6 gives:

$$\tilde{\sigma} = \epsilon_0\epsilon_\infty \frac{{\omega_p}^2}{\gamma - i\omega} = \frac{Ne^2\tau}{m^*(1 - i\omega\tau)} \tag{2.10}$$

When we think of conductivity, we think of transport properties in for example an electric circuit consisting of dissipative components (resistance) and reactive components (inductance, storing energy in the magnetic field, and capacitance storing energy in the electric field). The real part of the conductivity (and therefore the imaginary part of the permittivity) is responsible for dissipation through absorption of photons, and can be represented by resistance in the equivalent circuit model. The imaginary part of the conductivity has a reactive response to external fields, responsible for interactions with the magnetic field described as a kinetic inductance. In normal metals, the complex conductivity is described by the Drude model (right hand side of Equation 2.10), see Figure 2.2 for the frequency dependent conductivity of gold. The real part of the conductivity starts at its DC value at zero frequency and monotonically decreases with increasing frequency, particularly at frequencies $\omega \gg \gamma$. The imaginary part is much smaller than the real part, by a factor of $\omega\tau \ll 1$, and will show a peak near $\omega \sim \gamma$. The small value of σ_2 translates into a near zero value of the kinetic inductance of a normal metal. A metal therefore mainly displays dissipative properties through absorption of photons, that can be represented by a resistance in the equivalent circuit model. At the plasma oscillation frequency ω_p, the imaginary part of the conductivity is equal to $\omega_p\epsilon_0\epsilon_\infty$, corresponding to a zero crossing of the real part of the permittivity, responsible for the transition from a transparent to opaque material.

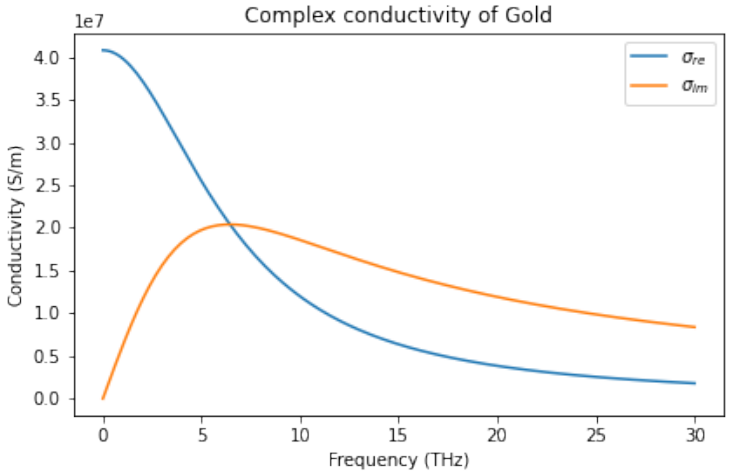

Figure 2.2: Complex conductivity of gold based on literature values [8]. For the low THz regime the real part of the conductivity is significantly larger than the imaginary part (which is usually neglected). At the collision frequency ($\omega_c = \gamma$) the imaginary part peaks and both are the same [9].

2.2 Interaction with bound carriers

Not only free carriers can be involved in wave-material interactions. Carriers which are bound by a potential barrier present discrete energy levels (according to the quantum mechanism) that play essential roles in these interactions. Each energy state involved can be considered as a simple harmonic oscillator with eigenfrequency $\omega_0 = E_0/\hbar$, where E_0 is the energy of the eigenstate and $\hbar$ is the Planck constant. The equation of motion for these resonant interactions with bounded carriers is given as:

$$\frac{d^2x}{dt^2} + \gamma\frac{dx}{dt} + {\omega_0}^2 x = \frac{q}{m^*}E \tag{2.11}$$

and Equation 2.6 becomes:

$$\epsilon(\omega) = \epsilon_\infty + \frac{\epsilon_\infty {\omega_p}^2}{{\omega_0}^2 - \omega^2 - i\omega\gamma} \tag{2.12}$$

The resulting permittivity for the material $LaAlO_3$ with bound carriers and without free carriers is shown in Figure 2.3.

The refractive index of the material is:

$$n^2 = \epsilon_\infty\left(\frac{{\omega_p}^2}{{\omega_0}^2 - \omega^2 - i\omega\gamma} + 1\right) \tag{2.13}$$

The imaginary part of the refractive index presents a peak at the resonance frequency which indicates an absorption peak of the material. When the THz wave spectroscopy is measured, one can identify those resonant energy levels through the absorption peaks. These absorption lines can then for example correspond to vibrations or rotations of the molecule.

2.2.1 Interaction with phonons

In a crystalline structure, all cells are periodically distributed in space and vibration of each cell can be coupled into collective vibration modes and presented as phonons. Acoustic phonons correspond to coherent movement of the atoms in the lattice out of their equilibrium position, whereas optical phonons are defined by out-of-phase movements of the atoms (neighbouring atoms move in opposite direction) which only exist when the unit cell consists of more than one atom. In ionic crystals, optical phonons cause fluctuations in displacement

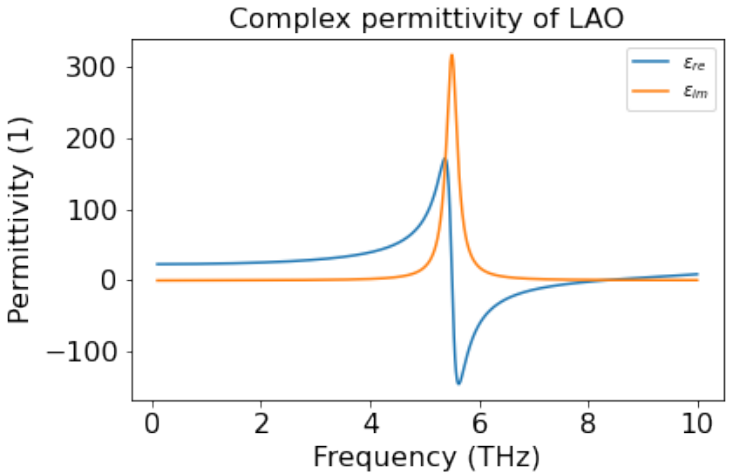

Figure 2.3: Complex permittivity of $LaAlO_3$ (LAO) based on literature values [10]. Due to a vibrational (phonon) mode at 5.51 THz, the imaginary part displays a peak corresponding to a peak in absorption.

that can create an electrical polarization that couples to the electromagnetic field. When excited by infra-red radiation, the electric field of the light will move every positive ion in the direction of the field, and every negative ion in the other direction, causing the crystal to vibrate and creating a time variant electrical dipole moment. Interaction between these phonons and light of other (larger) wavelengths can also occur indirectly through Raman scattering, giving another contribution to THz wave interactions with the material. Strong absorption occurs for waves whose frequency is close to its phonon energy, as shown in Figure 2.4.

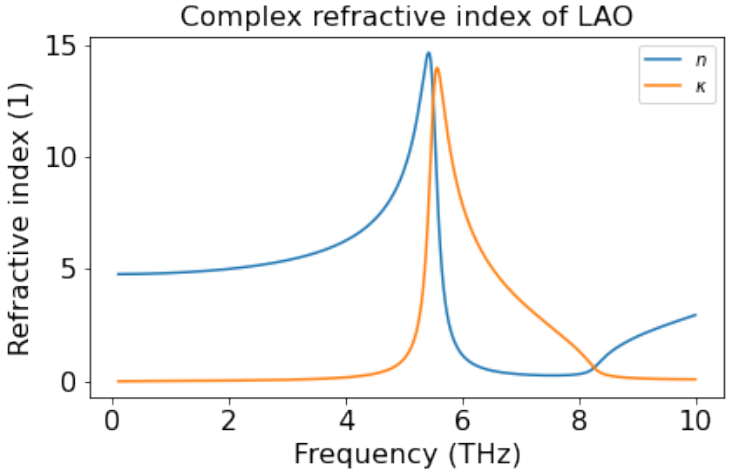

Figure 2.4: Complex refractive index of LAO based on literature values [10]. Due to a vibrational (phonon) mode at 5.51 THz, the imaginary part displays a peak corresponding to a peak in absorption.

A phonon is also defined by its displacement direction with respect to propagation. Transverse phonons vibrate perpendicular to their propagation direction and phonons where propagation travels along with the vibration direction are called longitudinal. Depending on the displacement direction, different interactions with incoming radiation occur. Therefore, the energy structure cannot only be shown from absorption spectroscopy, but also in reflection.

A crystal will show strong reflection for frequencies between the first transverse optical (TO) phonon and the first longitudinal optical (LO) phonon. This energy region is called the Reststrahlen band. The complex permittivity and refractive index of the crystal around its Reststrahlen band is:

$$\tilde{\epsilon}(\omega) = \epsilon_\infty \left(1 + \frac{{\omega_{LO}}^2 - {\omega_{TO}}^2}{{\omega_{TO}}^2 - \omega^2 - i\gamma\omega}\right) \tag{2.14}$$

The reflection spectrum will reveal a peak corresponding to the Reststrahlen band between the TO and LO phonon of the crystal.

Chapter 3

Split ring resonators

In 1999, the first version of a split ring resonator was introduced by Pendry et. al.[11]. They suggested to make a design of two thin metallic rings, disrupted at a specific location by a non-conductive gap of air or filled with a dielectric material. Such microstructures built from conducting materials show a resonant response in the gigahertz range, with a strong (in this case magnetic) response compared to most natural materials at high frequencies. Their motivation was two-fold: not only do they show that it is possible to build a magnetic material out of periodic non-magnetic structures, but this strong response also leads to strongly inhomogeneous fields inside the material which may result in local field strengths much higher than the incident field. This enables enhancement of nonlinear phenomena with reduced power requirements.

Over the years this idea was expanded to metamaterials with an electric resonant response [12, 13] and extended to interaction at terahertz [14, 15, 16] and even near-infra red [17] frequencies. A purely electric response was enabled by the development of more symmetric designs. The symmetry eliminates any magneto-optical coupling effects and yields electrically resonant structures in which the magnetic response is suppressed [12]. Our research focuses on such an electric split ring resonator (eSRR) with a resonant response in the terahertz range. The electric and magnetic field components induced by interaction with a THz pulse are shown in Figure 3.1.

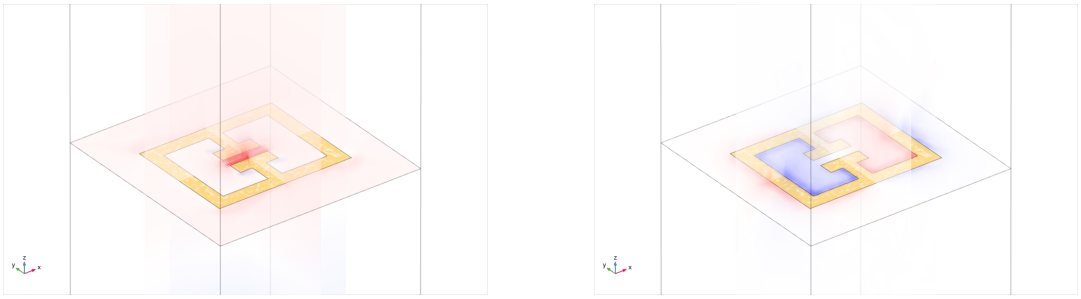

(a) E_y (b) H_z

Figure 3.1: Simulated field strengths in an electric split ring resonator at resonance. In plane vertical electric field component E_y (left) and out of plane magnetic field component H_z (right) are shown. Enhanced electric field in the gap is a result of the induced current in the resonator arms, that oscillates in time. The magnetic response is suppressed and the magnetic field densities are zero when averaged over the structure. For calculations underlying these simulations, see Chapter 5.

This type of SRR possesses a fairly high level of symmetry, belonging to the C_{2h} group, which is known to eliminate magneto-electric coupling [18]. Because the two loops are equivalent but oppositely wound with respect to the gap in the center, they act as a magnetic field gradiometer that does not couple to a uniform magnetic field [19]. A uniform magnetic field

cannot drive the fundamental resonance of this structure, whereas the incident electric field can. If our eSRR is placed in a temporally varying electromagnetic field, an electric circular current is induced in the resonator arms which in turn leads to charge accumulating across the gap in the center of the structure [16]. The electric field which builds due to the charge at the gap counteracts the circular current leading to energy stored (predominantly) in vicinity of the gap and magnetic field energy concentrated in the region enclosed by the rings.

Such a small microantenna has dimensions much smaller than the wavelength at which it resonates. The thickness of the resonator usually ranges from a few nanometer [17, 20] to tens of micrometers [19], while the planar geometry ranges from microns (for a response in the terahertz range) to millimeters at the gigahertz range. An individual resonator is therefore an order of magnitude smaller than its resonance wavelength, but by placing them in a systematic array, as shown in Figure 3.2, we can still experimentally retrieve a resonant response across a terahertz beam cross section. Even though the interaction is governed by the individual resonator, the array allows us to overcome the difference in length scale of a terahertz beam (with diameter in the order of millimeters) and the eSRR. Because of their sub-wavelength structuring, the metasurface does not diffract light and therefore acts as a uniform medium that can be ascribed effective optical parameters.

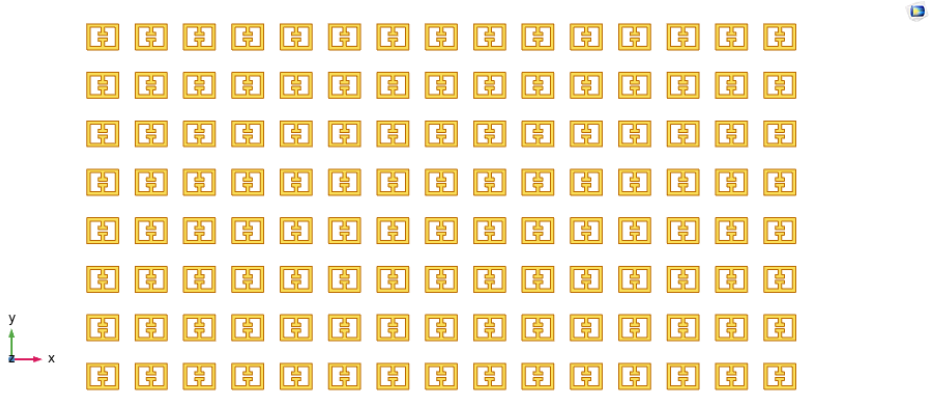

Figure 3.2: Two-dimensional array of resonators. In this work, one sample of 4x4 mm contains on the order of 12.000 resonators.

3.1 Frequency domain analysis of resonant response

The basic idea of a metamaterials response to electromagnetic fields is governed by the free charges in the resonator arms made of a conductor (in our case gold), as shown in Figure 3.3. Without an incident beam, the metal is charge neutral, but in response to an applied field the negatively charged electrons will move, due to which the metal becomes polarized [21]. Such a charge distribution is known as an electric dipole and produces a set of fields that flow from the positively charged side to the negatively charged side. A magnetic response can be obtained when the incident magnetic field fluctuates as a function of time and propagates through a loop of metallic wire. This induces a time-varying current in the conductor, giving rise to a magnetic field response. For a small enough wire, this magnetic field behaves exactly like a magnetic dipole.

The eSRRs are designed to have an enhanced response at specific frequencies in the THz range. This means that the enhancement of the electric fields, as shown in Figure 3.1, only occur at specific frequencies. We can show the resonant behaviour by studying the interaction of a THz beam with our sample through its reflection and transmission. When we study this phenomenon through spectroscopy of the frequency domain transmitted terahertz pulse, the structure's response will lead to a resonant decrease in transmission that we can relate to material electrodynamics (see Figure 3.4). The dip occurs at resonance frequency f_0, where the electrons in the metallic resonators are driven by the incident oscillating electromagnetic

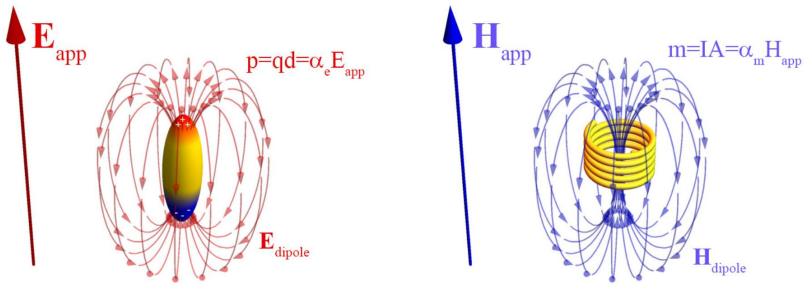

Figure 3.3: Electric and magnetic response to an incident electromagnetic field in a conductor. Figure from [21].

field.

This resonance is described by a lorentzian defined as:

$$T(f) = 1 - \frac{A}{\pi} \frac{\sigma}{((f - f_0)^2 + (\Gamma/2)^2)} \tag{3.1}$$

where A gives the amplitude, Γ the full width at half maximum (FWHM) (indicated in Figure 3.4), f stands for frequency, f_0 the resonance frequency. The Q factor is then defined as:

$$Q = \frac{f_0}{\Gamma} \tag{3.2}$$

The underlying physics of the light-matter interaction taking place can be described by the Lorentz-Drude model and is governed by interaction with the free electrons in the metal, in combination with a dielectric response coming from the substrate in the resonator gap, as explained in Section 2.1. A straightforward method to access these parameters is by describing our eSRR by an equivalent circuit model.

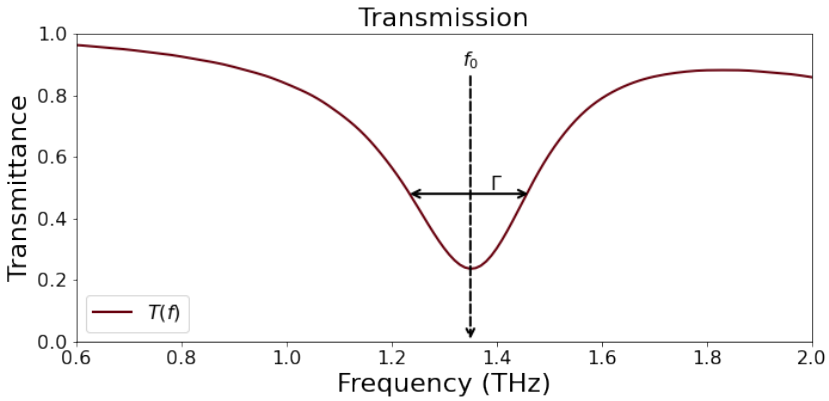

Figure 3.4: Resonant response in the frequency domain. The resonant decrease in transmission is characterized by the resonance frequency f_0 (dashed arrow) and quality factor $Q = f_0/\Gamma$. Solid horizontal arrow indicated the full width at half maximum Γ.

3.2 Resonator equivalent circuit model

Our eSRR effectively is a miniature electric circuit, driven by an oscillating electromagnetic field in the terahertz range. This circuit consists of dissipative components (resistance) and reactive components (inductance, storing energy in the magnetic field, and capacitance storing energy in the electric field). In our equivalent circuit model, the metallic contribution is

the resistance $R \propto 1/\sigma$: responsible for conductivity and dissipation, resulting in a broadening of the resonant response (hence a damping of the Q factor $Q \propto 1/R$). The substrate parameters appear in our capacitive gap $C \propto \epsilon$: the dielectric constant determines the field strength concentrated in the gap, which shows in the resonance frequency that scales with the capacitance and therefore the permittivity. The equivalent circuit is shown in Figure 3.5.

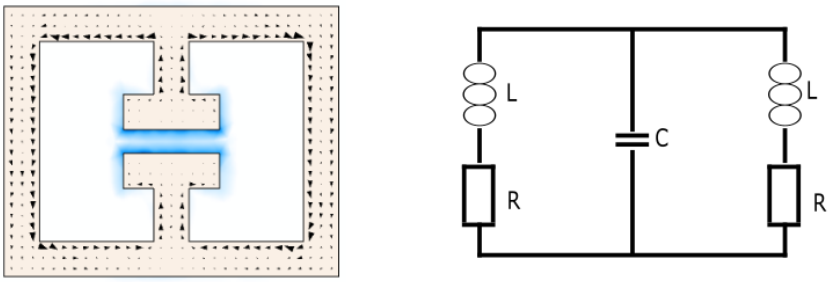

Figure 3.5: Equivalent circuit of eSRR. Left: Electric field norm at resonance (blue) and surface current density (black arrows). Right: Equivalent circuit.

From the lumped element model we can determine the metamaterial equivalent circuit components from which we can define the LC resonance. We assume that dissipation occurs mainly in the resonator arms, such that we can add a series resistance to the inductance. The total system has a combined impedance of:

$$Z = \left(\frac{2}{R + i\omega L} + i\omega C\right)^{-1} = \frac{2R + i(2\omega L - \omega^3 L^2 C - \omega R^2 C)}{(2 - \omega^2 LC)^2 + \omega^2 R^2 C^2} \tag{3.3}$$

A resonance occurs when the imaginary part of the impedance is zero with resonance frequency:

$$\omega_0 = \sqrt{\frac{2}{LC} - \frac{R^2}{L^2}} \tag{3.4}$$

The (Ohmic) quality factor is given as:

$$Q_{\text{Ohmic}} = \frac{\omega_0 L}{2R} = \frac{1}{2R}\sqrt{\frac{2L}{C} - R^2} \tag{3.5}$$

The total quality factor will be lower, since there are also radiative losses present. This makes it more difficult to directly relate the Q factor to sample properties. The total Q factor is defined as:

$$\frac{1}{Q_{\text{total}}} = \frac{1}{Q_{\text{Ohmic}}} + \frac{1}{Q_{\text{radiative}}} \tag{3.6}$$

Chapter 4

Time-domain spectroscopy: experimental methods

We obtain the THz frequency optical parameters from transmission and reflection measurements through terahertz time-domain spectroscopy (THz-TDS). This technique provides access to the complex electric field of the THz waveform. By comparing the waveform which interacts with our sample to a reference measurement of the waveform obtained from propagation through free air, it is possible to determine the complex dielectric material parameters of a sample over a broad frequency interval with a pair of measurements [22] shown in Figure 4.1. While the reference scan only consists of a single pulse, the sample waveform exhibits multiple pulses due to the later arriving multiple reflections inside such a sample. Measuring in the time domain makes it possible to either take these internal reflections into account, or leave them out of the data analysis process by only considering the first pulse.

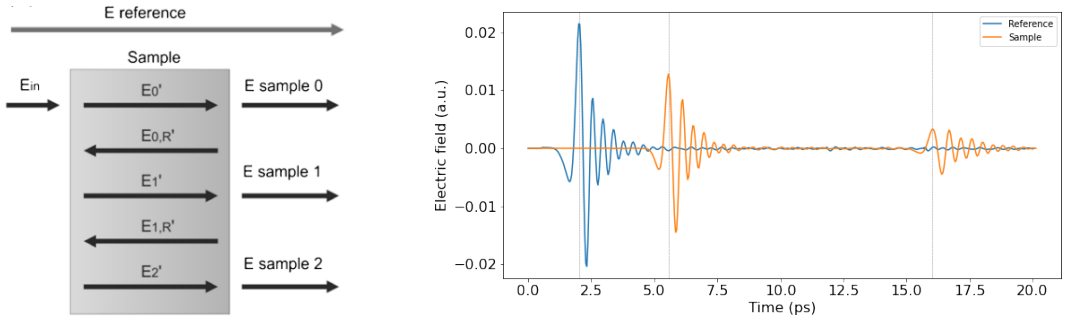

(a) Pulse propagation

(b) Measured time-domain pulse

Figure 4.1: Schematics of terahertz time-domain spectroscopy. The pulse propagating through a sample arrives a few picoseconds later with respect to a reference pulse, due to the refractive index that slows down the speed of light inside a sample. In the sample, multiple reflections occur which can be measured as well, or left out by cutting off the pulse only considering the first transmitted pulse. Figure (a) from [22].

The full experimental setup will be discussed in Section 4.2, but first the essential components for generation and detection of our terahertz pulse are explained.

4.1 Generation and detection

To be able to do spectroscopy we first need to generate a THz pulse. To do so, we use an electro-optic effect taking place in certain crystals, where due to nonlinear optical properties of the material electric fields will be emitted as further explained in Section 4.1.1. A similar effect as the one used for generation in the same crystal is exploited to then in turn detect

our pulse, now due to a linear electro-optic effect also known as the Pockel's effect. An elaborate explanation can be found in Section 4.1.2. Even propagation through air modifies the spectrum due to strong water absorption, which we can prevent by nitrogen purging methods explained in Section 4.1.3.

4.1.1 Generation

To generate terahertz, we use optical rectification. This definition refers to the development of a DC or low-frequency polarization when an intense laser beam propagates through a crystal [23]. Optical rectification is an effect that only occurs in noncentrosymmetric crystals such as ZnTe, or in centrosymmetric crystals where the symmetry is broken by a strong electric field [24]. As the excitation pulse is an ultrashort, broadband laser pulse, effectively containing many frequencies, rectification takes place between the different indident frequencies. This process is enabled by the asymmetry due to which the second order nonlinear susceptibility is nonzero, resulting in parametric processes that enable difference frequency generation. The nonlinear optical properties are described by the scalar relationships between polarization P, electric susceptibility χ and electric field E by expanding $\chi(E)$ in powers of the electric field:

$$P = (\chi_1 + \chi_2 E + \chi_3 E^2 + \chi_4 E^3 + ...)E \tag{4.1}$$

The second order term $P_2 = \chi_2 E^2$ is responsible for the optical rectification. Since we send in a short pulse, effectively containing many frequencies, rectification takes place between the different incident optical fields. Consider the second order term for two fields oscillating at frequencies $E_1 = E_0 \cos(\omega_1 t)$ and $E_2 = E_0 \cos(\omega_2 t)$, where ω_1 and ω_2 are frequencies in the optical laser pulse:

$$P_2 = \chi_2 E_1 E_2 = \chi_2 \frac{E_0^2}{2}[\cos((\omega_1 - \omega_2)t) + \cos((\omega_1 + \omega_2)t)] \tag{4.2}$$

Here, the second order nonlinear polarization consists of two terms, one at the difference frequency $\omega_1 - \omega_2$, and one at the sum frequency $\omega_1 + \omega_2$. Production of these terms is known as difference frequency generation (DFG) and second harmonic generation (SHG), respectively. For the bandwidth limited 100 fs pulses used in this work, this results in 'low' frequency radiation in the THz range. The production of THz radiation relies on DFG, and is therefore described by the first term in Equation 4.2. A schematics of the procedure is shown in Figure 4.2.

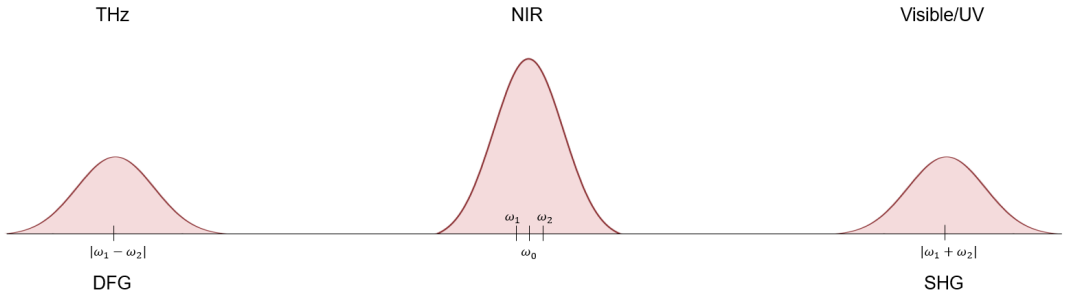

Figure 4.2: Nonlinear optical rectification of ultrashort near infrared pulse (middle) resulting in difference frequency generation (DFG, left) at terahertz frequencies and second harmonic generation (SHG, right) in the visible/UV range.

A broadband spectrum is generated if we take into account the full laser pulse, with generation between all frequencies in the pulse bandwidth, which in turn determines the THz pulse bandwidth. A maximum possible conversion efficiency is achieved when the phase matching condition is fulfilled. This means that the optical group velocity matches the THz phase velocity which ensures conservation of both energy and momentum for the DFG at THz frequencies such that conversion efficiency is enhanced. Effectively what happens is that the amplitude contributions from different positions in the crystal are in phase at the crystal

boundary and add up constructively. When the phase velocity of the THz wave matches the group velocity of the optical pulse, the generated radiation will add up constructively at each point along the direction of propagation. The electrooptic crystal ZnTe used in this work naturally has a refractive index that matches 800 nm Ti:sapphire pulsed laser source group velocity to THz range phase velocity.

4.1.2 Detection

The same electro-optic medium can be used for a reverse process for the time-domain sampling of the THz electric field after it has interacted with the sample. In this case, the THz pulse is sent through a ZnTe crystal together with an optical pulse travelling at the same speed. Due to the linear electro-optic effect (or Pockel's effect), an incoming THz electric field leads to a change in the polarization state of a co-propagating optical detection pulse (the 'sampler') [25], shown in Figure 4.3.

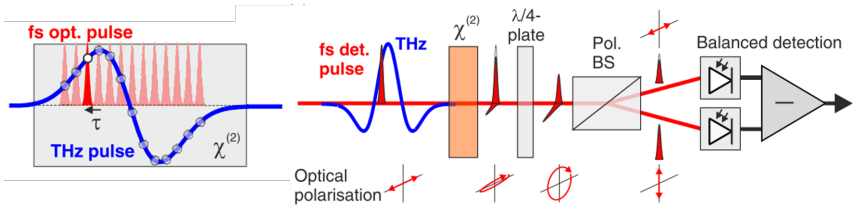

Figure 4.3: Sampling procedure. Figure from [25].

The THz electric field induces an instantaneous birefringence in the crystal, i.e. a difference in the refractive indices along each crystal axis. This perturbs the polarization of the sampler. A linearly polarized sampling pulse becomes elliptically polarized due to the induced phase modulation, depending on the THz strength. The induced ellipticity is detected by a Wollaston prism (WP) which converts the elliptically polarized probe into two beams [26]. A quarter waveplate in front of the WP makes sure that the difference between the two beams is zero when the THz signal is absent. A nonzero signal is then related to the difference between the beams which carries the information about the ellipticity. The intensity modulation is detected by balanced photodiodes, which allows complex measurement containing both phase and amplitude information.

Since the laser pulse used for sampling is still short compared to the period of the THz wave, it is possible to resolve the THz field as a function of time. Compared to the optical field the THz field is almost constant for several tens of optical periods (if the phase matching is still fulfilled) [24], which means that the ellipticity can be related to a specific time point. By delaying the sampling pulse with respect to the THz pulse, different points in time can be resolved. The detection of such a time resolved THz pulse is subject to a lot of noise. Since we are measuring a picosecond signal on a femtosecond interval, no photodiode is able to directly resolve such a short pulse. The introduction of a lock-in amplifier is therefore the next crucial step in our detection process, shown in Figure 4.4. The actual measurement of one time point of the THz electric field involves many pulses. By alternatingly sending through a sampler pulse with and without accompanying THz pulse, we are able to generate a signal that is switching between high (when both THz pulse and sampler are detected) and low (without the THz pulse) at a frequency set by the time-interval between pulses. The sampling pulse is sent through every ms, accompanied by the THz pulse every 2 ms. A lock-in amplifier filters out everything except the 500 Hz signal, such that the amplitude of this signal can be interpreted as the phase modulation due to the THz field.

4.1.3 Purging

Because terahertz radiation is absorbed by water, propagation of the pulse through air will modify our spectrum. Strong water lines appear, which are due to absorption of photons at energies corresponding to vibrations or rotations of water molecules. To prevent this from

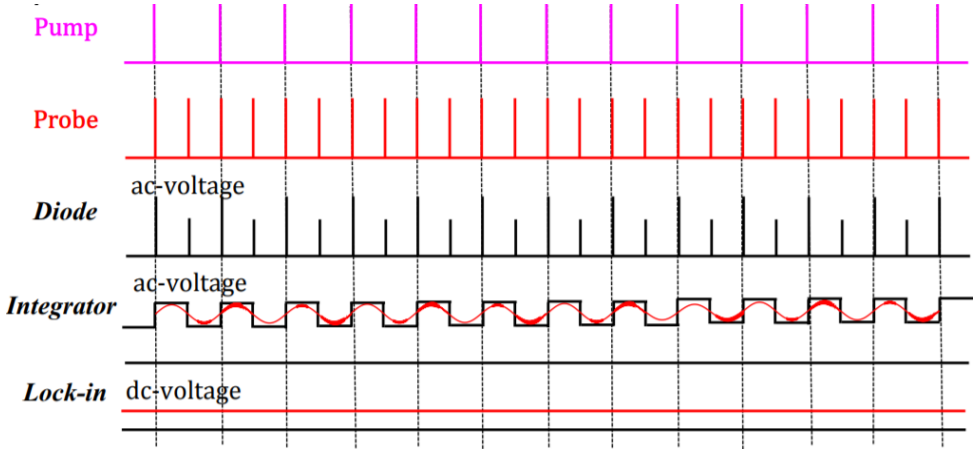

Figure 4.4: Lock-in procedure. The terahertz pulse (pump, pink) is sent to the diodes every 2 ms, whereas the sampler (probe, red) is detected every ms. The diodes read an AC voltages that is high when the THz pulse is detected and low without THz pulse. An integrator 'holds' the received signal until for 1 ms until the next signal arrives. This alternatingly high and low signal is interpeted as a 500 Hz sine wave by the lock-in, whose amplitude encodes the phase modulation. Figure from [27].

interfering with our measurements, we contain the terahertz beam in a closed box filled with nitrogen. This purging procedure lowers the humidity inside the box, which we can track with a sensor. Already in the time-domain we see a large difference in intensity of the electric field, as shown in Figure 4.5.

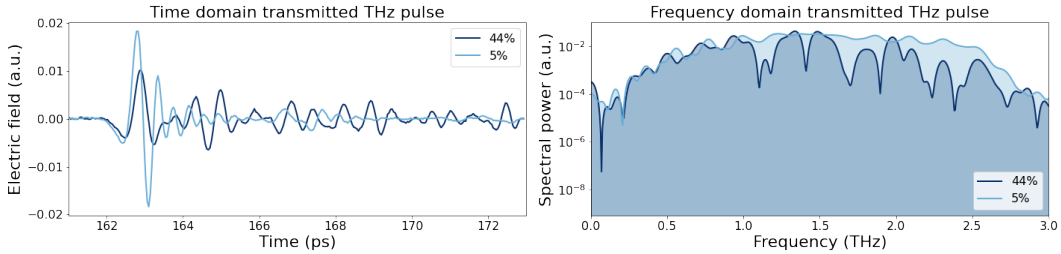

Figure 4.5: Humidity traces. Strong water absorption lines at 1.1, 1.7, 2.3 and 2.7 terahertz may appear in the spectra due to finite humidity left after purging

4.2 Experimental setup

The full optical setup, designed and constructed during my thesis project, is shown in Figure 4.6. We start with one near infrared beam (800 nm) from the Ti:sapphire laser. The beam is split into two paths: one to generate terahertz which will be sent through the sample, and one serving as the optical detection beam also known as the 'sampler'. The beams are aligned such that the optical paths travelled by the individual beams are equally long before arriving at the detection crystal where they meet. Only then the beams will overlap, travelling at the same velocity through the detection crystal to enable the detection process.

The terahertz path is sent through an optical chopper, letting the beam pass every 2 ms. A $\lambda/2$ waveplate and polarizer determine the polarization of the incoming beam. The polarizer makes sure only one polarization can pass, whereas the waveplate determines the (main) polarization of the incoming NIR beam. This polarized beam is sent through the first ZnTe crystal for terahertz beam generation. After generation, the beam is collimated and sent through our sample. The sampler beam is polarized along the axis of the terahertz

beam, such that it moves along the axis of induced birefringence when passing through the detection crystal.

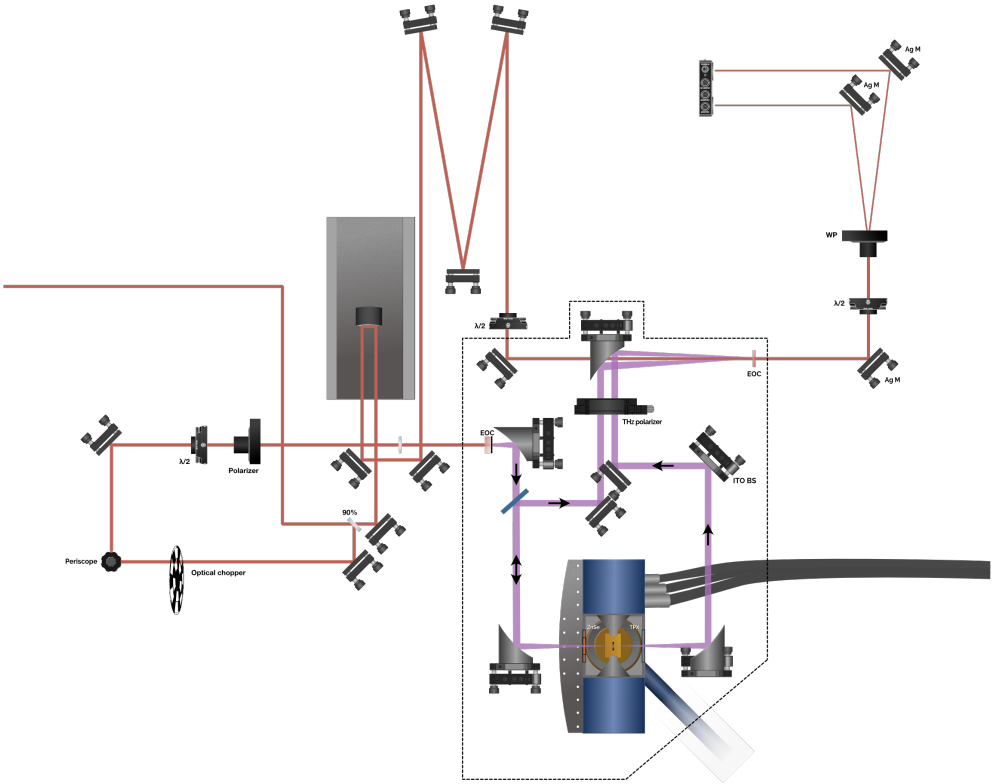

Figure 4.6: Our pump-probe scheme for terahertz time-domain spectroscopy. The incoming NIR beam (red) coming from the laser is split by a 90% beam splitter into the terahertz path (bottom) and sampler path (right). The terahertz path first passes through an optical chopper, $\lambda/2$ waveplate and polarizer. This polarized beam is sent through the first ZnTe crystal for terahertz beam (purple) generation. After generation, the beam is collimated by the parabolic mirror, passes through a Si 50% beam splitter and reaches the sample after the next parabolic mirror. The reflected beam follows the same path backwards, and is directed to detection by the Si beam splitter. Both transmitted- and reflected beams are converged onto the detection crystal, where they meet with the optical sampler probe. The sampler passes through a movable retroreflector (grey rectangle), that sets the delay of the sampler with respect to the terahertz beam, enabling time-domain resolved measurements.

Our setup is suitable for both transmission- and reflection measurements that can be executed simultaneously. The polarization of the incoming terahertz beam can be tuned by the $\lambda/2$ waveplate followed by the polarizer. The transmitted beam is directed by an ITO crystal that will reflect the terahertz beam, but transmits NIR. This is useful for possible pump-probe experiments or situations in which it is desirable to simultaneously perform THz spectroscopy and, say, polarimetry with a NIR beam, making it possible to also detect the NIR pump. Our sample is contained in a Montana cryostat, that enables us to measure at low temperatures down to 20 K.

4.3 Frequency domain analysis

A more detailed investigation of our sample requires more sophisticated approaches to extract material parameters than just time domain analysis. This is done most efficiently in the frequency domain by taking the Fourier transform, as shown in Figure 4.7. The interaction between a terahertz wave and sample is described by the spectral transfer function $h(\omega)$. This transfer function is defined as the ratio of the Fourier transforms of the sample measurement $E_s(\omega)$ and the reference measurement $E_{\text{ref}}(\omega)$ [22]. The useful frequency range of this method is determined by the duration of the initial pulse and by the time resolution of the detection process [28]. Smaller time steps in the detection process and reduction in the width of the generated electromagnetic pulse both lead to an increase in the available frequency range. This way, it is possible to analytically derive material parameters, independent of the actual THz waveform which was used for measurements. The frequency resolution is determined by the length of the time domain pulse. A conventional method to increase the frequency resolution is by zero padding. The time pulse is elongated by adding zeros before the actual time pulse [29].

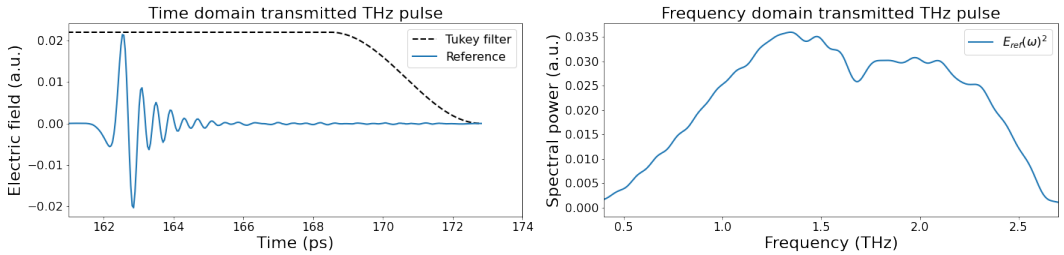

Figure 4.7: Frequency domain analysis of reference pulse. Zeros are padded in the time-domain before the actual pulse to elongate the number of points for a higher resolution in the frequency domain. The pulse is filtered by a tukey filter to make sure the first and last time point are zero. The reference pulse sets the frequency bandwidth in the terahertz range. Small dip in transmission at 1.7 THz corresponds to water lines as described in Section 4.1.3.

4.3.1 Substrate measurements

The transmittance $T(\omega) = |t(\omega)|^2$ is obtained from the transfer function for spectroscopy in transmission $t(\omega)$ through a dielectric slab of thickness d and complex refractive index $\hat{n}$, given as:

$$t(\omega) = \frac{E_s(\omega)}{E_{\text{ref}}(\omega)} = |t(\omega)|e^{i\phi(\omega)} = t_{ij}t_{ji}\exp\left[i\frac{\omega d}{c}(\hat{n}_j - \hat{n}_i)\right]F_{iji}(\omega) \tag{4.3}$$

where i and j denote free space and the sample, respectively [30], and shown in Figure 4.8. At normal incidence, the Fresnel transmission and reflection coefficients are given as $t_{ij} = 2\hat{n}_i/(\hat{n}_i + \hat{n}_j)$ and $r_{ij} = (\hat{n}_i - \hat{n}_j)/(\hat{n}_i + \hat{n}_j)$.

The Fabry-Perot term describes reflections within the slab and is (also for normal incidence) given as:

$$F_{iji}(\omega) = \sum_{p=0}^{P}\left[r_{ji}^2\exp\left(i\frac{2\hat{n}(\omega)\omega d}{c}\right)\right]^p \tag{4.4}$$

where the upper limit P of the series is set by the number of internal reflections recorded in the time-domain data. To extract the refractive index for a slab of arbitrary thickness d, we need a model for $\hat{n}$ to compare it with experiment or use methods to calculate $\hat{n}$ numerically. Only in the limit of an exceedingly thick ($P = 0$) or thin ($P = \infty$) film, we can successfully invert Equation 4.3 to obtain analytical expressions for $\hat{n}$.

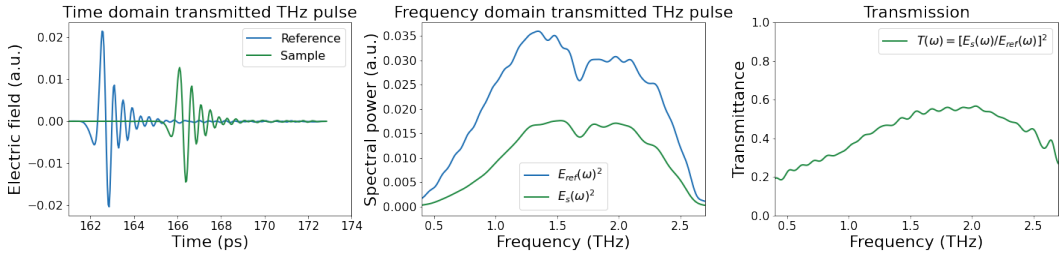

Figure 4.8: Analysis in the frequency domain of 500 um substrate sample (Al_2O_3) in transmission. The water line at 1.7 THz disappears from the spectrum when we divide by the reference pulse.

In the thick film limit for a sample with minimal absorption in the relevant frequency range such that we can assume $\kappa \ll n$, the Fresnel transmission coefficients can be approximated as real numbers. In that case the real part of the refractive index is given by the phase of the complex transmission:

$$n(\omega) = 1 + \frac{c}{\omega d}\phi(\omega) \tag{4.5}$$

and the absorption coefficient is:

$$\alpha(\omega) = -\frac{2}{d}\ln\frac{|t(\omega)|}{|t_{ij}t_{ji}|} \tag{4.6}$$

From which we derive the imaginary part of the refractive index as:

$$\kappa = \frac{\alpha c}{2\omega} = \frac{\alpha c}{4\pi f} \tag{4.7}$$

At intermediate optical thickness one obtains a series of maxima and minima in the transmitted power as the frequency is varied, separated by $\Delta f = \frac{c}{2nd}$ [31], shown in Figure 4.9. This phenomenon can be utilized to determine the dielectric properties of thin films or transparent media.

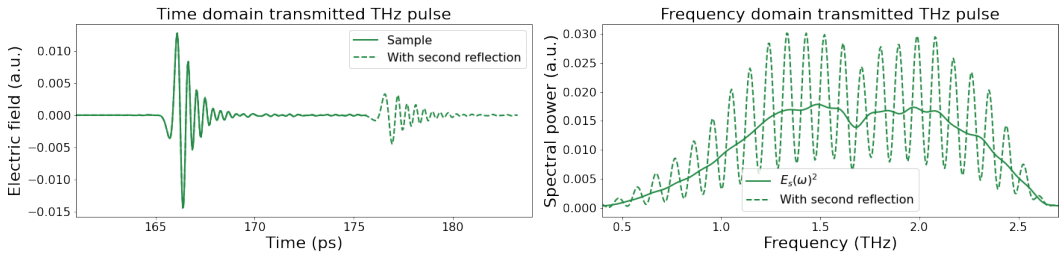

Figure 4.9: Including the second reflection in the analysis results in a series of maxima and minima in the transmitted power, separated by $\Delta f = \frac{c}{2nd}$.

Chapter 5

Finite element calculations: simulation methods

Simulations in COMSOL Multiphysics enables characterization and optimization of our eSRR design. This program enables simulation of transmission spectra and field- and current densities. We can use this to understand the light-matter interactions governing a resonant response, and to extract the field strength of the induced electric field at resonance. Apart from the additional information obtained on electric near-fields not available in experiment, another advantage is the time consumption. Whereas optimization from experimental results would require us to fabricate many metasurfaces, in simulation we can optimize by just changing individual geometric parameters. Therefore, this numerical approach gives us access to the electric near-fields and current densities, and saves a lot of time.

COMSOL Multiphysics uses finite element methods to calculate solutions to the frequency domain form of Maxwell's equations describing light-matter interaction. As a result we obtain the electric- and magnetic fields and S-parameters corresponding to scattering processes taking place at an interface or throughout a medium of finite thickness. The simulation domain is shown in Figure 5.1.

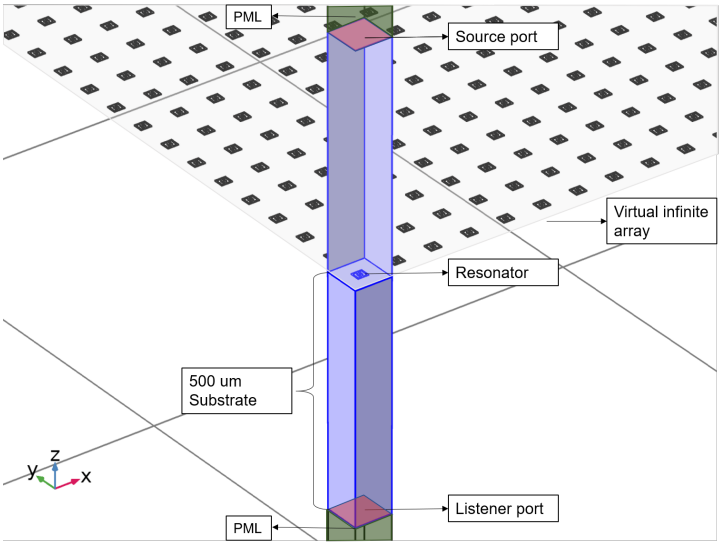

Figure 5.1: Simulation domain in COMSOL. One unit cell containing one resonator is modeled with periodic boundary conditions simulating an infinite 2D array. Perfectly matched layers (PML) at the top and bottom of the unit cell (above the source port and below the listener port) absorb the excited and higher order modes.

As mentioned before, our sample consists of tens of thousands of resonators that are

periodically distributed in an array, with geometric length scales of micron size and a 200 nm thickness. Modeling our resonators in a periodic configuration can become quite complex and time-consuming. To minimize computation time, we only simulate a single resonator (or one unit cell) and implement periodic boundary conditions in x- and y-direction assuming an infinite array of identical resonators. The incoming terahertz wave is defined at the source port and detected at the listener port. These port boundary conditions automatically determine the reflection and transmission characteristics in terms of S-parameters.

5.1 Maxwell equations

The electric wave-equation solved in the simulated domain is given as:

$$\nabla \times \frac{\nabla \times \mathbf{E}}{\mu_r} - k_0^2 \Big(\epsilon_r - \frac{i\sigma}{\omega \epsilon_0}\Big)\mathbf{E} = \mathbf{0} \tag{5.1}$$

with $\mathbf{E}$ the electric field vector, μ_r the relative permeability, k_0 the wave number in free space, ϵ_r the relative permittivity, σ the conductivity, ω the angular frequency, ϵ_0 the free space permittivity. Throughout the domain, different boundary conditions (B.C.) are implemented, as shown in Figure 5.2. From top to bottom:

In a perfect electric conductor (PEC, white), implemented at the top of the simulation domain, no electric fields can penetrate:

$$\mathbf{n} \times \mathbf{E} = \mathbf{0} \tag{5.2}$$

with $\mathbf{n}$ the normal vector.

At the source port (P_1, red) we define the incident wave orientation and retrieve the S-parameters for reflection:

$$S_{P_1} = \frac{\int_{\partial\Omega} (\mathbf{E} - \mathbf{E}_1) \cdot \mathbf{E}_1}{\int_{\partial\Omega} \mathbf{E}_1 \cdot \mathbf{E}_1} \tag{5.3}$$

with $\mathbf{E}_1$ the electric field component at the boundary.

The resonator is implemented as a transition boundary (T). This enables us to simulate the nanometer thick domain without using nanometer size meshing. This saves us a lot of computation time without losing any physics. At the transition boundary the surface current densities $\mathbf{J}_s$ are described by the surface impedance Z_s and transition boundary impedance Z_t and electric field E_t as:

$$\mathbf{J}_{\text{s,up}} = \frac{Z_s \mathbf{E}_{\text{t,up}} - Z_t \mathbf{E}_{\text{t,down}}}{Z_s^2 - Z_t^2} \tag{5.4}$$

$$\mathbf{J}_{\text{s,down}} = \frac{Z_s \mathbf{E}_{\text{t,down}} - Z_t \mathbf{E}_{\text{t,up}}}{Z_s^2 - Z_t^2} \tag{5.5}$$

where the subscript up and down stands for upside and downside of the transition boundary respectively.

At the listener port (P_2, red) we retrieve the S-parameters for transmission:

$$S_{P_2} = \frac{\int_{\partial\Omega} \mathbf{E} \cdot \mathbf{E}_2}{\int_{\partial\Omega} \mathbf{E}_2 \cdot \mathbf{E}_2} \tag{5.6}$$

with $\mathbf{E}_2$ the electric field component at the boundary.

The scattering boundary condition (S, green) ensures no reflections take place at the bottom of the simulation domain:

$$\mathbf{n} \times (\nabla \times (\mathbf{E})) - ik\mathbf{n} \times (\mathbf{E} \times \mathbf{n}) = 0 \tag{5.7}$$

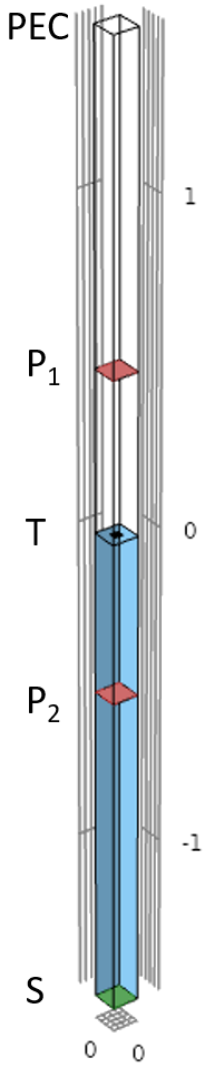

Figure 5.2: B.C.

Periodic boundary conditions are used in the x- and y-direction (in this case Floquet boundary conditions) to make sure that no interruption takes place between source (src) and destination (dst) origin. These boundary conditions are applied to the faces parallel to our resonator unit cell. The wavenumber is parametrically swept while solving for eigenvalues (frequency) at each interval [32]. The source origin is defined by k-vector of the incoming wave defined at Port 1, and Floquet boundary conditions are used fulfilling:

$$\mathbf{E}_{\text{dst}} = \mathbf{E}_{\text{src}} \exp\left[-i\mathbf{k}_F \cdot (\mathbf{r}_{\text{dst}} - \mathbf{r}_{\text{src}})\right] \tag{5.8}$$

$$\mathbf{H}_{\text{dst}} = \mathbf{H}_{\text{src}} \exp\left[-i\mathbf{k}_F \cdot (\mathbf{r}_{\text{dst}} - \mathbf{r}_{\text{src}})\right] \tag{5.9}$$

where $\mathbf{k}_F$ is the Floquet wavenumber with orientation taken from the incident field defined at periodic Port 1.

5.2 Mesh and materials

Mesh and materials are shown in Figure 5.3. Only one unit cell containing a single resonator is modeled with periodic boundary conditions to simulate an infinite 2D array. THz waves come in at port 1, with the incoming field polarized along the y-axis if not further specified. Detection takes place at port 2 which is positioned at the substrate boundary. To prevent multiple reflections, the surface beneath the port is also assumed to be of the substrate medium, different to the experimental method. We can still relate these simulations to the measurement by considering only the thin resonant layer by dividing out substrate effects.

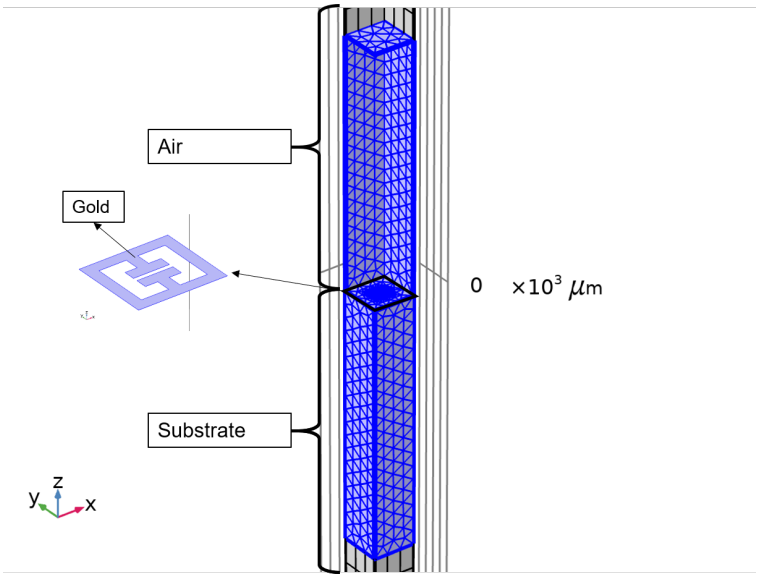

Figure 5.3: Mesh and materials. Mesh inside domains are tetrahedral with triangular boundaries. The bottom half of the simulation domain is assumed to be of the substrate material, top half is air. The inset shows the gold resonator.

All simulations (except for the substrate dependence) are based on gold resonators (conductivity $4.09{\cdot}10^7$ S/m [33]) with a sapphire substrate (n=3.31, α=1.8 cm^{-1} [34]). During experimental characterization, I realised that the sapphire parameters are different from the literature values I used. But since the simulations are executed assuming the substrate has no frequency dependence, this makes it easier to relate changes in resonance to geometric factors. The frequency dependence of the conductivity of gold is also neglected in simulation for the same reason. The actual conductivity will be lower at high frequency (see Figure 2.2).

A fine mesh avoids artificial discontinuities in electric fields, which could give rise to false etalons, but at the cost of long computation time. This is due to the large wavelength of high

frequency radiation (1 THz corresponds to 300 um wavelength) compared to the nm scale resonator thickness. Unless specified otherwise, oscillations in the transmission spectrum are due to artifacts. Since the design considerations are mainly focused on the resonant behaviour, such artifacts are neglected such that we can still obtain the relevant relative behaviour with reasonable computation time.

Part II

Gold electronic split ring resonators

Chapter 6

Resonance characterization from simulations

The functionality of any metamaterial is largely determined by the properties of the substrate and the structural details of the resonators [12, 13]. Since their introduction, split ring resonators have undergone many design variations to accommodate particular applications. These different designs however also ask for different explanations of the resonances observed [35]. One of the main goals of this thesis project is to optimize our eSRR design for enhanced light-matter coupling. Before changing the geometry, I want to characterize the first design provided by my supervisor to further understand the physics taking place at resonance, and to be able to later on see to what extent my optimized design shows a different response. Only then we can relate this response to electrodynamic properties of the materials involved.

Simulations in COMSOL allow us to study the near-field electrodynamics through local electric and magnetic field strengths, and the induced transport through the surface current density. This teaches us about the origin and strength of the resonances. By comparing between designs in literature and throughout this thesis, we can test our equivalent circuit model and relate the resonance frequency and quality to geometric- and material properties.

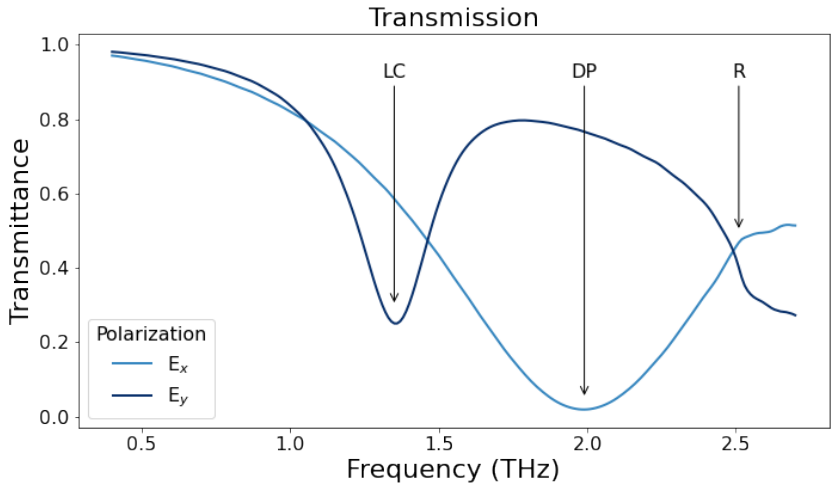

Figure 6.1: Transmission spectrum. Arrows indicate LC resonance (LC), dipole resonance (DP) and Rayleigh resonance (R). Polarization of the incident electric field is indicated in the legend (left bottom).

The transmission spectrum is shown in Figure 6.1. Split ring resonators display two fundamental resonances, known as the LC (discussed in the introductory chapters) and dipole resonance. A third resonance, the Rayleigh resonance, becomes relevant for substrates with

moderate to high refractive indices $n > 3$. These resonances each couple to the electric field, but have different physical origins. The LC resonance is a result of the individual resonator, whereas the dipole and Rayleigh resonance (often named higher order modes) are a result of the periodically distributed conductive components.

We are interested in using the LC resonance for material characterization, but understanding the presence of other resonances remains relevant. Overlapping resonances may result in distortion of the net metamaterial response, or cause mutual resonance coupling [36, 37]. Especially when the resonances are similar in oscillator strength, the total metamaterial response will be greatly affected by their coupling. This effect usually degrades the quality factors, distorts the resonances into non-Lorentzian forms, and even shifts the resonances from their intended positions. Terahertz SRR-based metamaterials usually suffer from fairly low Q factors on the order of 1-10, aggravating the problem of resonance overlap [38]. Apart from mutual resonance coupling, another reason is that we want to be able to resolve material's collective modes, such as phonons, that lie within our frequency bandwidth, but do not overlap with the LC resonance.

To understand how the higher order modes come about, it is necessary to look into the electromagnetic response of conductive structures in general. If we understand the underlying physics, we can interpret the resonant response from the near-field electric and magnetic field strengths. The electromagnetic response of periodically distributed conductive structures is explained in Section 6.1, after which the electric and magnetic near-field- and surface current densities of the LC, Rayleigh and dipole resonance are characterized. Section 6.5 shows the out of plane field distribution for each resonance.

6.1 Electromagnetic response of conductive structures

Individual strips of metal become polarized in response to an applied field, as described by Figure 3.3, and the left hand side of Figure 6.2. If such strips of metal are organized in an array, the charges are separated roughly by a distance equal to the strip length l and the applied voltage integrates over the spacing between the elements d. We then see that a conducting element is polarized in an applied field, and that a metamaterial formed of such elements will have a positive permittivity (or dielectric constant) that relates directly to the self-capacitance of the structure induced by this collective mode. Any change to the geometry will change that capacitance, and thus change the effective polarization and dielectric constant of the composite.

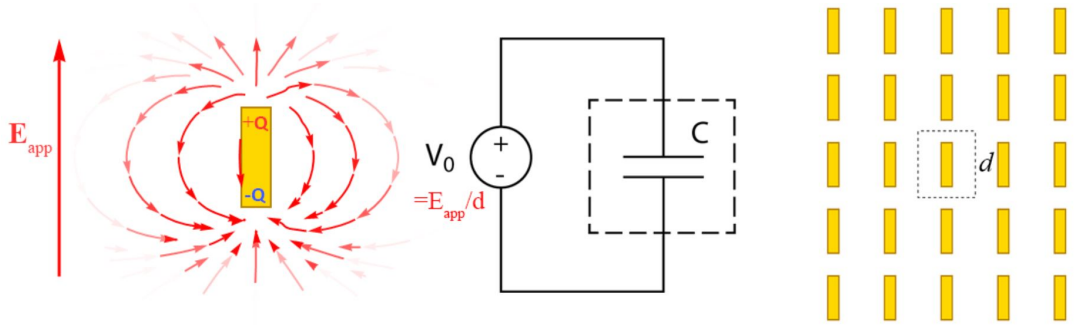

Figure 6.2: Effective self capacitance of array of metallic strips. Figure from [21].

The resonances observed in our eSRR can be related to these induced charge flows, based on the coupling to specific orientations of the incident field. The LC resonance for example only couples to an incident electric field perpendicular to the capacitor gap, and is caused by oscillating currents in the loops and charge accumulation at the gap. The (higher frequency) dipole resonance persists for each polarization, and is caused by interactions between the SRR sides or components parallel to the incident electric field [39, 40]. The Rayleigh resonance also couples to the resonator arms parallel to the electric field, but scales with the lattice

constant of the array (periodicity $p_{x,y}$) rather than the resonator arm length [41, 42]. The design and its dimensions are shown in Figure 6.3 and Table 6.1, respectively.

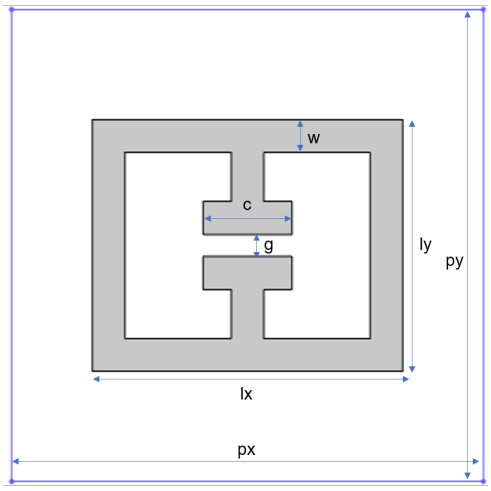

Figure 6.3: Resonator geometry.

Parameter	Symbol	Length (um)
Resonator length	lx	23.7
	ly	19.2
Capacitor length	c	6.8
Gap width	g	1.7
Linewidth	w	2.5
Periodicity	px, py	36
Thickness		0.05

Table 6.1: Dimensions of the resonator.

6.2 LC resonance

The identification of the LC resonance was first established by Linden et al [9]. The electric field norm and out of plane magnetic field components are shown in Figure 6.4. In the capacitor gap, an electric field builds up that is higher than the incoming field, while the total magnetic field is zero when averaged over the surface. Therefore, the capacitive component is the one that couples strongly to the electric field, whereas the inductive loops do not [19]. The strong magnetic out of plane component is a result of the high current density in the resonators, following the right-hand rule.

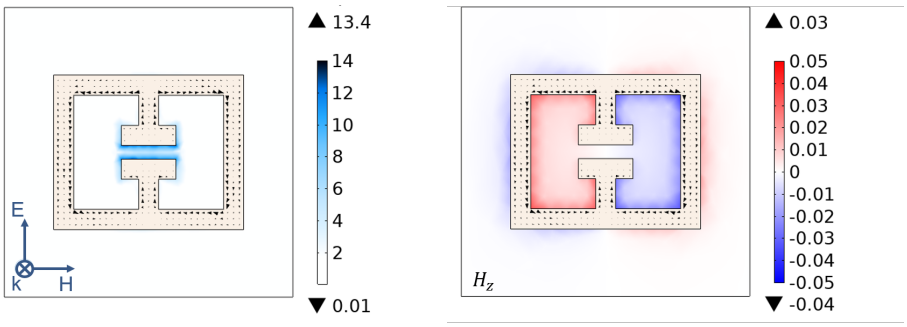

Figure 6.4: Simulation of electric field norm, surface current density and out of plane magnetic field at the LC resonance (1.35 THz).

The resonance frequency is determined by both the capacitive and inductive components, as described by the equivalent circuit model discussed in Section 3.2. It is possible to describe this resonance by a lumped element model, since the resonator size is much smaller than the resonant wavelength. Resonant response is achieved by mimicking an LC oscillator consisting of a magnetic coil (the loop) with inductance L, and a capacitor (the gap) with capacitance C.

The electric field components are shown in Figure 6.5. The incident light can couple to the LC resonance if either the electric field vector has a component normal to the plates of the capacitor, or the magnetic field vector has a component normal to the inductance (the

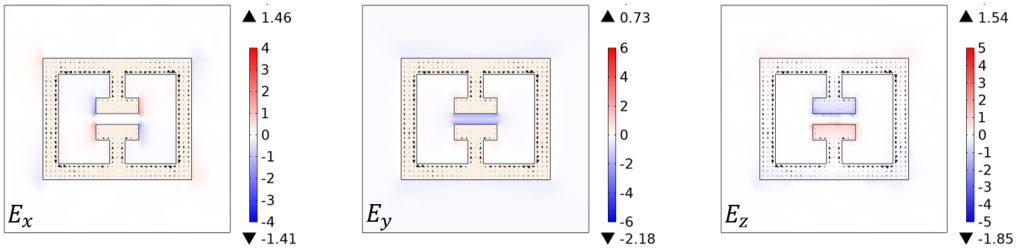

Figure 6.5: Simulation of electric field in x, y and z direction, and surface current density at the LC resonance (1.35 THz). The x and y components are evaluated at the metasurface, whereas the z component is evaluated 10 nm below the surface in the substrate (the out of plane components are zero at the transition boundary corresponding to the resonator).

plane of the coil). Our resonators couple to the electric field that comes in vertically, normal to the capacitor plates, resulting in an electric response.

6.3 Rayleigh resonance

The Rayleigh resonance is a direct result of the effective self capacitance of an array of metallic strips as shown in Figure 6.2. This resonance corresponds to the frequency at which the first diffraction order into the substrate changes from an evanescent to a propagating one [42]. This type of oscillation is called Rayleigh or Wood anomaly [41]. Its frequency is independent of the geometrical structure but depends solely on the period of the SRR unit cell and the refractive index of the medium on either side of the SRR [43].

From the electric field norm and out of plane magnetic field (Figure 6.6) we see that this resonance is weaker than the LC resonance in terms of built up electric fields at the surface, and comes with only a small induced current density. The separate electric field components however show a strong resonant response with maximums twice as strong as the LC resonance. For horizontally incident electric field, the Rayleigh resonance appears merely as a kink in the frequency spectrum at 2.51 THz. For the sake of brevity, the horizontal Rayleigh resonance is left out of this discussion.

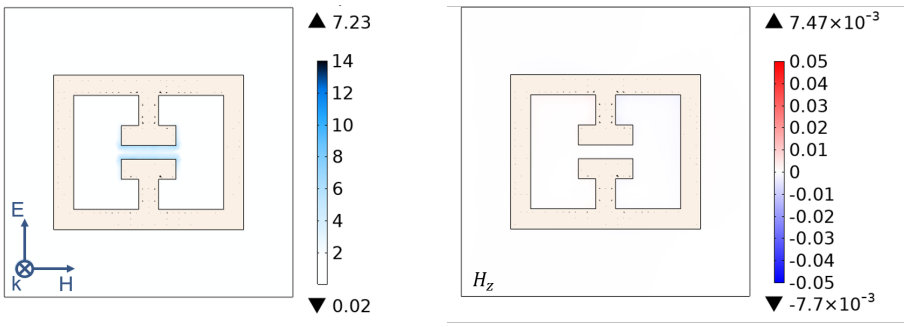

Figure 6.6: Simulation of electric field norm, surface current density and out of plane magnetic field at the Rayleigh resonance (2.51 THz).

The resonance frequency corresponds to the periodicity as:

$$\lambda_0 = n_{\text{sub}} \cdot p_y \tag{6.1}$$

As the spatial periodicity is an unavoidable property of metamaterials, this resonance is an intrinsic property of composites, which cannot be avoided by the decreasing the size of the unit cell [39]. However, the mode is sensitive to the length scales involved in the sense that the resonance becomes weaker for decreasing resonator size [42].

The electric field components shown in Figure 6.7 seem rather similar to the LC resonance, except for the z-component which shows a strong polarization in the vertical resonator arms not observed for the LC resonance. With respect to the field strengths at frequencies adjacent to the Rayleigh resonance, a maximum in electric field strengths is observed and a minimum in magnetic field strength. The electric field components are much stronger than for the LC resonance, but the field norm is much smaller due to the symmetry in positive and negative fields.

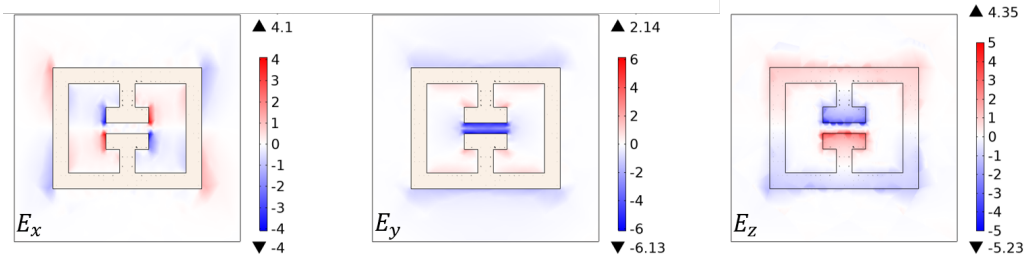

Figure 6.7: Simulation of electric field in x, y and z direction, and surface current density at the Rayleigh resonance (2.51 THz). The x and y components are evaluated at the metasurface, whereas the z component is evaluated 10 nm below the surface in the substrate (the out of plane components are zero at the transition boundary corresponding to the resonator).

6.4 Dipole resonance

The dipole resonance is a reoccurring mode at multiples of the resonator arm length. These resonator modes, i.e., standing surface plasmon waves along the nanowire axis, exist whenever an integer of half the surface plasmon wavelength equals the wire length [40]. At the dipole resonance, a current is induced in the polarization direction of the incoming electric field. This is also an electric resonance, resulting in the buildup of electric field at the edges of the arms and a magnetic field around the arms following the right-hand rule (Figure 6.8).

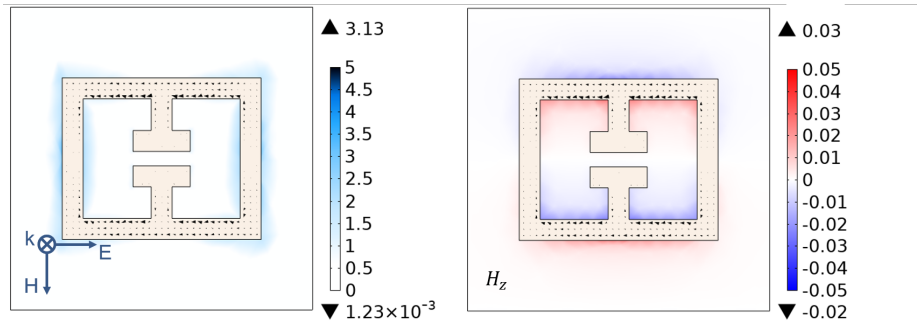

Figure 6.8: Simulation of electric field norm, surface current density and out of plane magnetic field at the dipole resonance (horizontal polarized incident electric field) (1.96 THz).

The electric field components are shown in Figure 6.9. Whereas the Rayleigh resonance corresponds to a maximum in electric fields strength with respect to adjacent frequencies, the dipole resonance shows a minimum in electric field strengths compared to the adjacent frequencies of this resonance.

Due to the mirror symmetry of the structure with respect to the polarization of the incident field, the internal field has to be in phase at both arms of the eSRR such that the reflected fields have an equal phase along the arms [42, 44]. All modes must have a non-vanishing even number of nodes (2,4,6,...) to meet the required symmetry. The first mode corresponds to the x-polarized dipole mode:

$$\lambda_0 \approx 2 \cdot n_{\text{sub}} \cdot l_x \tag{6.2}$$

The response resembles results obtained in elongated nanowires, which form plasmonic resonators [40]. More specifically, the modes found in SRRs correspond to the lowest-order modes of such a plasmonic resonator [42].

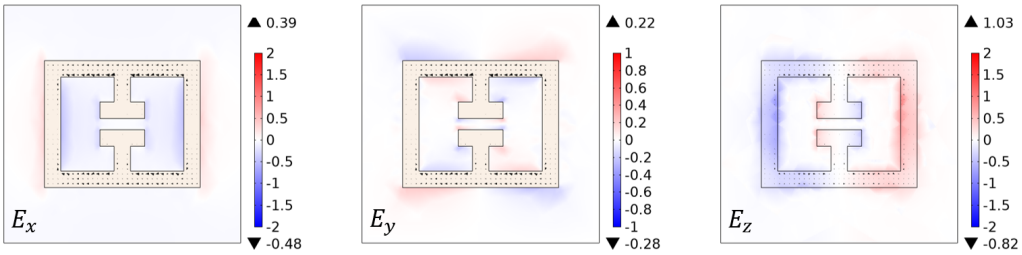

Figure 6.9: Simulation of electric field in x, y and z direction, and surface current density at the dipole resonance (horizontal polarized incident electric field) (1.96 THz). The x and y components are evaluated at the metasurface, whereas the z component is evaluated 10 nm below the surface in the substrate (the out of plane components are zero at the transition boundary corresponding to the resonator).

We would expect the dipole resonance to be visible for both polarizations, following Equation 6.2 (with l_x for x-polarization, l_y for y polarization). For a vertical incident electric field, this would correspond to a resonance at 2.31 THz. When studying the near-field electrodynamics (see Appendix B for the fields of the dipole resonance at vertical orientation), it is clear that this resonance persists for both polarizations, but in the transmission spectrum shown in Figure 6.1 the decrease in transmission is not clearly resolvable. This might be a result of the overlap in resonance or mutual resonance coupling with the Rayleigh resonance, or solely due to the fact that the resonance is weaker for shorter arm length [42].

6.5 Out of plane field distribution

In Figure 6.10 the near-field electric field components of the three resonances described above are shown. Even though the resonances are induced in the metasurface, the fields extend in to the substrate. The induced electric field extends up to a few micron into the dielectric, and for the Rayleigh resonance even up to 30 micron. From the figure we can also see that the LC resonance is the strongest. The LC resonance is sensitive to thin film properties with up to tens of micron thickness [45].

6.6 Conclusion and discussion

In this chapter, we have established the near-field and current density at the metasurface on resonance. We distinguish three types of resonances. The LC resonance, described by the equivalent circuit model in Section 3.2, is a resonance from the individual eSRR. These dimensions are much smaller than the wavelength, and therefore we can describe only this resonance by a lumped element model. The higher order modes are array properties that become weaker for larger periodicity. The Rayleigh resonance is an anomaly caused by the periodicity of the array, and depends on periodicity of the eSSRs and permittivity of the substrate.

The dipole resonance occurs due to current flow in the resonator arms parallel to the incident electric field, and therefore mainly depends on resonator arm length and substrate permittivity. Overlap between dipole and LC resonance may distort the LC resonance into a non-lorentzian shape, and would result in lower quality factor. The electric field norm at LC resonance shows an enhancement in field, stronger than the incident field. In the optimization

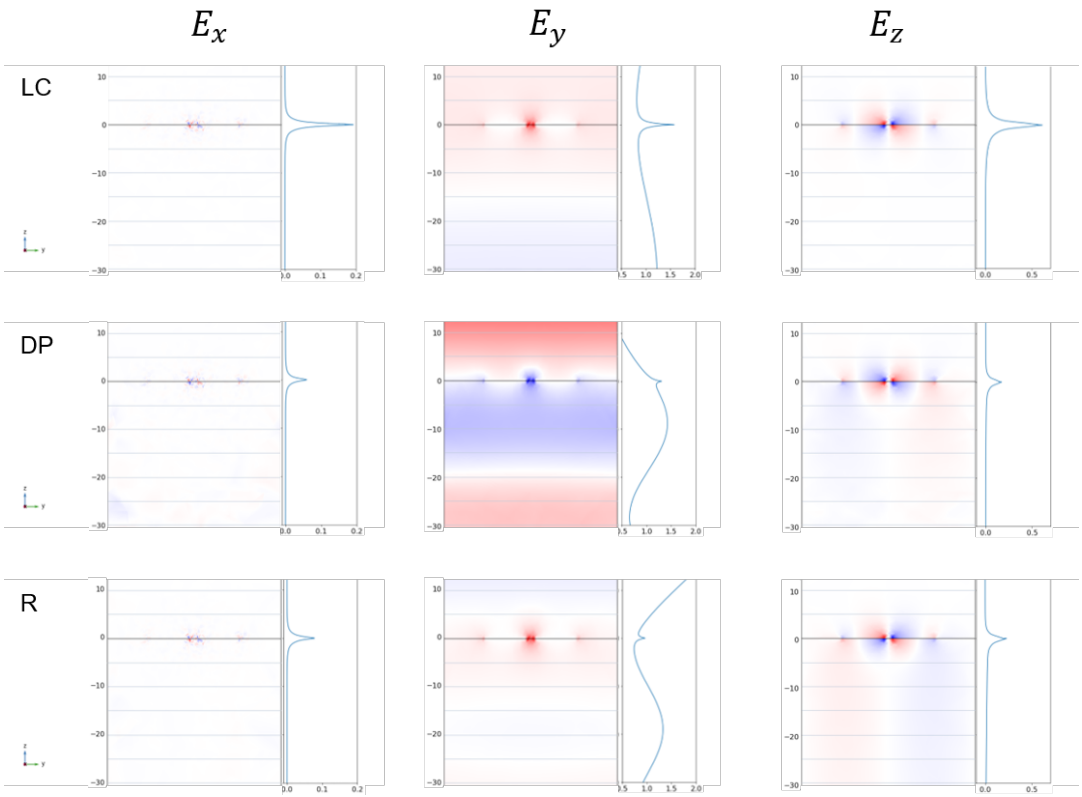

Figure 6.10: Decay of electric field components into the substrate at resonance for y-polarized incident electric field. Vertical axis shows the distance in um with respect to the resonator plane at z=0. Horizontal axis gives the surface integrated electric field components, normalized by the incident field.

process, we want to maximize the field norm at resonance, and minimize overlap between LC and dipole resonance.

I am aware that defining the higher order mode visible for the vertical incident electric field as the Rayleigh reonance is contradictory to the interpretation of for example Reference [38], where this mode is defined as the dipole resonance, but my interpretation does not stroke with the results of this paper (these results can also be explained by a lattice mediated coupling instead of the assumed dipole mode).

Chapter 7

Simulation and experiment

An important factor in the optimization process is to verify the agreement between simulation and experiment. Only if the simulations and measurement agree, it is useful to optimize in simulation. The disadvantage of experiment over simulation is the time consuming resonator fabrication and measurement procedure. In addition, simulations provide the near-field electric and magnetic field strengths. However, the simulations can only be provided for known material parameters, whereas the experimental results provide insight on unknown materials. Therefore, combining simulation and experiment enables us to verify geometric parameters of the resonators from comparing measurement and simulation of known materials, which we can use to then determine the material parameters of unknown materials and for dynamical studies.

The measurements are performed in the terahertz time-domain spectroscopy setup described in Part 1. A photograph of the sample studied in this chapter is shown in Figure 7.1a, with an optical microscope image in Figure 7.1c. From the microscope image, I derived the geometrical parameters of these resonators to use in the simulations.

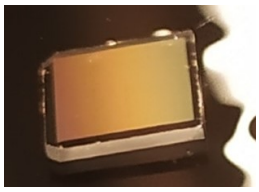

(a) Picture of sample

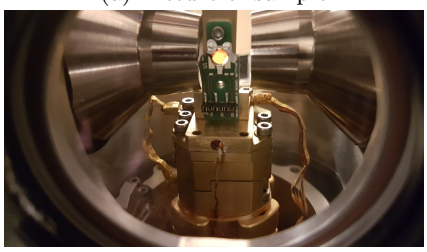

(b) Sample mounted

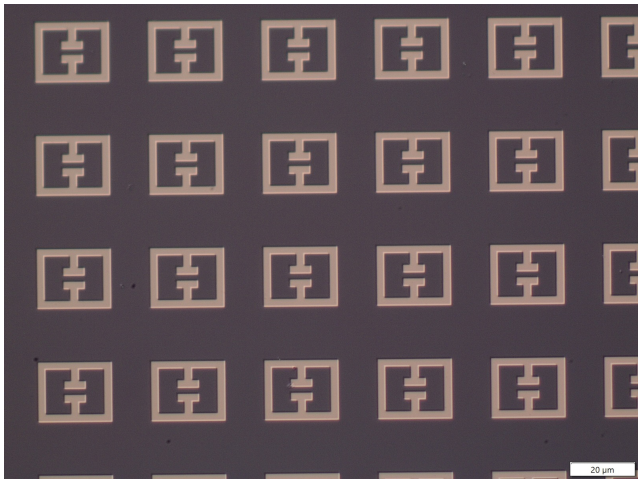

(c) Microscope image

Figure 7.1: Sample of 5x5 mm.

7.1 Terahertz response of the metasurface

The sample is measured with the experimental setup explained in Chapter 4, with the sample mounted in the Montana as shown in Figure 7.1b. The time-domain transmitted THz pulse is shown in Figure 7.2 and 7.2b (top). By taking the Fourier Transform, we obtain the transmitted spectral power shown in Figure 7.2b (bottom).

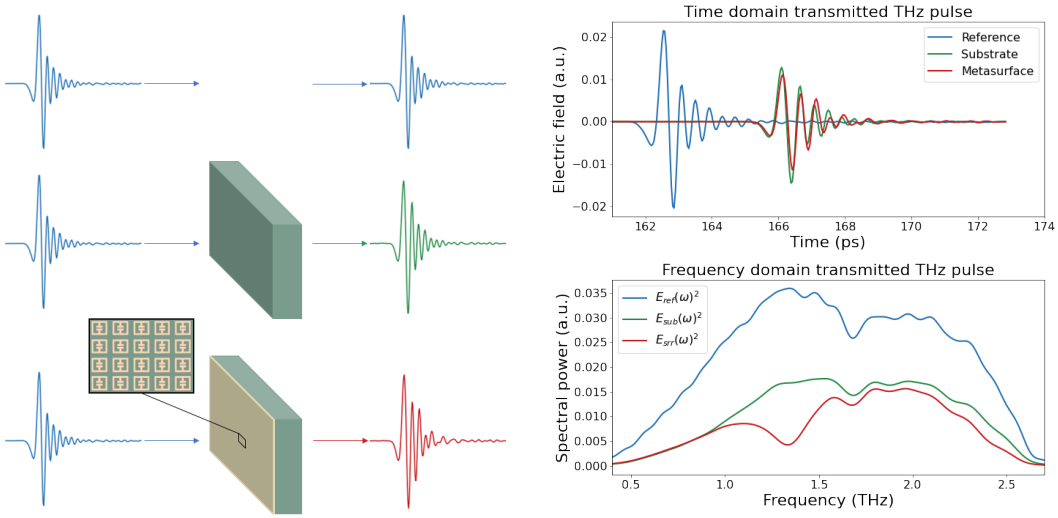

(a) Pulse propagation

(b) Measurement in time- and frequency domain

Figure 7.2: THz response of metasurface. (a). top to bottom: reference without sample, substrate, metasurface. (b). top: THz response in time-domain, bottom: THz response in frequency domain.

The resonant response is obtained by dividing the metasurface frequency spectrum by the substrate reference spectrum. If we fit an interval of the data around the LC resonance with a lorentzian as defined in Equation 3.1, we can extract both resonance frequency and Q factor with a standard deviation determined from the offset with respect to the actual data. As can be seen in Figure 7.3, the experimental data matches the simulated spectrum fairly well. The extracted resonance frequency and quality factor are slightly higher for the simulated result with respect to the experimental result. This can be clarified by a lower conductivity of gold at high frequency, since the simulations are based on the DC conductivity of gold. The actual (lower) conductivity would result in a lower resonance frequency and quality factor due to higher resistance $R \propto 1/\sigma$.

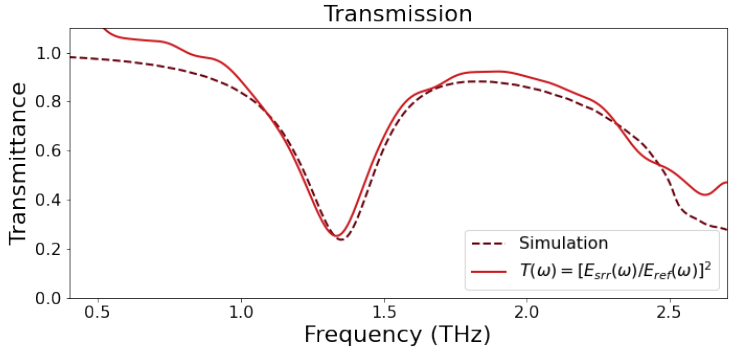

Figure 7.3: Analysis in the frequency domain of simulated (dashed red) and experimental (light red) response of eSRR sample with substrate reference. The dip in transmission corresponds to the resonant behaviour of the metasurface. Since the metasurface is extremely thin with respect to the substrate, the transmission does not deviate far from 1 except at the LC resonance at 1.36 THz, and the Rayleigh resonance at 2.51 THz.

7.2 Polarization of incident electric field

The LC resonance only couples to an incoming electric field perpendicular to the capacitor gap, as can be shown from the polarization dependence of the transmitted fields with respect to the incident (electric) field (see Figure 7.4 for the simulated polarization dependence). The dipole resonance depends on the length of the arms of the resonator in the direction of the electric field. Since this is a rectangular design, the dipole resonance is higher for incoming vertical polarization (with shorter arms) and lower for horizontal polarization (longer resonator arms). The Rayleigh resonance is most apparent for vertical incident electric field, but its resonance frequency does not depend on polarization for a square periodicity, since its wavelength is determined by the periodicity in the direction of the incident electric field.

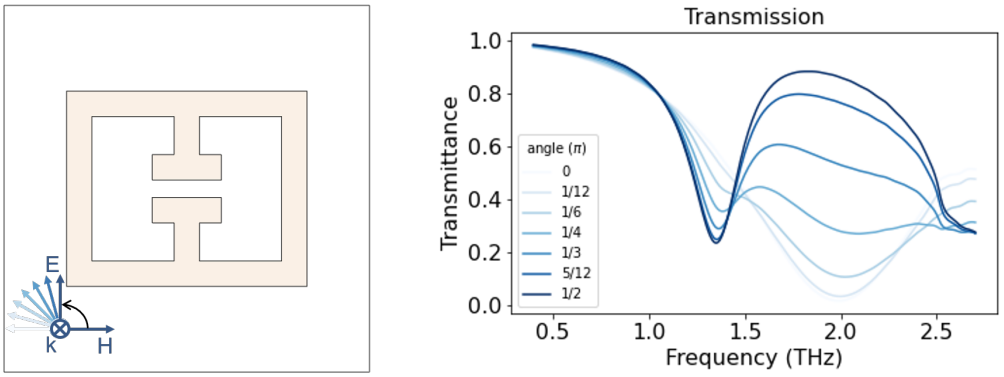

Figure 7.4: Polarization dependence of resonance on incoming electric field. The LC resonance only couples to the vertical component of the electric field. Angles are indicated with black arrow in left inset. Top arrow (different shades of blue) indicates electric field orientation of incident terahertz beam. In the vertical orientation, the LC resonance and surface plasmon resonance appear at 1.36 THz and 2.51 THz, respectively. For a horizontal incident electric field the dipole resonance appears at 1.96 THz.

To verify the agreement of experiment and simulation for all resonances, we measured the resonant response at vertical and horizontal incident electric field. Measurement of the resonant response at vertical and horizontal incident electric field is shown together with the simulations in Figure 7.5. Both are fitted with the lorentzian model described in Equation 3.1. As expected, we see the LC resonance at vertical incident field at 1.36 THz, and the dipole resonance at horizontal incident electric field at 1.96 THz. In both polarizations, we see the Rayleigh resonance at 2.51 THz. Simulation and experiment show an offset in resonance frequency for the LC and dipole resonances, but not for the Rayleigh resonance. This indicates that the offset is due to the difference in conductivity of gold between simulation and experiment. Since the Rayleigh resonance is mainly a substrate effect, this resonance is less affected by material properties of the resonators, but rather determined by permittivity of the substrate.

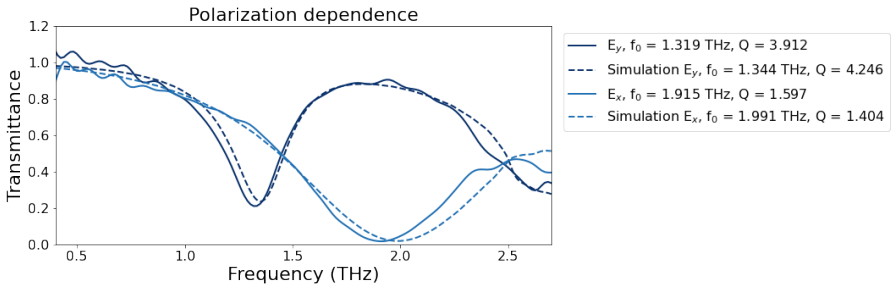

Figure 7.5: Polarization dependence

7.3 Experimental transmission and reflection

The first sample was measured both in transmission and reflection. The temperature dependence shows the sensitivity to permittivity of the substrate and conductivity of the resonators. The conductivity of gold increases for lower temperature, resulting in a smaller resistance ($R \propto 1/\sigma$). The permittivity of our sapphire substrate decreases with lower temperature, resulting in a smaller capacitance ($C \propto \epsilon$). Both result in an increase in resonance frequency for lower temperature as can be resolved from both transmission and reflection.

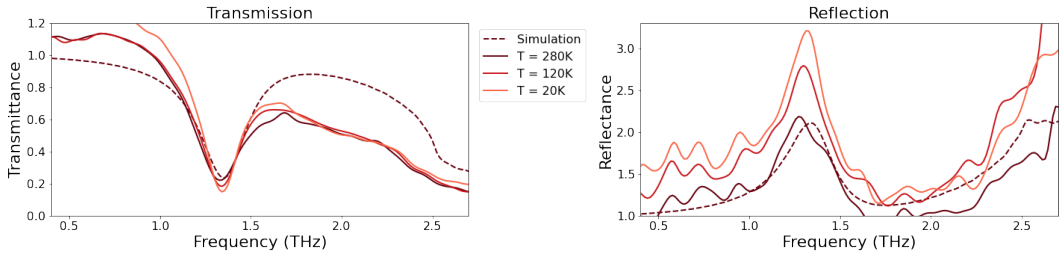

Figure 7.6: Measurement in reflection and transmission. Simulation is at room temperature. Note that the transmission spectrum for frequencies above resonance deviates from simulations and seems to indicate that the polarization of the incident field is not vertical. These measurements were taken without the polarizer present in the setup, which could indeed correspond to a not correctly polarized incident beam.

The reflection measurements are subject to more noise due to the low intensity of the measured beam after passing the Si beam splitter twice. Also, reflection measurements are more likely to suffer from alignment issues between sample and reference measurements, since offsets in alignment influence the beam path of the reflected beam. Due the low spectral power in reflection, this measurement is subject to more noise. Another disadvantage of reflection is the loss of phase information. Since it is impossible to perfectly align the substrate sample at exactly the same position as the metasurface sample for a reference, the phase information is lost. Note however, that use of the metamaterial allows us to obtain both phase and magnitude information on materials from just the real spectrum. The complex information is contained in resonance frequency and Q factor, that we extract from the magnitude of the transmittance $|t(\omega)|^2$ without considering the phase information.

7.4 Conclusion and discussion

Measurement and simulation match up fairly well. One notable feature is the fact that for all measurements there is a slight offset in resonance frequency, lower with respect to the simulation. This could be due to a lower conductivity of the gold, resulting in also a slightly lower Q factor and amplitude. As explained in Section 5.2, all simulations are based on the DC conductivity of gold, which is higher than the conductivity at THz frequencies (see Figure 2.2).

Most measurements also have a slight amplitude offset. Measurement limitations such as noise or a difference in humidity between eSRR and substrate measurements can be a cause. If this is the case, the low frequency transmission below the resonance is higher or lower than 1 (higher if the eSRR measurement is at lower humidity, lower if the substrate measurement is at lower humidity). A more fundamental reason might be a difference in thickness of the resonators between simulation and measurement, since the offset is different per sample. Since the amplitude of the resonance is subject to measurement noise, I prefer to characterize the resonance based on resonance frequency and Q factor. These inherent properties are less prone to vary between measurements, and not subject to humidity artifacts as long as the LC resonance does not overlap with a strong water absorption line.

Part III

Optimizing metasurface

Chapter 8

Design considerations of eSRR

Split ring resonators couple to only a narrow band of THz frequency light, at a frequency and bandwidth determined by the resonator material, geometry and periodic distribution over the metasurface. Design considerations of the resonant patterned surfaces depend on the material studied, parameters that need to be obtained and available detection bandwidth and power. By comparing the effect of different geometric parameters on these properties, we can deduce the impact and optimize our geometry by studying various design choices in depth through finite element calculations in COMSOL. With these simulations we want to achieve the following goals:

- Understanding the effect of geometric parameters on the resonant parameters.
- Using the knowledge to enhance quality factor to narrow the resonance bandwidth and allow more sensitive material characterization/higher resolution in resonance read-out.
- Use the knowledge to predict and optimize resonant responses, allowing to tune the design for specific material- and resonance characteristics.
- Enhance the light-matter interaction at resonance for future out of equilibrium studies.

The starting resonator geometry I chose is a simple design encountered in several papers discussing different geometries [12, 13], active metamaterial experiments [46, 47, 48], or thin film sensing [49, 50] shown in Figure 8.1 with parameters described in Table 8.1. This provides a starting point and a foolproof reference to what to expect.

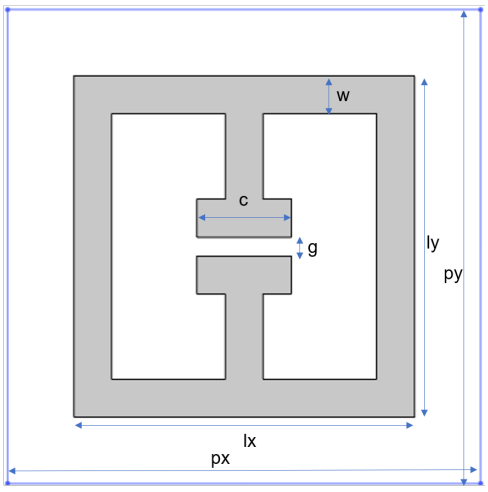

Figure 8.1: Starting geometry.

Parameter	Symbol	Length (um)
Resonator length	lx, ly	36
Capacitor length	c	10
Gap width	g	2
Linewidth	w	4
Periodicity	px, py	50
Thickness		0.2

Table 8.1: Starting dimensions of the resonator. Based on design proposed in [12, 13]

The resonance we are interested in is the LC resonance, with parameters extracted by fitting the resulting spectrum around this resonance with a lorentzian given as:

$$T(f) = -\frac{A_{\text{fit}}}{2\pi} \frac{\Gamma}{((f - f_0)^2 + (\Gamma/2)^2)} + y_0 \tag{8.1}$$

where A_{fit} gives the fitting amplitude, Γ the full width at half maximum (FWHM), f stands for frequency, f_0 the resonance frequency, and y_0 an offset for fitting purposes only. The Q factor is then defined as:

$$Q = \frac{f_0}{\Gamma} \tag{8.2}$$

We retrieve the amplitude by compensating for the offset $A = A_{\text{fit}} - y_0$.

When optimizing our resonant response, we do not only care about the material properties, but also geometric contributions. The geometry determines the strength of the light-matter interaction. A stronger resonant response comes with large amplitude and high quality factor. As will become apparent later on in the following chapters, some geometric parameters have a contradictory effect when optimizing: a higher quality factor sometimes comes with a lower amplitude. Therefore, in the optimization process we define a new parameter that maximizes them jointly as our figure of merit:

$$\text{FoM} = A \cdot Q = \frac{(y_0 - A_{\text{fit}}) f_0}{\Gamma} \tag{8.3}$$

This parameter visualizes the interplay between the sensitivity to the resonators (the amount of light coupling to the metamaterial affects the amplitude) and the strength of the interaction at resonance (corresponding to a high Q factor). Both affect the light-matter interaction which we want to maximize at resonance. The error bars in all plots indicate the error of the fit with respect to the data, and lines through the data points are fits to a polynomial, serving solely as a guide to the eye.

8.1 Metasurface material and thickness

We obtain a resonant response when a periodic array of conducting structures is placed on a dielectric substrate. Both the resonator- and substrate material impact the resonance through their respective conductivity ($R \propto 1/\sigma_1$) and permittivity ($C \propto \epsilon$). The resonator itself is made of a conductor, usually a metal (in this case gold). Metallic resonators have a purely dissipative contribution to the resonance equivalent circuit. The properties of the resonator that affect the resonance quality are the conductivity, skin depth and resonator thickness.

A perfect electric conductor (assumed to have infinitesimal thickness, infinite conductivity and therefore zero skin depth) provides an upper limit of both resonance frequency and quality factor in terms of conductivity, ignoring the resistive contribution of finite conductance to the LC circuit (see black dashed line in Figure 8.2). This shows the ideal interaction for the geometry, without depending on the metal used, and therefore also shows how the finite conductivity of a non-ideal material affects the resonances. This shows that the resistive contribution from dissipation is small with respect to inductance and capacitance. For gold, the finite conductivity results in a 1.1% shift of the resonance frequency with respect to the PEC resonance. The Rayleigh resonance at 1.81 THz is barely affected by conductivity or resonator thickness, as expected since this resonance is mainly a substrate effect.

8.1.1 Choosing a thickness

The metal film needs to be at least thicker than the skin depth to have a saturated response to the incident radiation [51], and twice the skin depth for a minimum in Ohmic losses [52].

Ohmic losses of the metamaterial are modelled with an effective resistance of the eSRR. This effective resistance is obtained by using the equivalent ring model for the current distribution in the resonator arms. If a constant azimuthal surface current density is assumed on the ring, the resistance can be approximated as:

$$R = \begin{cases} \frac{2\pi r_0}{w d_{\text{res}} \sigma_1}, & \text{if } \frac{d_{\text{res}}}{2} < d_{\text{skin}} \\ \frac{2\pi r_0}{w d_{\text{skin}} \sigma_1}, & \text{otherwise} \end{cases} \tag{8.4}$$

where $2\pi r_0$ is the perimeter of the resonator loop, w the linewidth of the resonator, σ_1 the real part of the conductivity, d_{res} the resonator thickness and d_{skin} the skin depth [52].

The skin depth of a metal, defined as the distance perpendicular to the interface in which the electric field in the conductor drops by a factor of e, is given as:

$$d_{\text{skin}} = \frac{1}{\sqrt{\pi f \sigma \mu_0 \mu_r}} \tag{8.5}$$

with f the frequency, σ the metal conductivity, μ_0 the vacuum permeability and μ_r the relative permeability [51]. This gives a skin depth of gold of 78 nm at 1 THz.

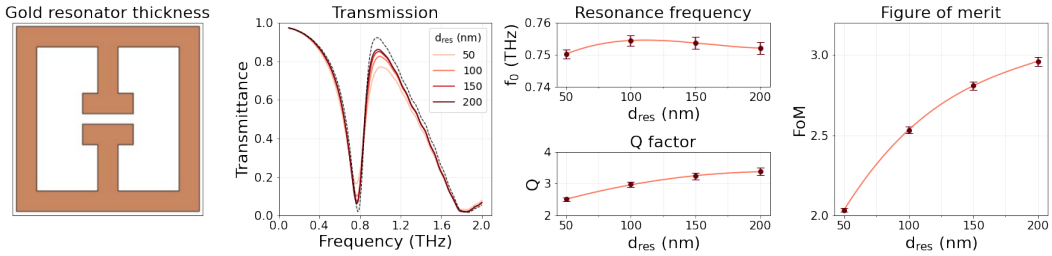

Figure 8.2: Resonator material, black dotted line is for a perfect electric conductor (PEC). The PEC resonance: $f_0 = 0.760$ THz, $Q = 4.07$, the gold (200 nm) resonance: $f_0 = 0.752$ THz, $Q = 3.38$.

The conductivity of the resonator material affects both the resonance frequency and quality factor, the thickness of the resonator limits the resonance quality. For optimal resonant properties, metals with high conductivity and resonators with a thickness of twice the skin depth are preferred. This results in a strong resonant response and then the conductivity can be determined from the resistance directly.

8.2 Frequency regimes

The metamaterial studied in this thesis is aimed at a resonant response in the terahertz regime. The design described in this chapter is one that is reproduced multiple times [12, 13, 46, 47, 48, 49, 50], but alternative geometries serve the same purpose [38, 33, 53, 54, 55, 56, 57]. Also, electric split ring resonators with the same shape have been used in the GHz regime with geometric parameters in the mm-range instead of um-range [19, 58, 59, 60, 61, 62, 35]. The ratios between parameters are slightly altered, but other than that similar response is obtained. Based on these observations, I wanted to know to what extend the same resonant response can be obtained at a different frequency. By multiplying all planar geometric parameters by a unit-less constant scaling parameter s, we see how the metamaterial's response changes over frequency regimes, shown in Figure 8.3a.

Remarkably, the quality factor and amplitude remain practically the same while the resonance frequency shifts over nearly our entire broadband spectrum. This enables us to choose a suitable resonance frequency for any experiment without changing the quality of a certain optimized geometry. Of course, again this is limited by fabrication method to a certain extent when shrinking the geometry to obtain a higher resonance frequency. In the equivalent circuit model, this result implies that the quality factor only depends on ratios in distance, whereas the resonance frequency scales with length. The capacitance and inductance both are linear dependent in length. The resistance only depends on the ratio (for constant resonator thickness). The resonance frequency follows this simple function:

$$f_0(s) = f_0(s = 1)/s \tag{8.6}$$

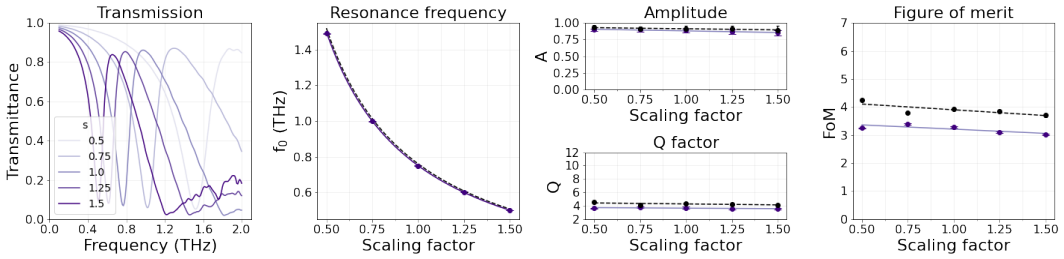

(a)

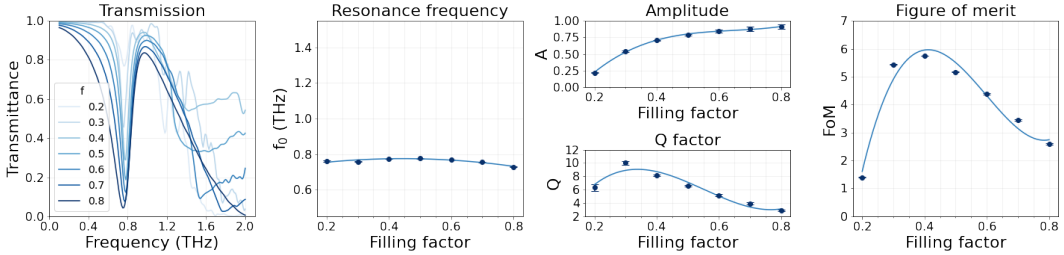

(b)

Figure 8.3: Scaling (a) and filling (b) factor. Scaling allows us to change the resonance frequency without affecting the figure of merit, whereas the filling factor influences figure of merit without changing the resonance frequency. Dotted line in scaling plots shows the scaling for PEC instead of gold resonators, showing that the resistive contribution gives a constant (relative) offset in resonance frequency and Q factor.

A perfect electric conductor also shows this scaling behaviour, with a constant offset in resonance frequency with respect to the gold resonators due to the additional resistive contribution from finite conductivity. The offset in resonance frequency is marginal with respect to the offset in quality factor. This shows that the quality of the resonance is more sensitive to dissipation than the resonance frequency, in line with expectations based on the equivalent circuit model where the resonance frequency only depends on resistance in its second order term, and the quality factor mainly depends on resistance $Q \propto 1/R$.

8.3 Packing regimes

The LC resonance is governed from the interaction within an individual resonator. Therefore, the resonance is determined by the geometry within one unit cell, and coupling between resonators only gives small perturbations to this resonance, but should not change the physics. To verify this, I have studied another unit-less parameter, defined as the filling factor $f = l/p$ (see Figure 8.3b). Here the filling factor is determined as the ratio between resonator arm length l and periodicity of the array p. From the simulations we can see that the filling factor indeed barely affects the resonance frequency, but the quality factor is highly sensitive. This is the case because of the radiative losses that are minimized for a critical periodicity.

This parameter also shows the importance of the figure of merit as defined in Equation 8.3. An optimum in quality factor occurs for low filling factor, whereas the amplitude of the resonance is optimum for high filling factor. The periodicity in resonators sets the sensitivity to the resonators (the amount of light coupling to the metamaterial affects the amplitude) and interference of radiation turns out to have a noteworthy effect on quality (the strength of light-matter interaction at resonance).

The resonators are arranged on the substrate in an array with a certain periodicity. This periodicity influences the coupling between resonators, both in terms of radiation and Ohmic losses. If the resonators are close together, the outer dimensions can couple to neighbouring resonators, contributing in terms of capacitance (in the y direction) or mutual inductance (in

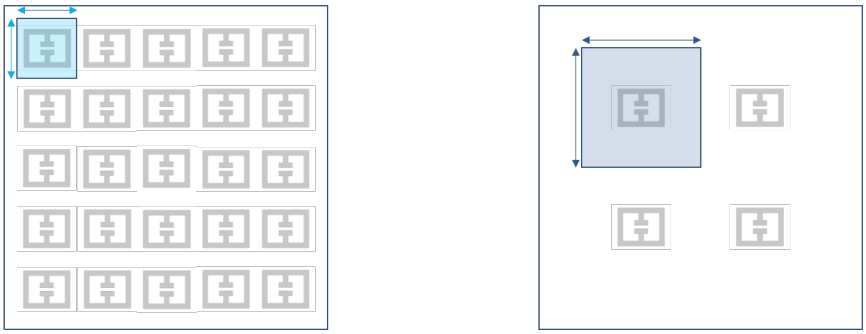

Figure 8.4: Packing regimes. Left: Ohmic regime. Coupling between resonators results in crosstalk, decreasing both quality factor and resonance frequency. Right: Radiative regime. An optimum in quality factor is obtained for critical periodicity at the Rayleigh or Wood anomaly [41].

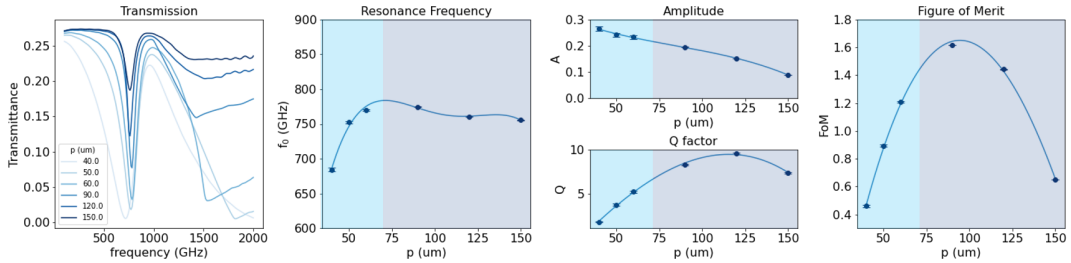

Figure 8.5: Packing density. The light blue corresponds to Ohmic regime, dark blue to Radiative regime. The critical periodicity is at 116 um.

the x direction), both resulting in a lower Q factor [21, 59, 63]. A larger spacing between the resonators results in a smaller amplitude due to the fact that not all radiation will interact with the metamaterial, but rather only interact with the substrate. There are two 'regimes', shown in Figure 8.4: for small periodicity (small spacing between resonators), the array of resonators will couple strongly to each other, contributing to Ohmic effects, and the Rayleigh resonance follows the periodicity of the array. For larger periodicity (in the order of the THz wavelength), radiative coupling is enhanced [64, 63] and higher order modes such as the dipole and Rayleigh resonance become weaker [42]. At the critical periodicity, corresponding to the Rayleigh or Wood anomaly [41, 42], constructive interference also occurs for field components scattered into the sample plane. This field contribution is coupled to other elements rather than to free space so that its energy gets 'trapped' in the array [64].

8.4 Conclusion and discussion

In this chapter, the design goals are stated. From Section 8.1 we can conclude that a highly conductive material with resonator thickness of at least twice the skin depth is preferred for a saturated response with minimum dissipation. For gold resonators, this comes down to a thickness $d_{\text{res}} = 156$ nm for a resonance at 1 THz. In the optimization process, we can focus on the Figure of merit defined in Equation 8.3, that combines the high quality factor (corresponding to a narrow resonant response with minimum losses) with high amplitude (corresponding to the amount of light coupling to the metasurface). We can leave out the resonance frequency of the optimization, since we can afterwards scale the design to a preferred resonance frequency without affecting the Figure of merit, as described in Section 8.2. The quality factor of the LC resonance can be enhanced by placing the eSRRs in an array with critical periodicity at the Rayleigh or Wood anomaly. From the packing density of the resonators, we can also confirm that higher order modes become weaker for larger periodicity,

which is not the case for the LC resonance.

Chapter 9

Optimizing the resonant metasurface

In order to develop a metasurface that is optimally tailored for the purpose of thin film sensing, I calculate the spectrum of a large set of geometries. By changing the planar geometric parameters one by one it is possible to deduce the effect of each parameter on our resonant parameters. This also provides a stringent test for the equivalent circuit model introduced in Section 3.2. In Chapter 8 we have established that we can focus the optimization process on our figure of merit, combining the amplitude (corresponding to how much of our incident beam interacts with the eSRRs) and quality factor (showing the strength of the light-matter interaction at resonance) of the metasurface resonance. The space of possible metasurfaces is infinite, and cannot be explored. Instead, I focus on the basic design discussed in Chapter 8, and consider perturbations of this within the constraints of fabrication feasibility. Geometric features smaller than a micron are more technically challenging in the e-beam lift off procedure (see A.1 in Appendix A for the procedure), so this is set as the minimal feature size. We leave out the resonance frequency of our optimization procedure, since we can tune this afterwards by multiplying all parameters with scaling parameter s, explained in Section 8.2. All simulations in this chapter consist of gold resonators ($\sigma = 4.09{\cdot}10^7$ S/m [33]) on a sapphire substrate ($n = 3.31$, $\alpha = 0.18$ cm^{-1} [34]). These parameters are constant over frequency, such that changes in resonance can be assumed to be purely due to geometric modifications. The simulations in this chapter are based on the geometry described in Table 8.1 and shown in Figure 8.1, where within each subsection only the indicated geometric parameter is changed with respect to these dimensions.

9.1 Geometry

The resonant properties of the metamaterial depend on the resonator geometry. Different parameters have different impact on resistance, capacitance and inductance. For example, the loop, which is responsible for both inductance and resistance, is affected by linewidth and resonator length, whereas the capacitance mainly depends on the capacitor length and gap width, but also on linewidth. Figure 9.1 shows the geometric properties, which are further elaborated on in the following subsections.

9.1.1 Resonator length

The resonator length l determines the loop circumference and therefore the inductance. A smaller loop corresponds to smaller inductance (and resistance) and according to the equivalent circuit model this comes with a higher resonance frequency. Since the resistive contribution is small with respect to the inductance, the quality factor also increases for smaller l. The resonator length also influences the dipole resonance, which shifts upward for decreasing resonator length (see Section 9.2 for a further explanation).

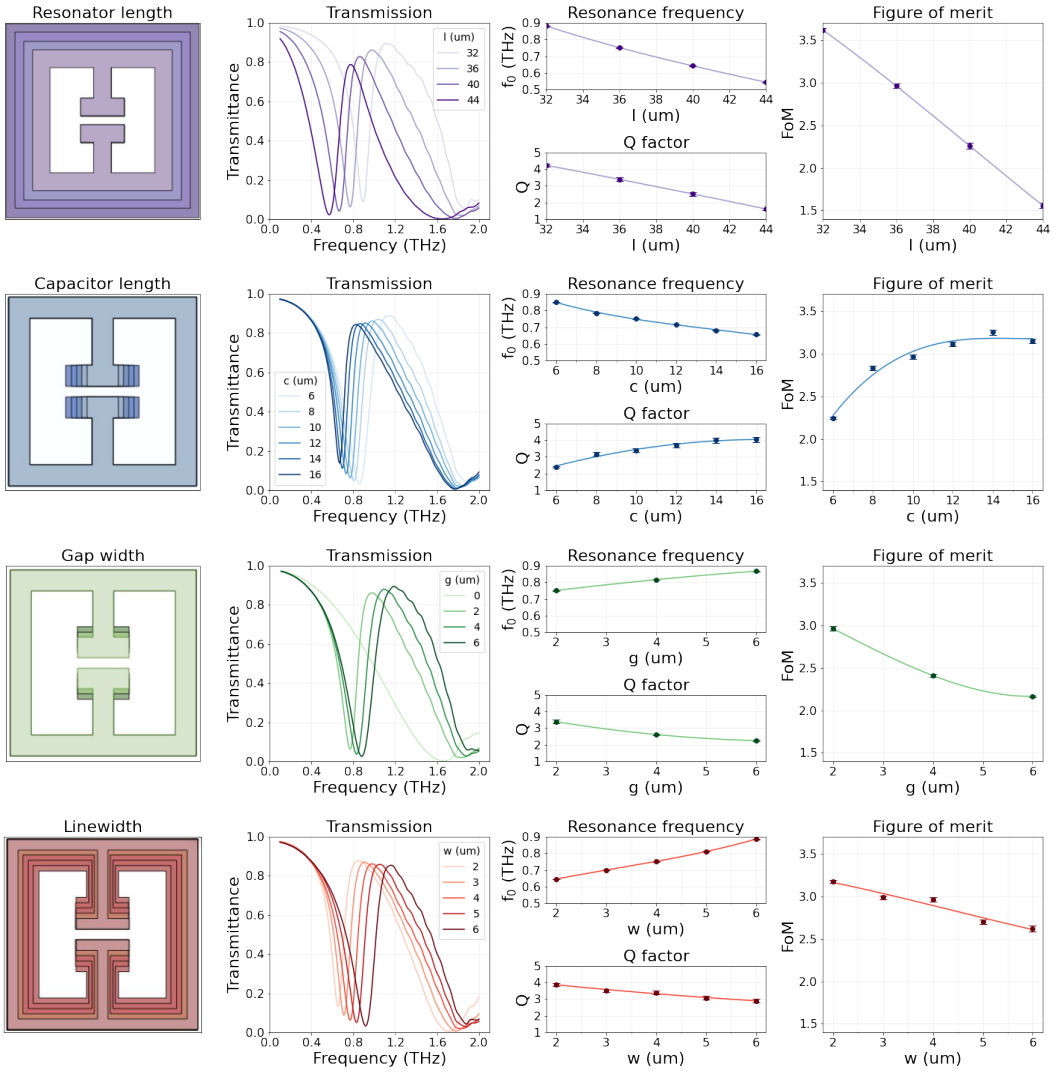

Figure 9.1: Geometric properties of resonant design.

9.1.2 Capacitor length

Increasing the capacitor length not only leads to an increase in capacitance, but also contributes to the inductance. Worth noticing is that the minimum in transmission at the resonance frequency goes up for a longer capacitor, due to decreased coupling strength [19]. The quality factor also increases due to the increase in inductance which apparently has a larger impact than the increase in capacitance, accompanied by a decreasing resonance frequency. The increasing quality factor saturates when the capacitor is long enough to couple to the outer resonator arms. In the final design I will therefore elongate the capacitor, but to such an extent that cross-talk with the outer arms is limited.

9.1.3 Gap width

Increasing the gap width will decrease capacitance and therefore result in a higher resonance frequency and lower Q factor. A small (but finite) gap is preferred, but the actual size of the gap is fabrication limited to a minimum value of approximately 1 um.

Without the capacitive gap, no LC resonance will occur. Therefore for zero gap width, we only see the dipole resonance and the LC has vanished. By closing the resonator, all even modes vanish and odd modes appear[42, 44]. With the gap closed the dipole resonance now

appears at 1.636 THz according to:

$$\lambda_0 = \frac{3}{2} \cdot n_{\text{sub}} \cdot l_y \tag{9.1}$$

9.1.4 Linewidth

The linewidth of our resonator will affect all circuit components (inductance, capacitance and resistance) to a certain extent. Decreasing the linewidth will increase our loop perimeter (due to the way it is defined here), and decrease both resistance and capacitance. Resonance frequency and amplitude drop for a smaller linewidth, while the quality factor increases. Also the dipole frequency drops, but remains fairly equidistant with respect to the LC resonance. In the optimization process, I leave the linewidth as an open parameter that I can later on use to tune the resonance frequency.

9.2 Rectangularity

From the last paragraph on geometry we have learned that a smaller resonator length leads to a higher quality in resonance, but so far we have only considered changing the parameter both in x- and y-direction. By changing only one of the axes it is possible to move the higher order modes up or down with respect to the LC resonance [38].

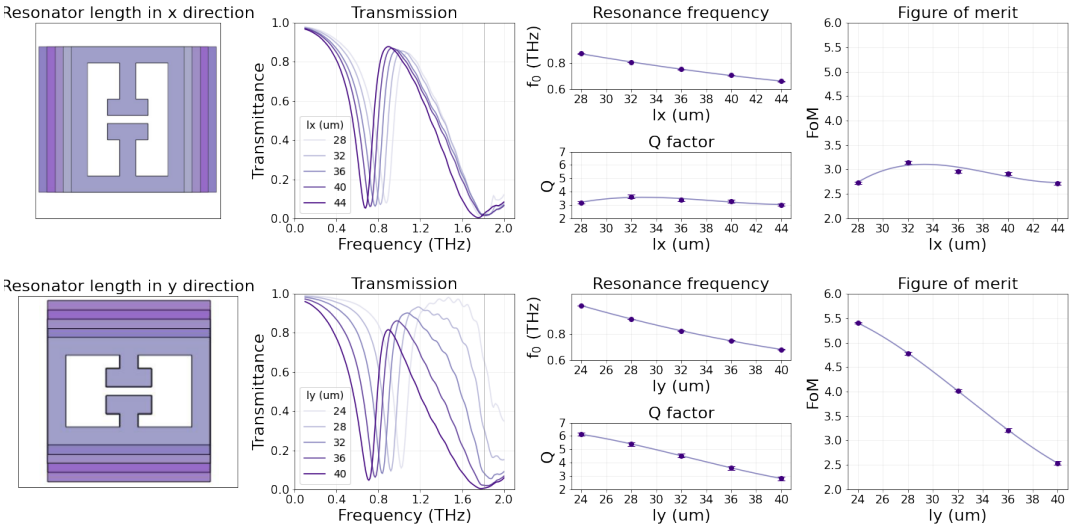

Figure 9.2: Rectangularity of resonant design. Grey line indicates Rayleigh resonance at 1.81 THz.

9.2.1 Resonator length in x direction

Changing the resonator length in the x direction barely affects the dipole and Rayleigh resonance. Only when the distance between adjacent resonators becomes smaller than the distance between the three vertical strips inside one resonator, we observe a downward shift in dipole frequency. This provides us with an upper limit in horizontal resonator length.

9.2.2 Resonator length in y direction

The vertical resonator length has a more pronounced effect on both LC- and higher order mode resonances. The LC resonance decreases for increasing l_y. The dipole frequency shifts up for smaller vertical resonator length, and the overlap between the resonances decreases. Since a smaller length corresponds to smaller inductance, the increase in quality factor for

small l_y at first seems contradictory, but can be clarified by the decrease in overlap between resonances. Both LC and dipole resonance show a lowering in quality factor due to the overlap between the effects. These phenomena are both a result of the lorentzian lineshape which we use to fit. Moving the dipole resonance out of our fitting regime will prevent this distortion. The strength of these higher-order resonances becomes weaker with a decreasing geometrical size of the structure [42]. We can also see that the Rayleigh resonance (1.81 THz) barely depends on resonator arm length, as expected.

9.3 Periodicity

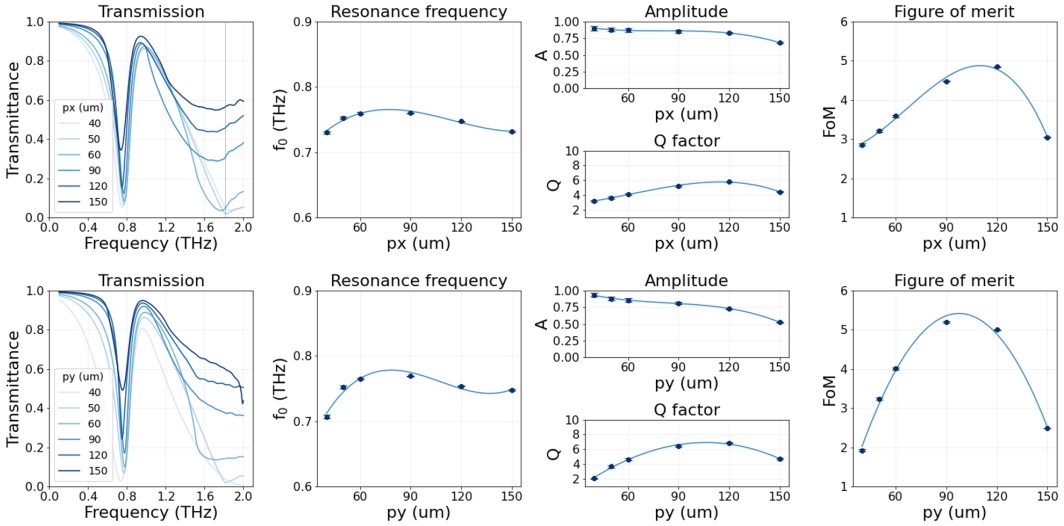

Figure 9.3: Periodicity of array

9.3.1 Periodicity in x direction

In the so called 'Ohmic regime', decreasing the horizontal distance between the resonators results in crosstalk between the inductive loops of neighbouring resonators. Both resonance frequency and quality factor decrease due to these inductive effects. When we move to a larger periodicity, the resonance frequency stabilizes, since neighbouring resonators no longer contribute in Ohmic effects (or at least the effect is small compared to the individual resonance effects), but the quality factor still increases up to a maximum at $p = 120\mu m$ for this design, where the periodicity matches the SRR resonance wavelength normalized with the refractive index of the substrate:

$$p_{\text{optimum}} = \frac{\lambda_0}{n_{\text{sub}}} \tag{9.2}$$

This minimum of radiative losses, resulting in an increase of Q roughly by a factor 2, gives great perspective on sensitivity to changes in conductivity of the resonator. As explained in Section 8.1, the conductivity and thickness of the resonator mainly affect the quality of resonance rather than the resonance frequency, which means that we maintain our optimum in sensitivity when comparing resonator properties over for example temperature (changing the conductivity of the resonator) or for different resonator thickness.

9.3.2 Periodicity in y direction

When the vertical distance between the resonators is small, the additional capacitive coupling results in a decrease of both resonance frequency and quality. The y periodicity has a stronger

influence on amplitude than the periodicity in x direction. This shows that the vertical packing density has a stronger impact on how much the radiation interacts with the metamaterial than the horizontal packing density. Again we see a minimum in radiative losses at the critical periodicity given by Equation 9.2. The Figure of merit shows that due to this strong decrease in amplitude, the optimal periodicity considering both quality factor and amplitude is different from the optimal periodicity based on maximum Q factor.

9.4 Conclusion and discussion

In this chapter, the effect of geometric parameters on the resonant response are determined. Based on the design goals stated in Chapter 8, we can conclude that we want to:

- maximize the capacitor length without coupling to the vertical resonator arms
- minimize vertical resonator arm length to prevent distortion from overlap with the dipole resonance, but without inducing coupling between horizontal resonator arms and capacitor arms
- maximize the loop perimeter by increasing the horizontal resonator arm length, but without inducing mutual inductance coupling to neighbouring resonators
- minimize capacitor gap width, taking into consideration a minimum gap width of 1 um due to fabrication limitations
- set the periodicity of the array at the critical periodicity corresponding to the Rayleigh anomaly

To determine the optimal design, I have summarized these conclusions in formulas shown in Table 9.1 with parameters shown in Figure 9.4. The design is determined based on two open parameters: the capacitor length c and linewidth w. In the final design, these parameters are set such that we obtain a resonant response at approximately 1 THz for a sapphire substrate.

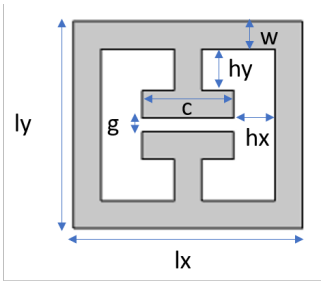

Figure 9.4: Resonator geometry.

Parameter	Symbol	Length (um)
Gap width	g	0.5·w
Coupling distance	hx,hy	1.5·w
Resonator length	lx	c+2·w + 2·hx
	ly	g + 2·w + 2·hy
Periodicity	px, py	λ_0/n_{sub}
Thickness		0.15

Table 9.1: Dimensions expressed in terms of capacitor length c and linewidth w.

The e-beam liftoff fabrication procedure (shown in Figure A.1) limits the minimum geometric size to 1 um. The smallest geometric parameter is the capacitor gap g defined as 0.5·w. Coupling distances hx and hy are set to 1.5 times the linewidth to prevent capacitive coupling between resonator arms and the capacitive plates in the center. For the final design, I have set the linewidth to 3 um (such that we can still scale the design for a higher frequency resonant response), and the capacitor length to 10 um to obtain a resonance at 1 THz. The thickness of the metasurface is 150 nm, set to twice the skin depth of gold at 1 THz.

Chapter 10

The optimized design

The main goal of this thesis is to optimize an eSRR metasurface for material characterization of both resonator and substrate, and to verify the sensitivity to optical parameters. We have determined the effect of geometric parameters on the resonant parameters, and used this knowledge to optimize the resonant response for enhanced light-matter interaction at resonance, with a narrow resonant response. This chapter is dedicated to characterizing our optimized design both from simulation and experiment. Section 10.1 is devoted to characterization of the LC resonance from the electric and magnetic near-field and current densities, followed by the experimental characterization in Section 10.2. To show the versatility of this design, we look at the resonant response on different substrates shown in Section 10.3.

The geometry of the optimized design is shown in Figure 10.1 with parameters shown in Table 10.1.

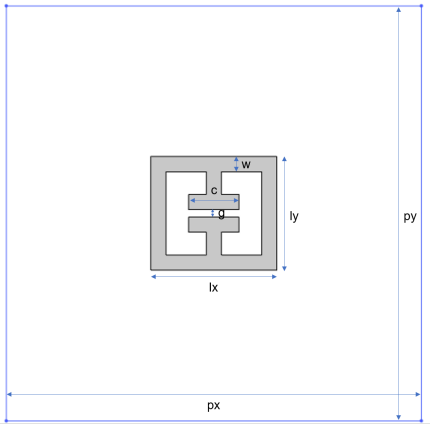

Figure 10.1: Resonator geometry.

Parameter	Symbol	Length (um)
Resonator length	lx	25
	ly	22.5
Capacitor length	c	10
Gap width	g	1.5
Linewidth	w	3
Periodicity	px, py	82.3
Thickness		0.15

Table 10.1: Dimensions of the resonator.

The simulated transmission spectrum of the optimized design is shown in Figure 10.2. If we compare to the initial design introduced in Part II, we see that the optimized resonance is much more confined to a narrow frequency interval, but at the cost of a smaller amplitude due to the low filling factor. The higher order modes only appear as a soft kink in the frequency spectrum, much weaker due to the small geometric sizes [42], and at higher frequency such that the LC resonance is not distorted by higher order plasmonic modes. The LC resonance is enhanced by the overlapping Rayleigh anomaly, as a result of the lattice mode mediated radiative coupling in the array [64]. Already from the high quality factor visible in the transmission spectrum, we expect a strong resonant response at the LC resonance. In the following section, characterization of the near-field and current densities reveals the enhancement of the electric field at resonance, and the effect of the overlapping Rayleigh anomaly.

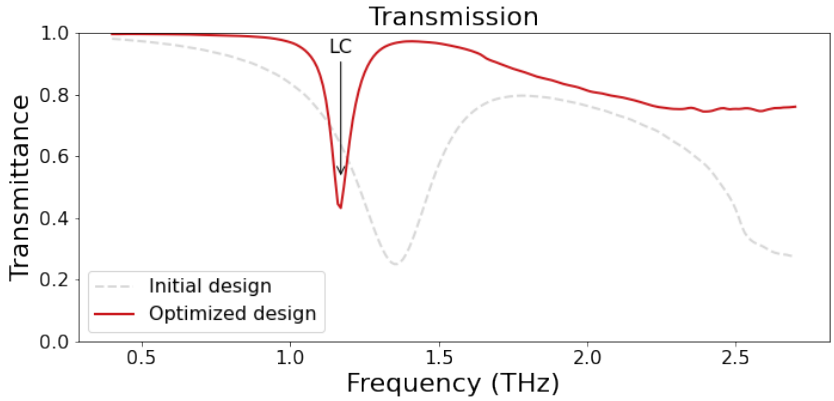

Figure 10.2: Simulated transmission spectrum of optimized design. In the optimized design, the only strong resonance is the LC resonance at 1.17 THz (indicated with black arrow). The dipole resonance at 2.01 THz merely results in a soft kink in the frequency spectrum. The dashed light grey shows the transmission spectrum of the initial design introduced in Part II.

10.1 LC resonance characterization

I want to make sure that the resonant behaviour is still the same as for the initial design, but with higher intensity. From the electric field norm shown in Figure 10.3, we see that we obtain a resonant response with fields up to 50 times stronger than the incident electric field. This is a result of the strong response leading to strongly inhomogeneous fields at the metasurface [11]. Especially in the THz regime, this opens up an avenue of nonlinear spectroscopy which is difficult to achieve with free-space methods due to the technological limitation of weak THz sources [65]. This strong resonant response is a result of the high current densities, resulting in a magnetic out of plane component (Figure 10.3) up to 4 times stronger than for the LC resonance of the initial design (Figure 6.4).

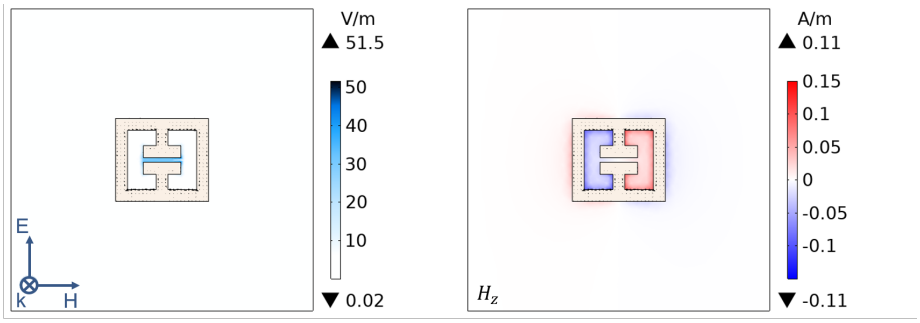

Figure 10.3: Simulation of electric field norm, surface current density and out of plane magnetic field at the LC resonance (1.17 THz). The surface current density is scaled to half the intensity with respect to figures in Chapter 6.

From the electric field components shown in Figure 10.4, we see the effect of the lattice mediated radiative coupling from the overlapping Rayleigh resonance. The field components are also 3-4 times stronger than for the LC resonance of the initial design (Figure 6.5), and of comparable intensity with respect to its Rayleigh resonance (Figure 6.7). Remarkably, whereas overlap between LC and dipole resonance would result in distortion or weakening of the net metamaterial response [36, 37], overlap with the Rayleigh anomaly enhances the resonant response [63, 64].

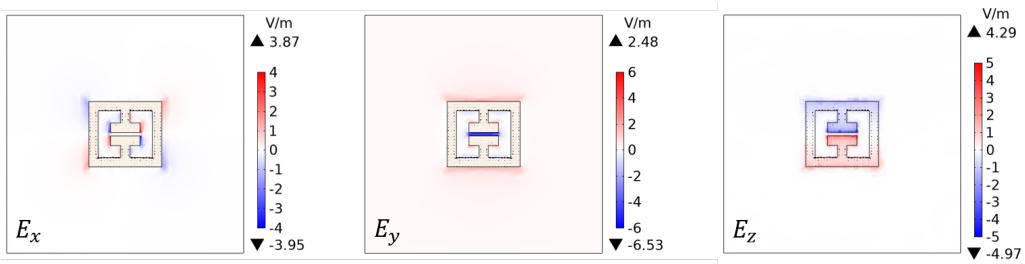

Figure 10.4: Simulation of electric field in x, y and z direction, and surface current density at the LC resonance (1.17 THz). The x and y components are evaluated at the metasurface, whereas the z component is evaluated 10 nm below the surface in the substrate (the out of plane components are zero at the transition boundary corresponding to the resonator).

10.2 Experimental characterization

After characterization of the simulated resonant response, we investigated the experimental resonant response from time-domain terahertz spectroscopy, shown in Figure 10.5. Already in the frequency domain spectral power we see a dip at 1.17 THz corresponding to the LC resonance (see bottom Figure 10.5b).

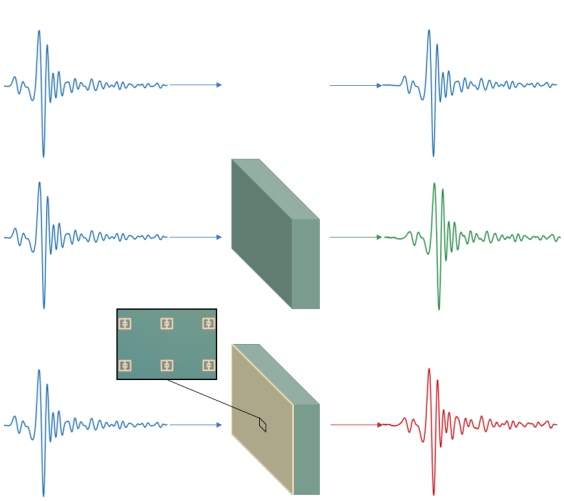

(a) Pulse propagation

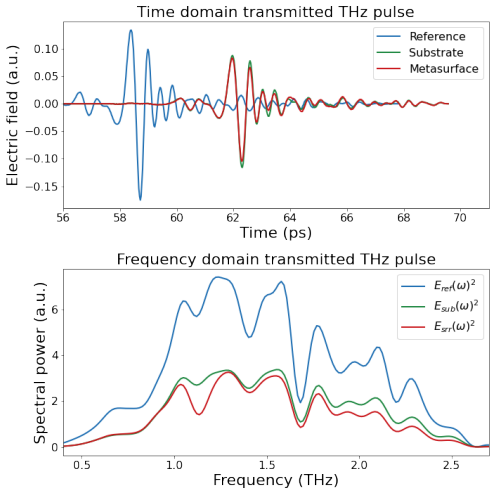

(b) Measurement in time- and frequency domain

Figure 10.5: THz response of optimized metasurface. (a). top to bottom: reference without sample, substrate, metasurface. (b). top: THz response in time-domain, bottom: THz response in frequency domain.

We obtain the tranmittance of the metasurface by dividing the pulse by a substrate reference, shown in Figure 10.6. The experimental result again matches the simulated response fairly well, except for a small offset in resonance frequency and Q factor (probably due to the difference in conductivity) and amplitude. The offset in amplitude could either be due to humidity effects, but for this particular measurement it is rather unlikely since the low frequency spectrum is close to 1 and the spectrum reveals no clear water absorption lines. Another possible explanation would be an offset in the actual thickness of the metamaterial, indicating that the metasurface is thinner than 150 nm corresponding to a lower Q factor and amplitude.

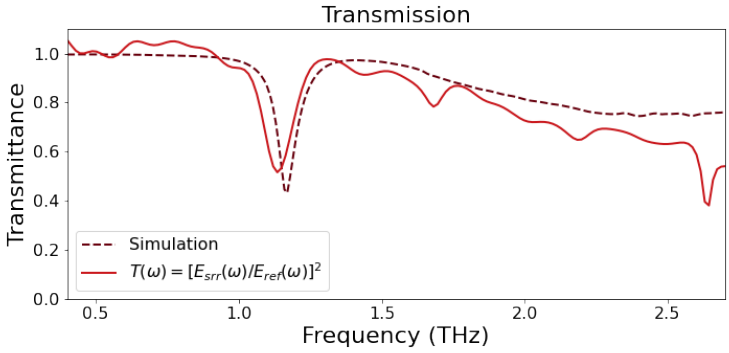

Figure 10.6: Analysis in the frequency domain of simulated (dashed dark red) and experimental (solid light red) response of optimized eSRR sample with sapphire substrate reference. The dip in transmission corresponds to the resonant behaviour of the metasurface.

10.2.1 Comparison of designs

To compare between the two designs, we did a temperature sweep on both of them to see how sensitive they are to material properties. We have two contributions in the temperature dependence: conductivity of gold and permittivity of the substrate.

First, we determine the temperature dependence of the sapphire substrate, shown in Figure 10.7. From the decrease in refractive index we expect an increase in resonance frequency and increase in quality factor for lower temperature, both scaling with $1/\sqrt{\epsilon}$.

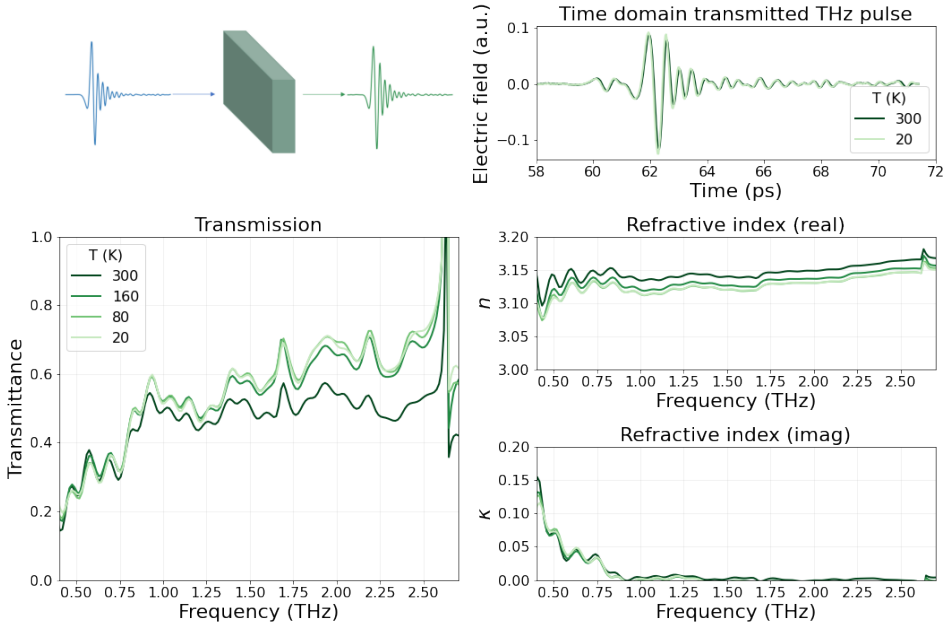

Figure 10.7: Temperature dependence of 500 um sapphire substrate. The complex refractive index is extracted from the transmission spectrum following the method explained in Section 4.3.1. The real part of the refractive index is related to the permittivity as $n = \sqrt{\epsilon}$.

The conductivity of a metal increases with decreasing temperature. From the increase in conductivity we also expect a increasing resonance frequency and increasing quality factor with decreasing temperature, both scaling linearly with conductivity $f_0, Q \propto 1/\sigma$.

We can extract this temperature dependence for both designs shown in Figure 10.8, but the trend seems different. This could be due to one of the designs being more sensitive to

conductivity and one to substrate permittivity.

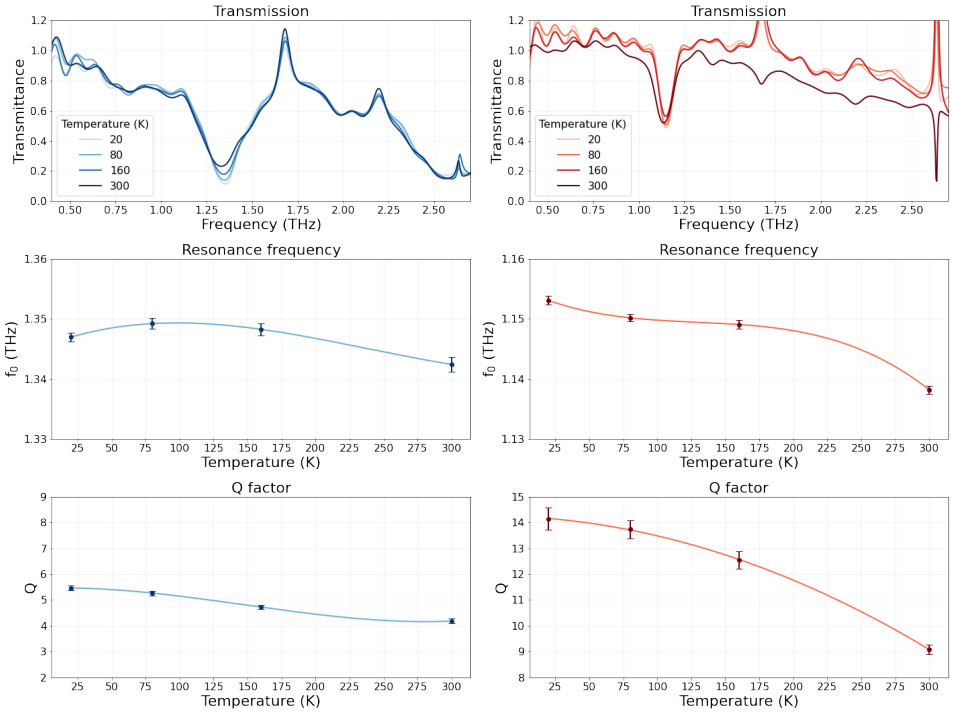

Figure 10.8: Comparison of designs. Left (in blue) is the original design introduced in the first chapters. Right (in red) is the optimized design. Both show a decrease in both resonance frequency and quality factor with increasing temperature. The peak in transmission at 1.7 THz is a result of the difference in humidity between metasurface- and substrate reference measurements. Especially the initial design measurements show a lower humidity for the metasurface measurement, resulting in the lower transmission (below 1) for frequencies below the resonance frequency.

10.3 Different substrates

To show the versatility of this design, we have deposited it on three different substrates. A dielectric substrate will affect the resonance frequency through its permittivity which sets the capacitance the LC circuit. Higher refractive index materials such as LAO therefore have a larger capacitance. Since the electric field extends up to tens of microns into the substrate, only a thin layer underneath the sample affects the resonance [45]. The substrate thickness therefore does not affect the resonance, provided that the thickness is larger than the electric field penetration depth.

We can determine the substrate dependence by comparing between substrates. The transmission for each substrate is shown in Figure 10.9. The LAO substrate has a phonon mode at 5.1 THz (see also Figure 2.3), resulting in a slope in the transmission spectrum in our measurement window. The $DyScO_3$ substrate has a very low transmission due to an electric mode opening within our measurement window. The sapphire substrate has a flat spectrum.

In Figure 10.10, the metasurface measurements for each substrate and simulations are shown. All three samples show similar resolution in resonance. With a lower Q factor, we would not have been able to resolve a resonance for the DSO substrate, because the resonance would be broader than the resolvable frequency bandwidth. This measurement shows that we can resolve resonances close to a Reststrahlen band, enabling possible cavity-phonon coupling experiments.

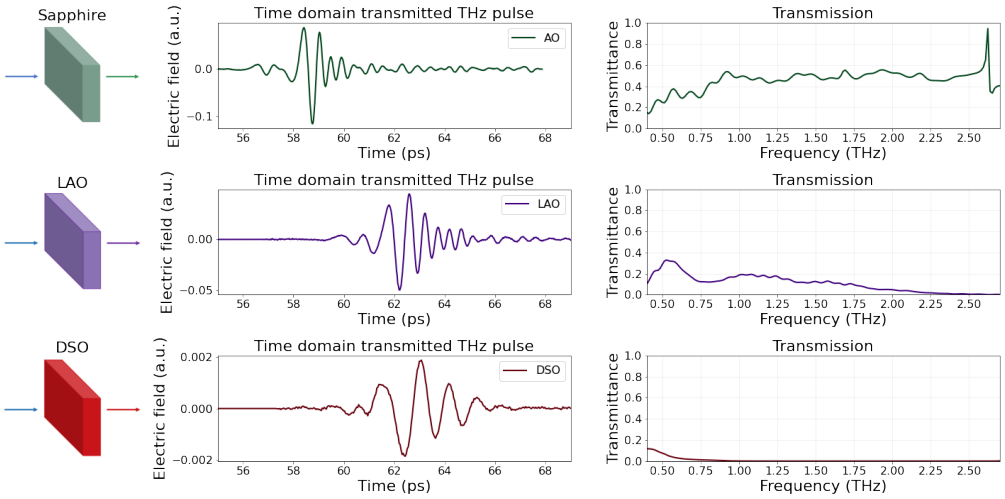

Figure 10.9: THz spectroscopy of several substrates. Sapphire (top) has the lowest refractive index and a flat spectrum. LAO (middle) and DSO (bottom) have similar refractive index, but due to collective modes of the lattice, the frequency spectrum is perturbed. DSO has an electronic mode at 1 THz, LAO has a phonon mode at 5.1 THz.

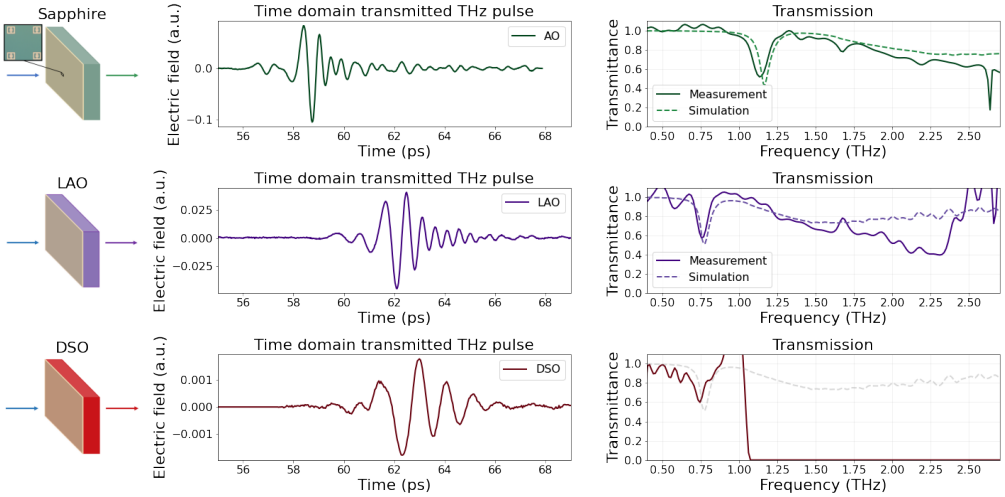

Figure 10.10: THz spectroscopy of metasurface on several substrates. The resonance is resolvable for all substrates, even for very low transmission such as for the DSO measurement. Grey dotted line in DSO transmission plot is the simulated resonance for LAO substrate (LAO simulation based on permittivity of LAO as determined in [66]). This shows that even though the transmission spectra of LAO and DSO substrates are very different, the resonance is almost at the same resonance frequency because the substrates have almost the same refractive index. The LAO resonance deviates from the simulated spectrum due to an additional mode at approximately 2.3 THz. This is not a resonator or lattice mode of the metasurface, but rather due to the substrate.

10.4 Temperature dependence eSRR on LAO

Whereas sapphire and DSO have a strong temperature dependence, the LAO substrate has a relatively constant refractive index over temperature, as shown in Figure 10.11. Therefore, we used the metasurface on an LAO substrate to determine the temperature dependence. This will show how sensitive we are to dielectric parameters and the conductivity of gold.

The temperature dependence of the resonant response of the metasurface on LAO is

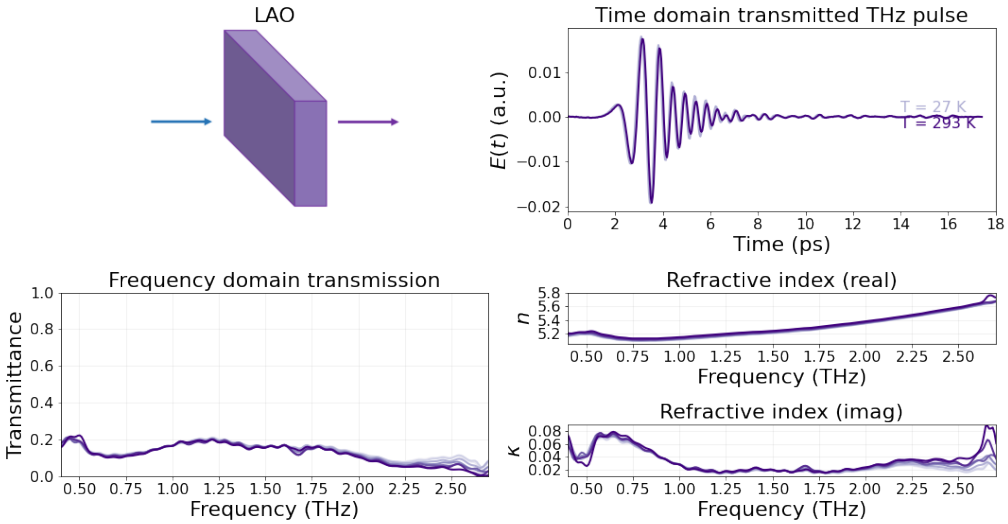

Figure 10.11: LAO substrate temperature dependence.

shown in Figure 10.12. The temperature dependence of the resonance frequency looks similar to that observed in the optimized design on sapphire (right side of Figure 10.8), but the quality factor shows a different dependence. I think this has to do with the temperature dependence of the permittivity in both substrates. The sapphire substrate shows a stronger temperature dependence in the real part of the refractive index, especially between 300 and 160 K, resulting in the big change in quality factor at high temperature that saturates at lower temperature. The LAO substrates shows a more linear temperature dependence, resulting in a square root dependence for both resonance frequency and Q factor $f_0, Q \propto \sqrt{\epsilon \propto T(K)}$.

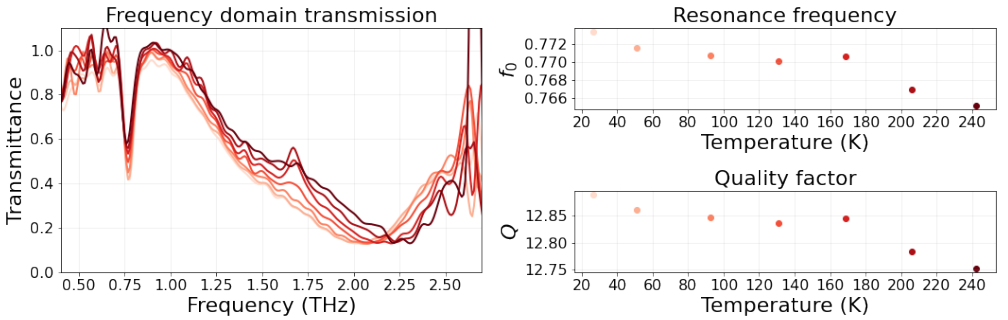

Figure 10.12: eSRR on LAO temperature dependence.

As mentioned in the subscript of Figure 10.10, the transmittance of the metasurface on LAO deviates from simulation due to a temperature dependent additional mode around 2.2 THz. In the substrate measurements, we see that the absorption coefficient is temperature dependent in this frequency range. Therefore, we think that this dip in transmission corresponds to a mode in the LAO substrate. The temperature dependence of the 2.2 THz mode for the metasurface matches the temperature dependence of the absorption coefficient of the bare LAO substrate.

10.5 Conclusion and discussion

In this chapter, we have established that the optimized design has a narrow resonant response, with strong light-matter coupling. The resulting resonant behaviour is up to 4 times stronger

than the design discussed in Part II. Both designs are sensitive to changing material properties, as studied with a temperature dependence. The optimized design is used for probing the resonant behaviour on different substrates. Even for substrates with a very limited transmittance, the resonance is resolvable. The optimized design has a resonance at 1.17 THz on a sapphire substrate, and is suitable for scaling up to resonances of 2 THz.

Part IV

Probing phase transitions

Chapter 11

Transition metal oxide $NdNiO_3$

We want to use the resonators as dielectric sensors. The simplest and most extreme test is to use a material whose dielectric function switches sign as a function of an external parameter, for example temperature: a metal-to-insulator transition (MIT). The MIT we are interested in is that of the complex oxide $NdNiO_3$ (neodymium nickelate, NNO). This material falls in the class of transition metal oxides, and more specifically the rare-earth (RE) nickelate family. So far, the phase transition mechanisms of the RE nickelates are still not well understood [67]. All theoretical predictions involve energy competition between lattice, electron, phonon and spin degrees of freedom as the main cause [68]. Understanding the underlying dynamics and interactions between these degrees of freedom may help gain insights into such phase transitions.

Terahertz spectroscopy of metasurfaces offers a great platform to study transition metal oxides (TMO), because this provides access to electronic, compositional and vibrational degrees of freedom [4]. By studying the NNO thin film on an LAO substrate with a gold metasurface deposited on top, we can verify the sensitivity to thin film dielectric properties, changing over temperature. This chapter concerns the current understanding of the metal-insulator transition in the nickelates, which will be referred back to in the discussion of the experiment in the next chapter. We first discuss the NNO perovskite structure (Section 11.1), followed by the temperature induced MIT (Section 11.2) and how electron-lattice coupling can mediate the metal-insulator transition (Section 11.3).

11.1 Perovskite structure

TMOs are composites composed of oxygen atoms which are bound to transition metal atoms as shown in Figure 11.1. The green central atom is the A cation, the B cations are blue and the O anions are indicated in red. In nickelates, the structure consists of a rare-earth A molecule (Nd for NNO) and Ni as B molecule.

These TMOs have energy bands that are only partially filled with electrons. Following Bloch theory of weakly interacting electron systems in a periodic lattice, such a material should conduct electricity and therefore be classified as a metal. If the allowed energy bands are fully filled with electrons, the compound is classified as an insulator and, conversely, if the material presents a partially filled energy band, the system is metallic. Yet, many TMOs have partially filled electron bands and are insulators, contradictory to what Bloch theory would predict [69].

The first attempt to solve this inconsistency was carried out by N. F. Mott [70, 71]. The assumption that proved to be crucial concerns electron-electron interactions, which are neglected in Bloch theory, but strongly influence the energy landscape of TMO compounds. This results in a strongly correlated system, where each electron has a complex influence on its neighbours. The strongly correlated electrons determine the electronic and physical properties of the material, but changing for example environmental conditions such as temperature or pressure can induce a transition from a metallic state to a different state of matter (insulator or superconductor) [69].

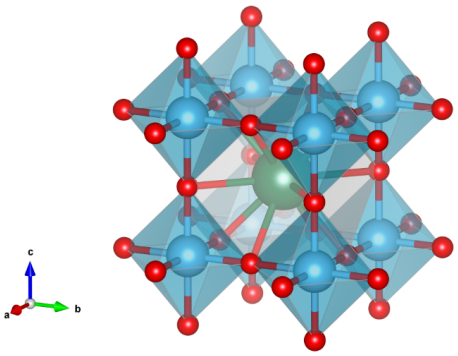

Figure 11.1: ABO_3 cubic structure. The green central atom is the A cation, the B cations are blue and the O anions are indicated in red. Figure from [69].

11.2 Metal-insulator transition

For $NdNiO_3$, the transition is bandwidth controlled by electron-lattice coupling. For Nd as the rare-earth material this is a first order metal-insulator transition. The MIT occurs at a temperature that is related to the degree of orthorhombic distortion of the unit cell. As the distortion increases, the $d-p$ orbital overlap decreases and therefore the hopping strength is reduced [72]. A more elaborate discussion of the underlying physics can be found in Appendix C.

At the transition temperature, the lattice changes from an orthorhombic to a monoclinic structure, as shown in Figure 11.2a. At high temperature, the compounds are metallic and paramagnetic, whereas the insulating ground state is antiferromagnetic.

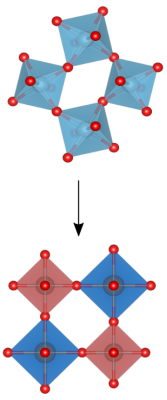

(a) Lattice over temperature

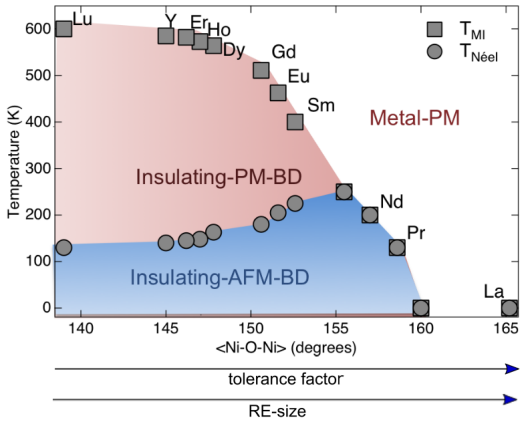

(b) Phase diagram of nickelates

Figure 11.2: MIT phase diagram of rare-earth nickelates. For decreasing temperature, the lattice changes from an orthorhombic structure to a monoclinic structure, thereby changing the orbital overlap which results in a metal-insulator transition. Both Figures from [69].

Note that the transition temperature as shown above is for bulk NNO, and will be different for heteroepitaxial films. Heteroepitaxy occurs when a film of different composition and/or crystal structure than the substrate is grown. In this case, the amount of strain in the film is determined by the lattice mismatch. Growing a thin film on a substrate will provide strain to the material [73]. For example, an LAO substrate provides 0.5% compressive strain to the material and reduces the metal-insulator-transition temperature from a bulk value of 200 K to about 130 K [74]. The hysteresis also becomes larger for deposition on a substrate [75], and is larger for thin films than for bulk NNO [76].

11.3 Control of the metal-insulator transition

Different pathways exist to externally induce a phase transition, as shown in Figure 11.3a. The lattice parameter that is relevant for this material is the Ni-O-Ni angle Θ shown in Figure 11.3b. Dependent on the rare-earth molecule, this angle is different, depending on the size of the RE metal (as shown in the horizontal axis of Figure 11.2b), but also external factors such as strain can influence this parameter. Therefore, it can be seen as an order parameter, since increasing distortion corresponds to decreasing Ni-O-Ni angle. Sufficient manipulation through for example strain or strong applied electromagnetic fields can induce a phase transition of the material. Such a phase transition can be monitored in equilibrium by studying for example the dielectric properties over temperature, but it is also possible to dynamically observe the phase transition by for example excitation in pump-probe measurements. With THz spectroscopy of our metasurface, we have access to the temperature dependent material electrodynamics and we can resolve pump-probe measurements on an ultrafast timescale.

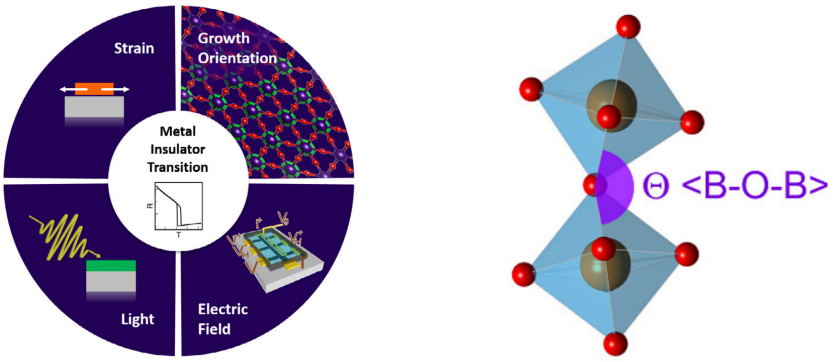

(a) MIT control (b) Bond angle Θ

Figure 11.3: Control of the metal-insulator transition from external factors. The bond angle Θ between the B cation and oxide atoms is indicated in purple in Figure (b). Changing this angle can induce a phase transition. Both Figures from [72].

By coupling the angle Θ to structural instabilities, it is possible to engineer the electronic (and magnetic) properties of the material. As explained in Section 11.2, the substrate on which an NNO film is grown can already influence the MIT in equillibrium, but it has been experimentally resolved that excitation of for example a vibrational mode in the substrate can modulate the electronic properties of the NNO thin film through propagation of dynamic distortion across the interface [73]. Figure 11.4 shows a schematic representation of how excitation of the LAO phonon mode at mid infrared frequencies (similar to the mode shown in Figure 2.3) enables dynamic control of the thin film electronic properties. As the vibrational mode in the LAO substrate is excited, the distortion propagates dynamically across the interface, exciting the NNO film into a metallic state far below the transition temperature. Understanding and engineering such couplings between structural modes in complex oxide heterostructures opens new possibilities for design and control of their scientifically fascinating and technologically useful properties.

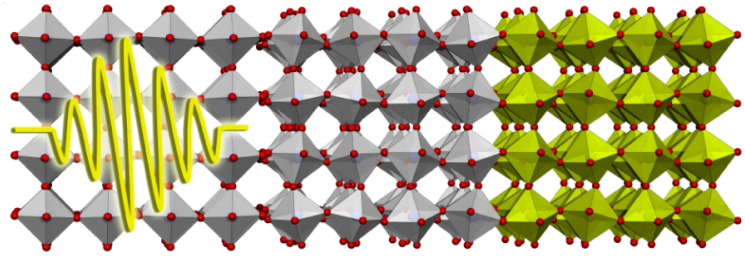

Figure 11.4: Schematic representation of the dynamic control the electronic properties of an NNO thin film via vibrational excitation of the substrate. A mid infrared pump pulse (yellow) excites the vibrational mode of the LAO substrate (grey) that creates a distortion in the NNO film (green), inducing the material into the metallic state at temperatures far below the transition temperature. Figure from [73].

Chapter 12

THz spectroscopy of $NdNiO_3$

For this thesis, the goal of the $NdNiO_3$ (NNO) measurements is to verify the thin film sensitivity, whether we can still resolve a resonance, and whether it is possible to capture the metal-insulator transition of NNO. The metasurface of gold eSRR is patterned on an NNO thin film of approximately 10 unit cells (u. c.) thickness with a 500 um $LaAlO_3$ (LAO) substrate as shown in Figure 12.1. First we compare the resonance observed far below the transition temperature and far above the transition temperature with simulations for the eSRR on LAO. After this, we will compare two measurement procedures: the bare NNO/LAO thin film, and with eSRR deposited on the thin film.

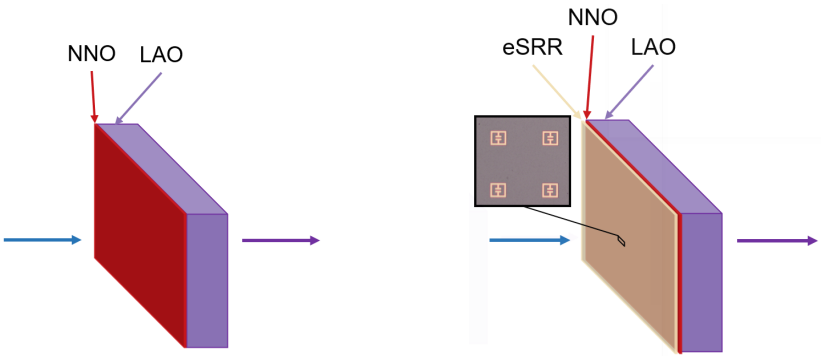

(a) Bare film (b) With resonators

Figure 12.1: Measurement approach for thin film characterization of NNO thin film on 500 um LAO substrate. The metasurface in (b) consists of gold eSRRs of the optimized design, scaled with $s = 0.8$ for a resonant response at approximately 1 THz.

We scaled the optimized design to a resonant response at approximately 1 THz by scaling the geometric parameters (all except the resonator thickness) from Table 10.1 with $s = 0.8$. The 10 u.c. NNO thin film is only $\sim$ 3.82 nm thick. We know from the out of plane field distribution studied in Chapter 6.5 (Figure 6.10) that the metasurface is sensitive to substrate parameters down to tens of microns into the substrate, and that the interaction strength decays exponentially. In the insulating state, we therefore expect that the NNO thin film barely perturbs the interaction, and that the resonant state is mainly determined by the LAO permittivity. In the metallic state above the transition temperature, we expect the capacitor gap to be shorted and the resonance to disappear.

The nanometer thickness of the film makes it hard to simulate the metasurface on NNO/LAO for comparison, since the required nanometer size mesh for such thin films will take days to simulate. Therefore we compare the experimental result to simulation of eSRR on LAO without the NNO thin film. As can be seen in Figure 12.2, our experimental results match our predictions. At 17 K, the resonance shows a striking resemblance to the simulated spectrum for eSRR on LAO, whereas the resonance has completely disappeared for the measurement

at 172 K.

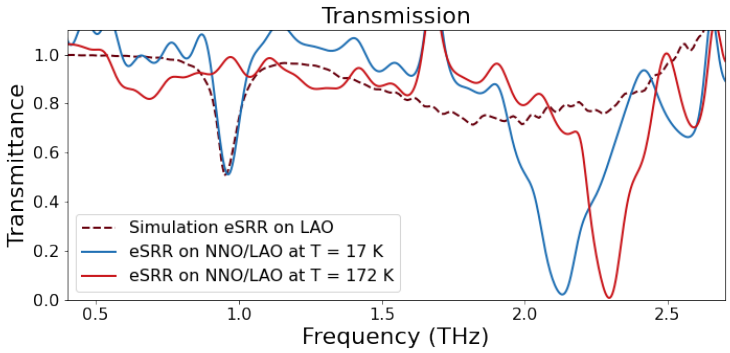

Figure 12.2: Analysis in the frequency domain of experimental response of eSRR sample on NNO/LAO substrate. Below the transition temperature, the experimental result (blue solid line) matches the simulated resonance for eSRR on LAO (dashed dark red). Above the transition temperature (red solid line) the resonance disappears completely. Experimental results are divided by bare NNO/LAO film as a reference. Simulation is with an LAO substrate as a reference.

We again observe a temperature dependent mode around 2.2 THz, also observed for the metasurface measurement of gold eSRR directly on LAO (without NNO, see Figure 10.12), which corresponds to the temperature dependent absorption coefficient of LAO (see Figure 10.11). The fact that the mode does not disappear along with the LC resonance for temperatures above the transition temperatures again leads to the conclusion that this mode is a property of the LAO substrate, and does not depend on the persistence of a resonant response. The mode does not scale with the resonator geometry, since the frequency of the mode has not changed with respect to the measured response for the metasurface without an NNO thin film (Figure 10.12). However, the mode does appear much narrower than for the eSRR on LAO. In Ref [77], it is speculated that the mode possibly originates from multiple phonon processes, similar to oscillations observed in MgO [78].

12.1 Time-domain THz probing of MIT

To verify the thin film properties, we first measure the film without resonators (approach shown in Figure 12.1a). This can be considered as a 'bulk' measurement in the sense that the response is averaged over spatial length scales. Even though the interaction is still governed by molecular properties, the electrodynamic properties of a sample are averaged over macroscopic length scales, on the order of the probing frequency. This is different from our metasurface response, since the metasurface is mainly sensitive to the dielectric function inside the capacitor gap. The metasurface therefore measures the response averaged over the $\sim 10\ \mu\text{m} \times 1\ \mu\text{m}$ regions inside the capacitor gaps, whereas the bare film gives the response on a length scale set by the probing frequency (∼0.3 mm) and the THz beam width (∼1 mm diameter). This difference in length scales may result in a difference in sensitivity to nucleation. $NdNiO_3$ is known to form inhomogeneous regions (as can be expected for a first order phase transition), where some regions already display insulating behaviour and others are still metallic [79]. The bare film measurement will not be sensitive to regions smaller than the probing frequency, whereas the metasurface is sensitive to even smaller regions.

Already from the time-domain transmitted THz pulse we can determine the critical temperature and hysteresis of the metal-insulator transition. In the metallic state, the NNO film is mainly reflective, and only a small portion of the THz beam is transmitted. In the insulating state, a significantly larger portion will be transmitted. By integrating the time domain electric field $E(t)$ over time t, we can obtain the transmitted power P_T, integrating along the parametric curve (numpy trapz function) defined as:

$$P_T = \int_t \left| E(t) \cdot 10^8 \right|^2 dt \tag{12.1}$$

where the multiplication with 10^8 merely serves to obtain the response in units on the order of 1, and its temperature dependence will reveal the MIT.

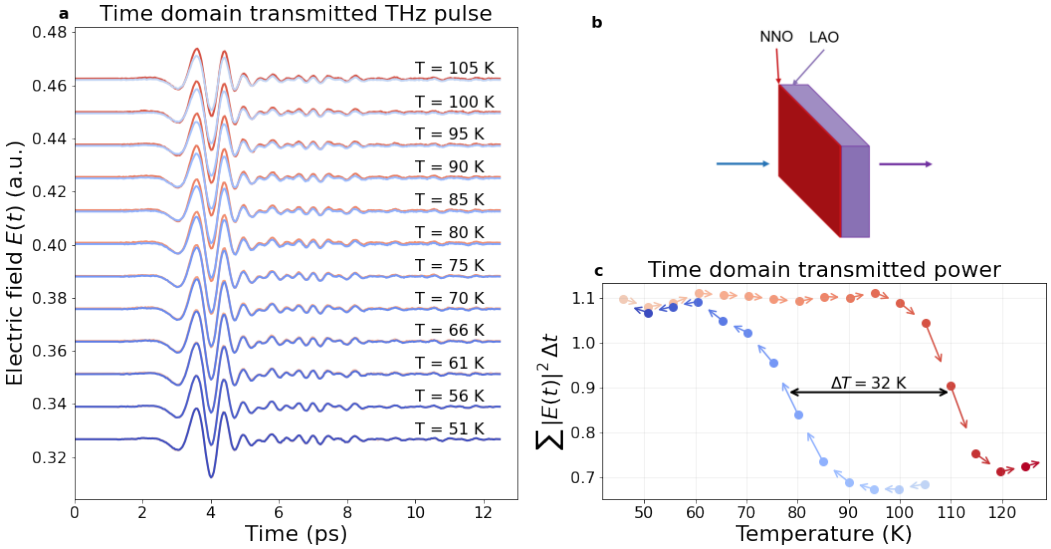

Figure 12.3: Time-domain analysis of bare NNO film (measured as shown in Figure 12.1a and subplot (b)). The time domain transmitted pulses (a) are offset with respect to their respective temperatures for clarity. At higher temperatures, it is clearly visible that the state differs between cooldown and warmup experiments, also visible from the hysteresis loop in the transmitted power (c). The hysteresis loop has a width of approximately 32 K, and a transition temperature around $T \approx 78$ K.

From the time domain transmitted power we can visualize the transition temperature and the hysteresis loop (see Figure 12.3), indicating a first order phase transition. The transition temperature is defined as the temperature at the maximum slope of the cooldown curve, with a value of approximately 78 K. In Reference [80], the transition temperature (here defined as the temperature which gives the peak of the activation energy on warming) has a value of 120 K for NNO (film thickness $\sim$ 100 u.c.) on LAO.

12.1.1 Frequency domain interpretation

Interpretation of the power intensity in the time-domain provides information on the MIT averaged over the full spectral weight, with a bandwidth determined by our THz pulse bandwidth. By interpreting the same data in the frequency domain, it is possible to determine the spectral weight transfer: whether the MIT is the same at specific frequencies with respect to the time-domain response which is averaged over all frequencies. This allows us to determine to what extend we can relate the metasurface response to bare film measurements, since the resonant approach is determined at one specific frequency (the resonance frequency) rather than averaged over the full bandwidth.

The resulting spectra for the bare NNO film are shown in Figure 12.4. The frequency domain transmission changes with temperature as expected. If we look at the transmitted field at specific frequencies, the same MIT is observed as for the time domain analysis shown in Figure 12.3, except for frequencies in the vicinity of the substrate mode around 2.2 THz.The low spectral weight and temperature dependent mode perturb the obtained values for the MIT. Also for low frequency (f = 0.5 THz), the obtained MIT is subject to more noise than for higher frequencies. This could also be caused by the small dip in transmission around 0.6 THz,

or due to the low spectral weight of the reference pulse due to our limited THz bandwidth. Overall, these relatively small perturbations at high and low frequency do not perturb the overall determined values for the MIT, since the averaged (time-domain integrated) response nicely matches the response at for example 0.75, 1.0 and 1.25 THz.

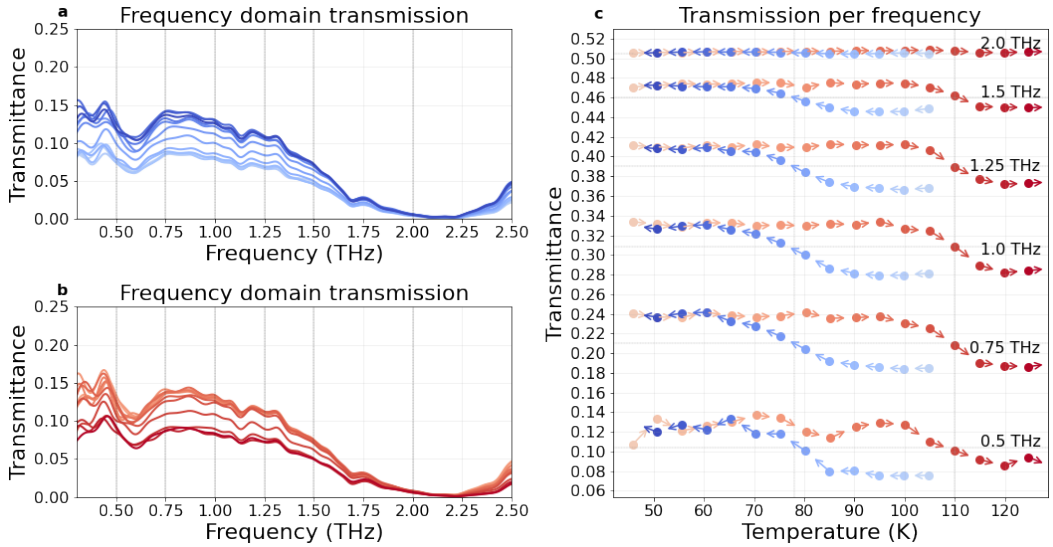

Figure 12.4: Frequency domain analysis of bare NNO film, obtained by Fourier transforming the time-domain measurements shown in Figure 12.3a and dividing by a reference scan without sample. (a) Transmittance upon cooling. (b) Transmittance upon warming. (c) Transmission revealing MIT for specific frequencies (corresponding to frequencies indicated by grey lines in (a) and (b)). The transmission spectra are offset with respect to their respective frequencies for clarity. This shows that spectral weight transfer is not an issue, except for frequencies in the vicinity of the substrate mode around 2.2 THz.

12.2 Metasurface probing of MIT

We want to compare the results obtained for the bare NNO film with eSRR measurements. We expect that the broadband response should not change significantly, except for frequencies close to the resonance frequency, and for frequencies around the temperature dependent substrate mode (see Figure 12.2). Similar to the procedure for the analysis of the bare film, we interpret the time-domain response by integrating the electric field over time to obtain the transmitted power P_T with Equation 12.1. Already in the time-domain, shown in Figure 12.5b it is clear that the obtained response is significantly different in several aspects:

- The transition temperature and hysteresis loop are clearly visible, but remarkably at a higher transition temperature.
- The hysteresis loop width is smaller than for the bare NNO film.
- The warming curve is similar in slope, but at 10 K higher temperature with respect to the bare NNO measurement.
- The cooling curve has a steeper slope, and occurs at 20 K higher temperature with respect to the bare NNO measurement.
- Instead of saturating at $P_T \approx 1.1$, the transmitted power obtains a downward slope with lower temperature in the insulating state.

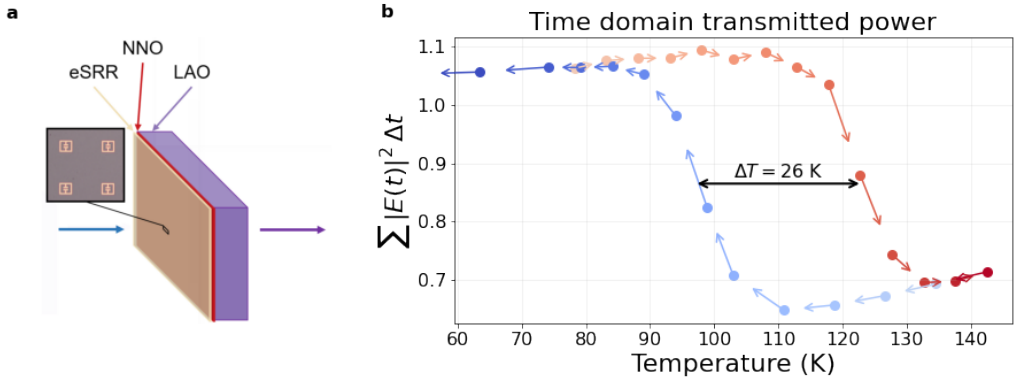

Figure 12.5: Time-domain analysis of metasurface measurement of gold eSRR on NNO/LAO. (a) Measurement approach. (b) Time domain transmitted power. The hysteresis loop has a width of approximately 26 K, and a transition tempature around $T \approx 97$ K, higher than for the bare NNO film. The hysteresis loop is smaller than for the bare NNO film. Instead of saturating at $P_T \approx 1.1$, the transmitted power shows a small decrease below 84 K upon cooling and 107 K upon warming.

The differences between these measurements could be due to experimental limitations of the sensitivity of our temperature sensor, or the metasurface deposition has changed the intrinsic properties of the NNO film, therefore perturbing the metal-insulator transition, or the persistence of the resonance perturbs the overall THz response. In the following paragraphs, different external and internal parameters are discussed, including their impact on the MIT. From these discussions, we then conclude that changes of the intrinsic properties are highly unlikely, and the difference is due to the perturbed THz response from spectral weight transfer due to the persistence of the resonance. First we discuss possible changes to the intrinsic NNO film from strain, fluctuations or due to the enhanced response at resonance.

Strain Tensile strain results in a higher MIT transition temperature, similar to replacing the Nd atoms with a smaller size rare earth material (see Figure 11.2b) [67]. For tensile strain on thin films, the Néel transition gets separated from the MIT, unlike the bulk where $T_{\mathrm{N}} = T_{\mathrm{MIT}}$. Compressive strain gives a similar result to providing hydrostatic pressure, and the MIT is completely quenched such that optimally prepared thin films under high pressure are completely metallic [81]. The metasurface measurements are on the same NNO/LAO sample. Since the NNO film is only a few nanometers thick, we can imagine that depositing 150 nm of gold on top can influence the very sensitive lattice ordering. However, we can exclude strain induced perturbations, since these are determined by the growth procedure of the NNO film itself, and it is unlikely that deposition of gold on top perturbs this significantly.

Fluctuations The smaller hysteresis loop could indicate a transition from first- to second order phase transition [74]. According to Catalano et.al., the absence of a visible hysteresis loop, initially interpreted as a signature of a second-order transition, is more likely due to increased thermal fluctuations reducing the size of the hysteretic effect as T_{MIT} is shifted to higher temperatures [72]. Both can be interpreted as a result of additional tensile strain [67], but are unlikely caused by deposition of the metasurface.

Resonant response induced effects The metasurface measurement is sensitive to the dielectric function of the substrate inside the capacitive gap. Locally, the induced currents at resonance may result in heating, and result in local strong electric and magnetic fields. The resistivity curves and T_{MIT} of NNO are, in essence, insensitive to the application of magnetic fields of up to 4 T [82], suggesting that the nickelate behavior is extremely robust against magnetic field, which, in turn, suggests magnetoresistive effects should be small [72].

Therefore, we exclude magnetic field dependencies as a possible explanation for the observed difference in MIT.

External perturbations by applied (electric) fields are known to have a significant influence on the MIT, both in terms of temperature and hysteresis loop. Electric (DC) fields will decrease the transition temperature and increase the hysteresis loop (for an 8 u.c. NNO film on LAO) [74]. Excitation with an NIR pump results in excitation into metallicity for the insulating state, and results in higher dissipation for the metallic state [68]. Excitation of a substrate phonon mode will also excite the insulating state into metallicity [73]. In SRR metasurface measurements of VO_2 [83], they used the intense THz electric fields to excite the insulating state into a metallic state, but with much higher incident field on the order of MV/cm^{-1} (in this thesis, the incident field is on the order of 1 kV/cm^{-1}).

All of these electric field induced perturbations would result in a decrease of the transition temperature and increase in hysteresis loop width. Since this is exactly opposite to what we see, we exclude the option that the resonant response is responsible for the change in MIT parameters.

Spectral weight transfer From the time-domain transmitted power, we see that whereas the transmitted power saturated around $P_T \approx 1.1$ for the bare NNO film, now there is a small decrease in transmission below the transition temperature. This can be explained by spectral weight transfer in the insulating state: the persistence of the resonance perturbs the overall transmitted field, since the transmission decreases around the resonance frequency. We can confirm the relation to the spectral weight transfer by looking at the frequency domain analysis, shown in Figure 12.6.

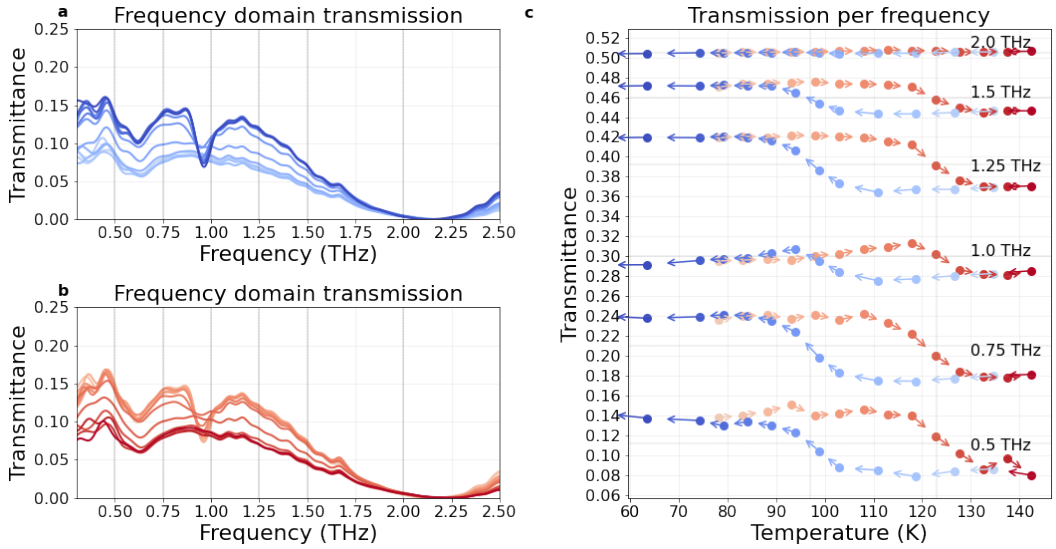

Figure 12.6: Frequency domain analysis of metasurface on NNO/LAO, obtained by Fourier transforming the time-domain measurements shown in Figure 12.3a and dividing by a reference scan without sample. (a) Transmittance upon cooling. (b) Transmittance upon warming. (c) Transmission revealing MIT for specific frequencies (corresponding to frequencies indicated by grey lines in (a) and (b)). The transmission spectra are offset with respect to their respective frequencies for clarity. For frequencies close to the resonance frequency (such as 1.0 THz), an additional kink is visible both in warmup and cooldown, corresponding to the temperature below which the resonance appears, hence corresponding to the temperature where the NNO switches from a metallic (above this temperature) to an insulating state (below this temperature). The same MIT is visible at the other frequencies, now saturating in power in the insulating state.

If we look at the transmission at specific frequencies, we see that for frequencies far

from the resonance frequency, the transmission indeed saturates, instead of decreasing for temperatures below the transition temperature. Around the resonance frequency (at 1 THz), the increase in transmitted power is suddenly cut off at 94 K and 117 K upon cooling and warming, respectively. This corresponds to the decrease in transmission from the resonance in the insulating state. The portion of the transmitted field that is 'lost' to the resonance (now reflected or absorbed due to the resonant response) becomes larger with decreasing temperature, corresponding to a higher figure of merit of the resonance. This is consistent with the downward slope in transmission with decreasing temperature.

12.3 Resonant response of metasurface

So far, we have looked at the broadband response of the eSRR on NNO/LAO sample. We can interpret the resonant response by its resonance frequency, quality factor and figure of merit, shown in Figure 12.7. The structures can only exhibit a resonant response for dielectrics with a conductivity below a certain (undetermined) threshold [83]. Above this threshold, we expect the capacitive gap to be shorted and the resonance to disappear. This threshold corresponds to the temperatures below which the transmission at 1 THz is decreasing with decreasing temperature (see Figure 12.6c).

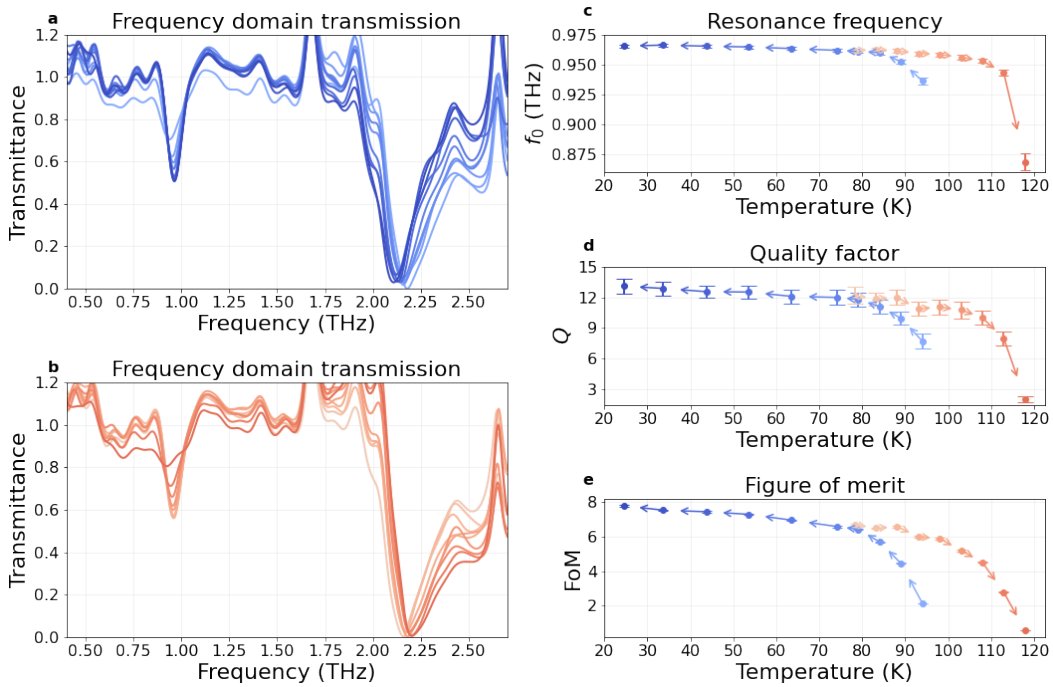

Figure 12.7: Resonance extraction in the insulating state. Spectra in (a) and (b) are divided by the blanket NNO film measurement at 20 K as a reference. (a) Frequency domain transmission upon cooling down. (b) Frequency domain transmission upon warming up. (c) Resonance frequency. (d) Quality factor of the resonance. (e) Figure of merit, rendering the spectral weight under the resonance in arbitrary units. Errorbars in (c), (d) and (e) indicate fitting errors.

To compare the sensitivity of our resonant response with the sensitivity of the broadband response, we compare two sets of temperature points, where each set consists of a pair of temperature points that have the same resonant response, one from the cooling sweep and one from warm up. The first set is outside the hysteresis loop, in the saturated insulating response. If we plot the transmission on top of each other, we see that not only the resonant response is the same, but also the broadband response (except for slight deviations around

the 2.2 THz mode due to the difference in temperature).

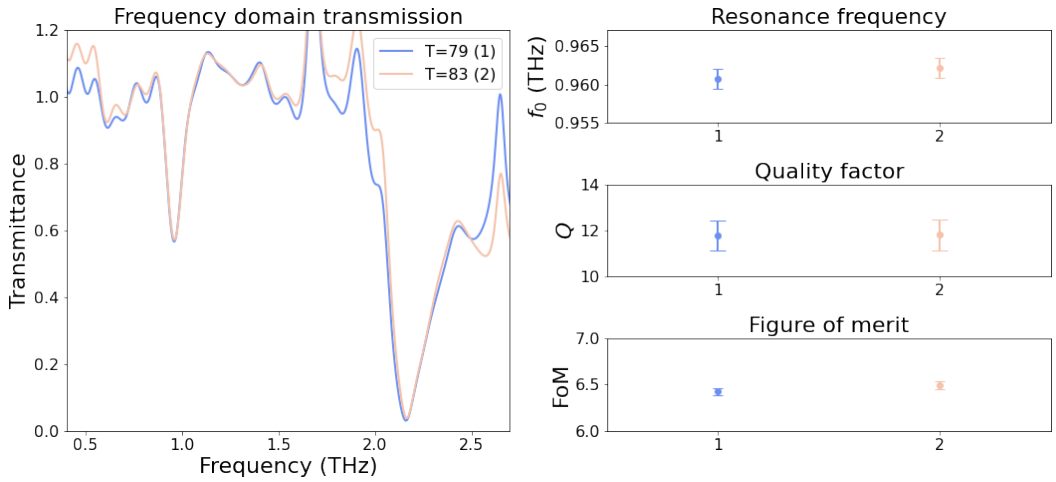

Figure 12.8: Comparison of two temperature points (set 1), from cooling (1) and warming (2) at temperatures below the hysteresis loop. Both the resonant response and broadband response are the same, consistent with a similar sensitivity in conductivity between methods.

The second set is for temperatures in the hysteresis loop, where we are closer to the conductivity threshold of the resonant response. Near the transition the persistence of the resonant response (corresponding to this conductivity threshold) seems different upon cooling than upon warming. Even though the resonant response is the same, the broadband conductivity is lower for the warming curve than for the cooling curve (higher conductivity corresponds to lower transmission). We can relate this to the nanoscale evolution of the MIT.

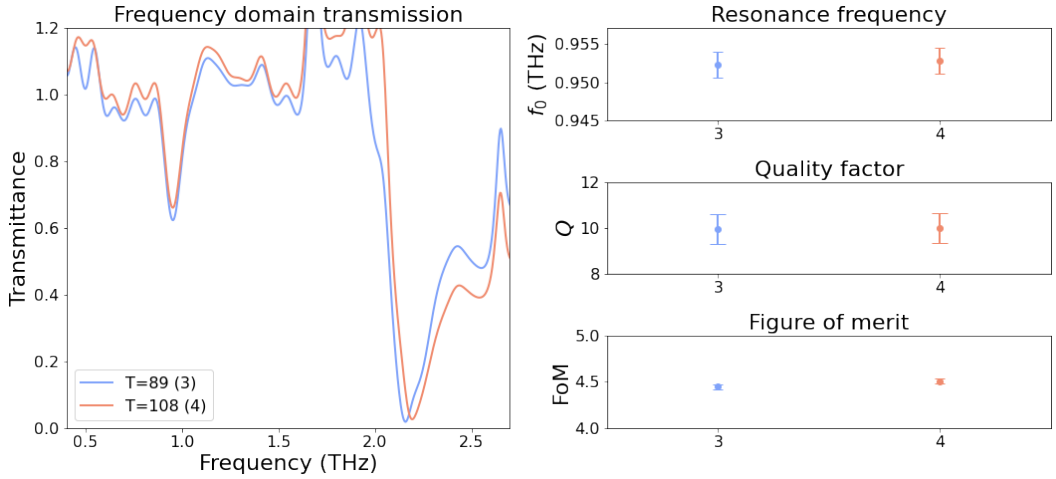

Figure 12.9: Comparison of two temperature points (set 2), from cooling (3) and warming (4) at temperatures inside the hysteresis loop. The resonant responses are the same, but the broadband response shows a higher conductivity for the cooldown curve with respect to the warmup curve.

Nanoscale evolution The coexistence of metallic and insulating regions in the vicinity of the MIT is typical of first-order phase transitions. In Reference [76], the local properties over the transition are studied. Their study shows that the MIT hysteresis is preserved down to the single domains, with locally different transition temperatures than the observed in

bulk measurements, shown in Figure 12.10. The distribution of transition temperatures is a local property, set by surface morphology and stable across multiple temperature cycles [76]. Upon cooling, the insulating domains grow along the surface terraces of the substrate, which act as nucleation centres for the insulating phase. The domains preferably grow along the edges of the domains, resulting in a striped shape. This also relates to the local strain. The local periodic strain field at the step edges can confine the insulating phase on the terraces, limiting its expansion [74]. The reverse transition upon warming, into the metallic state is rather different. The disappearance of the insulating domains is a homogeneous melting that originates from the domain edges [76]. Whereas the striped domains upon cooling can extend up to millimetres in width, the metallic domains upon warming appear to be evenly distributed over the surface, in sizes of the order of a few tens of nanometres.

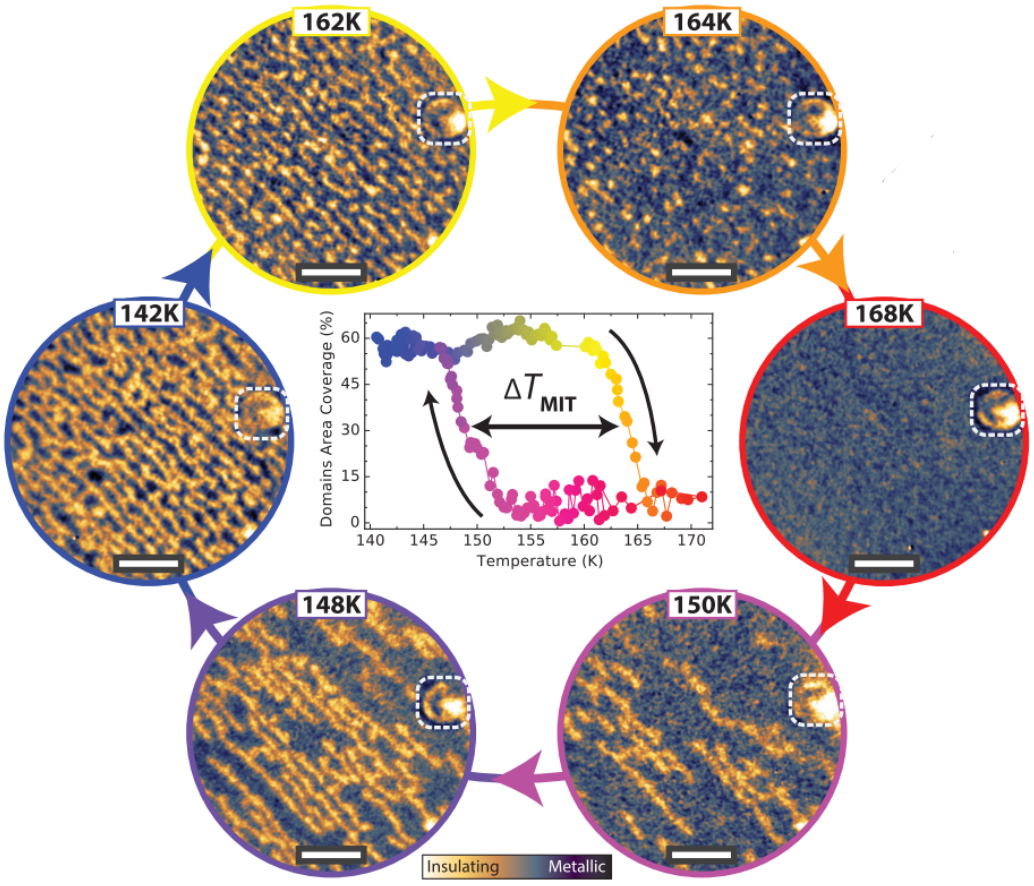

Figure 12.10: Temperature evolution of insulating domains across the MIT. The insulating domains nucleate and grow on cooling, while they gradually disappear on warming. The inner panel shows the percentage of image area covered by the insulating domains as a function of temperature. The measurement upon warming at 164 K and cooling at 150 K have the same insulating area coverage, but the domain sizes are different. Upon cooling, the domains nucleate along substrate terrace edges whereas upon warming they 'melt' down to nanometre size regions. Scale bar, 1 µm. Figure from [76].

We can relate this to the difference in conductivity observed by the metasurface. The micrometre size grains are much smaller than the wavelength, so we will not observe this difference from the broadband interpretation. However, the capacitive gap size is on the order of the striped domain size upon cooling, and oriented along the structural domain edges of the LAO substrate. This could explain why we observe the same resonant response at different broadband conductivity for temperatures inside the hysteresis loop.

12.4 Conclusion and discussion

In this chapter, we have established that our metasurface is sensitive to thin film properties by probing the metal-insulator transition of a 10 u.c. $NdNiO_3$ film over temperature. The metasurface is sensitive to changes in dielectric constant and conductivity, up to a threshold value of substrate conductivity above which the capacitive gap is shorted and the resonant response disappears. With our metasurface resonant response, we are able to obtain similar (to possibly even better) resolution with respect to broadband THz spectroscopy. In the last section, we speculate on the possibility that the metasurface is sensitive to micron-scale insulating domain formation over the MIT, but the current results are too limited to confirm this hypothesis. First, by repetitive measurement of the same sample, we can exclude offsets in temperature read-out and saturation of the sample temperature for each point over the transition. By compensating for the spectral weight transfer due to the persistence of the resonance, it would be possible to better compare between broadband and resonant approaches. Further on, measuring several samples would help in exclusion of perturbation of the NNO film upon resonator deposition.

All in all, we have established that the optimized metasurface is sensitive to changes in material electrodynamics. The resonant response can be predicted by simulation, and set to a specific resonance frequency without giving in on resonance quality. The resonant response can be related to dielectric and (super)conducting material properties, with an outlook on transient studies from the enhanced nonlinear response for intense THz incident beams in the capacitor gap.

Appendix A

Resonator fabrication and dimensions

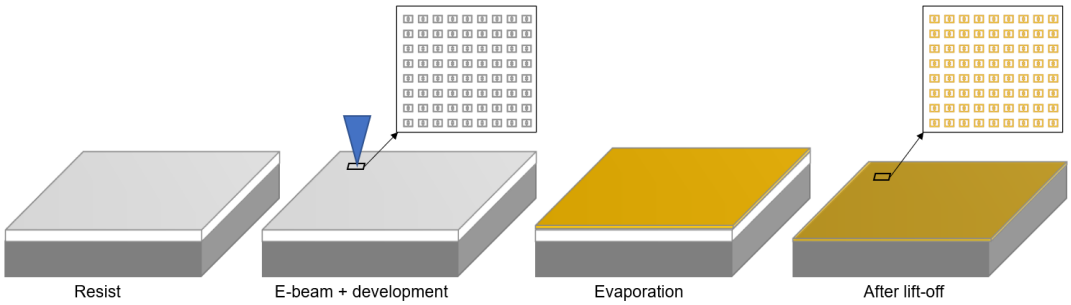

Figure A.1: **Resonator fabrication.** First, an e-beam resist layer (PMMA, white) is deposited on the sample (500 um substrate, dark grey). The resist is exposed by the e-beam writer (blue) which follows the resonator design (inset in grey, provided in an autocad file), thereby exposing the sample where the gold will fill the resonator geometry. After this, the resist layer is developed, removing the exposed parts. Subsequently, a 5 nm layer Titanium plus 150 nm layer of gold is deposited by evaporation (gold). Finally, the sample is immersed in acetone to liftoff the resist.

	Initial design Au on AO	Optimized simulation	Optimized Au on AO	Optimized Au on DSO	Optimized Au on LAO
lx [um]	19.2	25	25.3	25.4	25.16
ly [um]	23.7	22.5	22.6	22.94	22.66
w [um]	2.5	3	3.24	3.8	3.31
g [um]	1.7	1.5	1.29	0.82	1.19
c [um]	6.8	10	10.25	10.67	10.27
px [um]	36	82.3	82.2	78.9	82.3
py [um]	26	82.3	82	78.9	82.3
dres [nm]	50	150	150	150	150

Figure A.2: Resonator dimensions of simulated and experimental designs.

Appendix B

Resonance characterization dipole at vertical incident field

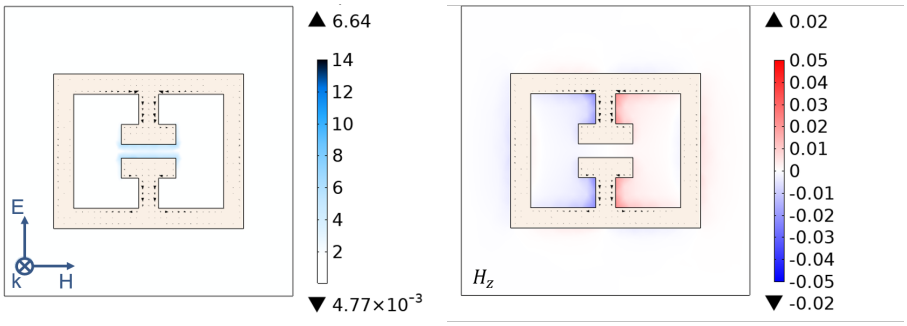

Figure B.1: Simulation of electric field norm, surface current density and out of plane magnetic field at the dipole resonance (vertical polarized incident electric field) (2.31 THz).

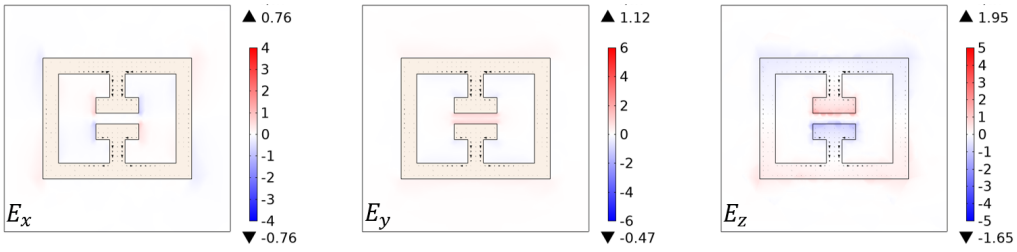

Figure B.2: Simulation of electric field in x, y and z direction, and surface current density at the dipole resonance (vertical polarized incident electric field) (2.31 THz). The x and y components are evaluated at the metasurface, whereas the z component is evaluated 10 nm below the surface in the substrate (the out of plane components are zero at the transition boundary corresponding to the resonator).

Appendix C

Competing energy scales in transition metal oxides

The Hubbard model describes electrons moving in a periodic lattice, with a single level at each site, and forming a single electronic band. As electrons hop from site i to site j, the system is left with one unoccupied i site and a doubly occupied j site.

The interaction between electrons is incorporated in a Hamiltonian from the Hubbard model:

$$\mathcal{H} = -t \sum_{(i,j),\sigma} \hat{c}^{\dagger}_{i,\sigma} \hat{c}_{j,\sigma} + U \sum_{i} \hat{n}_{i,\uparrow} \hat{n}_{i,\downarrow} \tag{C.1}$$

where t is the intersite hopping parameter, $\hat{c}^{(\dagger)}_{i,\sigma}$ is the second quantization operator that creates (annihilates) an electron with spin σ on a lattice site i, U the Coulomb interaction, and $\hat{n}_{i,\sigma} = \hat{c}^{\dagger}_{i,\sigma} \hat{c}_{i,\sigma}$ is the spin density operator. The first term represents the intersite hopping of electrons and the second one takes into account the onsite electron repulsion [72]. The energy associated with double occupancy of a site is incorporated as the Coulomb interaction U, and the intersite hopping energy is determined by the hopping parameter t.

In normal metals, $t \gg U$ and the electronic states are delocalized. The material therefore is able to conduct electricity. If the Coulomb energy U is much larger than the hopping amplitude t, the electrons are localized and the material is insulating. For TMOs, these parameters are close in energy, resulting in competition between insulating and metallic behaviour. The Zaanen, Sawatzky and Allen scheme (ZSA) enables us to distinct two types of strongly correlated insulators [84], shown in Figure C.1a. The division is based on the energy scales involved. For some B cations, the orbital overlap between the d orbital of the B atom and the p orbital of the O atoms becomes relevant. The energy required to transfer charge between these orbitals is defined as the charge transfer gap Δ. So far we discussed Mott insulators, for which the Coulomb energy is smaller than the charge transfer gap. If the Coulomb repulsion energy U is stronger than the charge transfer gap energy Δ, the material is classified as CT insulator. As the overlap between the p states and the d orbitals is decreased, the gap opens and a MIT occurs [69].

For TMO compounds, two pathways exist to control the electron-electron interactions: either the electron correlation strength, proportional to the ratio between Coulomb energy and bandwidth is increased, or the occupation number (filling) is varied [69]. The phase diagram for such a transition is shown in Figure C.1b. The MIT of $NdNiO_3$ is bandwidth controlled. Changing the Ni-O-Ni angle changes the d-p orbital overlap. Above the transition temperature, this material is in a metallic state, transitioning to a a charge-transfer insulator below the critical temperature.

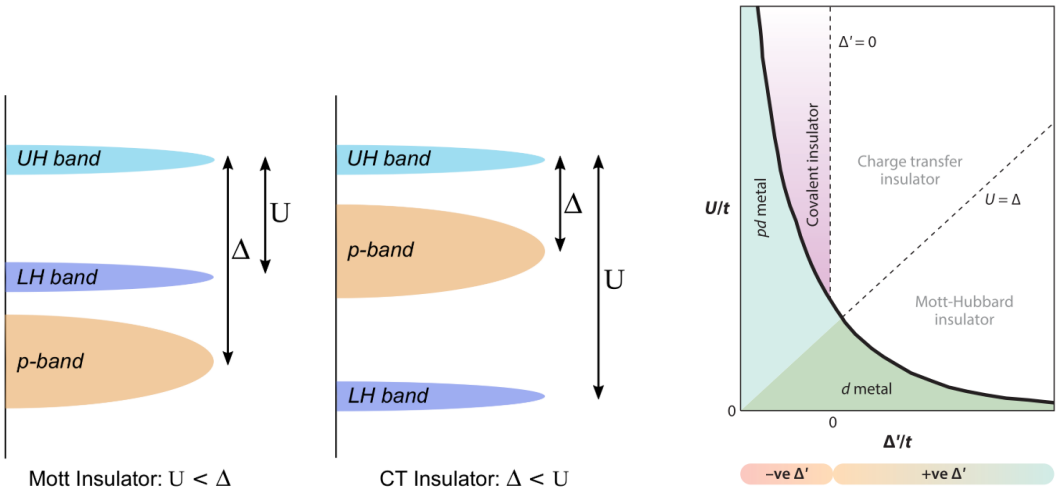

(a) Figure from [69]

(b) Figure from [67]

Figure C.1: Energy scales in NNO

Bibliography

[1] D. N. Basov, Richard D. Averitt, Dirk Van Der Marel, Martin Dressel, and Kristjan Haule. Electrodynamics of correlated electron materials. *Reviews of Modern Physics*, 83(2):471–541, 2011.

[2] X. C. Zhang and Jingzhou Xu. *Introduction to THz wave photonics*. Springer, 2010.

[3] Terahertz waves - das-nano. `https://www.das-nano.com/terahertz-waves/`. Accessed: 28-05-2021.

[4] J. Zhang and R. D. Averitt. Dynamics and control in complex transition metal oxides. *Annual Review of Materials Research*, 44:19–43, 2014.

[5] Safa Kasap and Peter Capper. *Handbook of Electronic and Photonic Materials*. Springer, 2 edition, 2017.

[6] A. Pashkin, M. Porer, M. Beyer, K. W. Kim, A. Dubroka, C. Bernhard, X. Yao, Y. Dagan, R. Hackl, A. Erb, J. Demsar, R. Huber, and A. Leitenstorfer. Femtosecond response of quasiparticles and phonons in superconducting YBa2Cu3O7-δ studied by wideband terahertz spectroscopy. *Physical Review Letters*, 105(6), 2010.

[7] Dominik M. Juraschek, Tomáš Neuman, Johannes Flick, and Prineha Narang. Cavity control of nonlinear phononics. *arXiv*, (c):1–8, 2019.

[8] M. A. Ordal, Robert J. Bell, R. W. Alexander, L. L. Long, and M. R. Querry. Optical properties of fourteen metals in the infrared and far infrared: Al, Co, Cu, Au, Fe, Pb, Mo, Ni, Pd, Pt, Ag, Ti, V, and W. *Applied Optics*, 24(24):4493, 1985.

[9] Stefan Linden, Christian Enkrich, Martin Wegener, Jiangfeng Zhou, Thomas Koschny, and Costas M. Soukoulis. Magnetic Response of Metamaterials at 100 Terahertz. *Science*, 306(5700):1351–1353, 2004.

[10] Jerzy Krupka, Richard G. Geyer, Johann Heyen Hinken, and Matthias Kuhn. Dielectric Properties of Single Crystals of A1203, LaAI03, NdGa03, SrTi03, and MgO at Cryogenic Temperatures. *IEEE Transactions on Microwave Theory and Techniques*, 42(10):1886–1890, 1994.

[11] J. B. Pendry, A. J. Holden, D. J. Robbins, and W. J. Stewart. Magnetism from conductors and enhanced nonlinear phenomena. *IEEE Transactions on Microwave Theory and Techniques*, 47(11):2075–2084, 1999.

[12] W. J. Padilla, M. T. Aronsson, C. Highstrete, Mark Lee, A. J. Taylor, and R. D. Averitt. Electrically resonant terahertz metamaterials: Theoretical and experimental investigations. *Physical Review B - Condensed Matter and Materials Physics*, 75(4):1–4, 2007.

[13] Hou-Tong Chen, John F. O'Hara, Antoinette J. Taylor, Richard D. Averitt, Clark Highstrete, Mark Lee, and Willie J. Padilla. Complementary planar terahertz metamaterials. *Optics Express*, 15(3):1084, 2007.

[14] T. J. Yen, W. J. Padilla, N. Fang, D. C. Vier, D. R. Smith, J. B. Pendry, D. N. Basov, and X. Zhang. Terahertz Magnetic Response from Artificial Materials. *Science*, 303(5663):1494–1496, 2004.

[15] W. J. Padilla, A. J. Taylor, C. Highstrete, Mark Lee, and R. D. Averitt. Dynamical electric and magnetic metamaterial response at terahertz frequencies. *Physical Review Letters*, 96(10):1–4, 2006.

[16] Jiangfeng Zhou, Thomas Koschny, and Costas M. Soukoulis. Magnetic and electric excitations in split ring resonators. *Optics Express*, 15(26):17881, 2007.

[17] C. Enkrich, M. Wegener, S. Linden, S. Burger, L. Zschiedrich, F. Schmidt, J. F. Zhou, Th Koschny, and C. M. Soukoulis. Magnetic metamaterials at telecommunication and visible frequencies. *Physical Review Letters*, 95(20):5–8, 2005.

[18] W. J. Padilla. Group theoretical description of artificial magnetic metamaterials utilized for negative index of refraction. *Optics Express*, 15(1):1–5, 2007.

[19] D. Schurig, J. J. Mock, and D. R. Smith. Electric-field-coupled resonators for negative permittivity metamaterials. *Applied Physics Letters*, 88(4):1–3, 2006.

[20] Chun Li, Jingbo Wu, Shoulu Jiang, Runfeng Su, Caihong Zhang, Chengtao Jiang, Gaochao Zhou, Biaobing Jin, Lin Kang, Weiwei Xu, Jian Chen, and Peiheng Wu. Electrical dynamic modulation of THz radiation based on superconducting metamaterials. *Applied Physics Letters*, 111(9), 2017.

[21] Metamaterials — circuit metamaterials. `http://people.ee.duke.edu/~drsmith/metamaterials/metamaterial_elements.htm`. Accessed: 18-06-2021.

[22] Maik Scheller. Data extraction from terahertz time domain spectroscopy measurements. *Journal of Infrared, Millimeter, and Terahertz Waves*, 35(8):638–648, 2014.

[23] Ingrid Wilke and Suranjana Sengupta. Nonlinear Optical Techniques for Terahertz Pulse Generation and Detection—Optical Rectification and Electrooptic Sampling. *Medical Group Management*, 28(1):46–48, 1981.

[24] A. Tomasino, A. Parisi, S. Stivala, P. Livreri, A. C. Cino, A. C. Busacca, M. Peccianti, and R. Morandotti. Wideband THz time domain spectroscopy based on optical rectification and electro-optic sampling. *Scientific Reports*, 3:1–8, 2013.

[25] W. Zouaghi, M. D. Thomson, K. Rabia, R. Hahn, V. Blank, and H. G. Roskos. Broadband terahertz spectroscopy: Principles, fundamental research and potential for industrial applications. *European Journal of Physics*, 34(6), 2013.

[26] S. Vidal, J. Degert, M. Tondusson, E. Freysz, and J. Oberlé. Optimized terahertz generation in ZnTe crystals. *International Conference on Infrared, Millimeter, and Terahertz Waves, IRMMW-THz*, 31(1):149–153, 2013.

[27] Dmytro Afanasiev. Large-amplitude spin dynamics induced by femtosecond laser excitation in iron oxides. page 129, 2015.

[28] D. Grischkowsky, Søren Keiding, Martin van Exter, and Ch. Fattinger. Far-infrared time-domain spectroscopy with terahertz beams of dielectrics and semiconductors. *Journal of the Optical Society of America B*, 7(10):2006, 1990.

[29] José Vázquez-Cabo, Pedro Chamorro-Posada, Francisco Javier Fraile-Peláez, Óscar Rubiños-López, José María López-Santos, and Pablo Martín-Ramos. Windowing of THz time-domain spectroscopy signals: A study based on lactose. *Optics Communications*, 366(May):386–396, 2016.

[30] James Lloyd-Hughes and Tae In Jeon. A review of the terahertz conductivity of bulk and nano-materials. *Journal of Infrared, Millimeter, and Terahertz Waves*, 33(9):871–925, 2012.

[31] Martin Dressel and George Grüner. *Electrodynamics of Solids: Optical Properties of Electrons in Matter*. Cambridge University Press, 1st edition, 2002.

[32] Christopher Hakoda, Joseph Rose, Parisa Shokouhi, and Clifford Lissenden. Using Floquet periodicity to easily calculate dispersion curves and wave structures of homogeneous waveguides. *AIP Conference Proceedings*, 1949(April), 2018.

[33] Hu Tao, C. M. Bingham, A. C. Strikwerda, D. Pilon, D. Shrekenhamer, N. I. Landy, K. Fan, X. Zhang, W. J. Padilla, and R. D. Averitt. Highly flexible wide angle of incidence terahertz metamaterial absorber: Design, fabrication, and characterization. *Physical Review B - Condensed Matter and Materials Physics*, 78(24):2–5, 2008.

[34] Federico Sanjuan and Jorge O. Tocho. Optical properties of silicon, sapphire, silica and glass in the Terahertz range. *Latin American Optics and Photonics Technical Digest*, (3):LT4C.1, 2013.

[35] Kwok L. Chung, Xiaoqing Yan, Sarawuth Chaimool, Botao Feng, and Yingsong Li. On the surface susceptibilities and effective parameters of metasurfaces composed of isolated metallic unit-cells. *International Journal of RF and Microwave Computer-Aided Engineering*, 31(2):1–9, 2021.

[36] Philippe Gay-Balmaz and Olivier J.F. Martin. Electromagnetic resonances in individual and coupled split-ring resonators. *Journal of Applied Physics*, 92(5):2929–2936, 2002.

[37] Dibakar Roy Chowdhury, Ranjan Singh, Antoinette J. Taylor, Hou Tong Chen, Weili Zhang, and Abul K. Azad. Coupling schemes in terahertz planar metamaterials. *International Journal of Optics*, 2012, 2012.

[38] Abul K. Azad, Antoinette J. Taylor, Evgenya Smirnova, and John F. O'Hara. Characterization and analysis of terahertz metamaterials based on rectangular split-ring resonators. *Applied Physics Letters*, 92(1), 2008.

[39] T. Koschny, M. Kafesaki, E. N. Economou, and C. M. Soukoulis. Effective medium theory of left-handed materials. *Physical Review Letters*, 93(10):1–4, 2004.

[40] Harald Ditlbacher, Andreas Hohenau, Dieter Wagner, Uwe Kreibig, Michael Rogers, Ferdinand Hofer, Franz R. Aussenegg, and Joachim R. Krenn. Silver nanowires as surface plasmon resonators. *Physical Review Letters*, 95(25):1–4, 2005.

[41] R. W. Wood. Anomalous diffraction gratings. *Physical Review*, 48(12):928–936, 1935.

[42] Carsten Rockstuhl, Falk Lederer, Christoph Etrich, Thomas Zentgraf, Jürgen Kuhl, and Harald Giessen. On the reinterpretation of resonances in split-ring-resonators at normal incidence. *Optics Express*, 14(19):8827, 2006.

[43] P. Markoš and C. M. Soukoulis. Absorption losses in periodic arrays of thin metallic wires. *Optics Letters*, 28(10):846, 2003.

[44] A. Matulis, G. Šlekas, D. Seliuta, and Kancleris. The equivalent circuit imitating wave scattering by arrays of split-ring resonators. *Lithuanian Journal of Physics*, 59(2):57–69, 2019.

[45] John F. O'Hara, Ranjan Singh, Igal Brener, Evgenya Smirnova, Jiaguang Han, Antoinette J. Taylor, and Weili Zhang. Thin-film sensing with planar terahertz metamaterials: sensitivity and limitations. *Optics Express*, 16(3):1786, 2008.

[46] Hou Tong Chen, Willie J. Padilla, Joshua M.O. Zide, Arthur C. Gossard, Antoinette J. Taylor, and Richard D. Averitt. Active terahertz metamaterial devices. *Nature*, 444(7119):597–600, 2006.

[47] R. D. Averitt, W. J. Padilla, H. T. Chen, J. F. O'Hara, A. J. Taylor, C. Highstrete, M. Lee, J. M. O. Zide, S. R. Bank, and A. C. Gossard. Terahertz metamaterial devices. *Terahertz Physics, Devices, and Systems II*, 6772(May 2014):677209, 2007.

[48] Hou-Tong Chen, Willie J. Padilla, Joshua M. O. Zide, Seth R. Bank, Arthur C. Gossard, Antoinette J. Taylor, and Richard D. Averitt. Ultrafast optical switching of terahertz metamaterials fabricated on ErAs/GaAs nanoisland superlattices. *Optics Letters*, 32(12):1620, 2007.

[49] S. J. Park, S. A.N. Yoon, and Y. H. Ahn. Dielectric constant measurements of thin films and liquids using terahertz metamaterials. *RSC Advances*, 6(73):69381–69386, 2016.

[50] K. Meng, S. J. Park, A. D. Burnett, T. Gill, C. D. Wood, M. Rosamond, L. H. Li, L. Chen, D. R. Bacon, J. R. Freeman, P. Dean, Y. H. Ahn, E. H. Linfield, A. G. Davies, and J. E. Cunningham. Increasing the sensitivity of terahertz split ring resonator metamaterials for dielectric sensing by localized substrate etching. *Optics Express*, 27(16):23164, 2019.

[51] Erik Bründermann, Heinz Wilhelm Hübers, and Maurice Fitz Gerald Kimmitt. *Terahertz techniques*, volume 151. Springer, 2012.

[52] Ricardo Marqués, Francisco Mesa, Jesús Martel, and Francisco Medina. Comparative Analysis of Edge- and Broadside-Coupled Split Ring Resonators for Metamaterial Design - Theory and Experiments. *IEEE Transactions on Antennas and Propagation*, 51(10 I):2572–2581, 2003.

[53] C. H. Zhang, J. B. Wu, B. B. Jin, Z. M. Ji, L. Kang, W. W. Xu, J. Chen, M. Tonouchi, and P. H. Wu. Low-loss terahertz metamaterial from superconducting niobium nitride films. *Optics Express*, 20(1):42, 2012.

[54] Caihong Zhang, Biaobing Jin, Jiaguang Han, Iwao Kawayama, Hironaru Murakami, Jingbo Wu, Lin Kang, Jian Chen, Peiheng Wu, and Masayoshi Tonouchi. Terahertz nonlinear superconducting metamaterials. *Applied Physics Letters*, 102(8):1–5, 2013.

[55] Fusheng Ma, You Qian, Yu Sheng Lin, Hongwei Liu, Xinhai Zhang, Zhen Liu, Julius Ming-Lin Tsai, and Chengkuo Lee. Polarization-sensitive microelectromechanical systems based tunable terahertz metamaterials using three dimensional electric split-ring resonator arrays. *Applied Physics Letters*, 102(16), 2013.

[56] Fusheng Ma, Yu Sheng Lin, Xinhai Zhang, and Chengkuo Lee. Tunable multiband terahertz metamaterials using a reconfigurable electric split-ring resonator array. *Light: Science and Applications*, 3(December 2013):1–8, 2014.

[57] Thomas Cai Wei Tan, Eric Plum, and Ranjan Singh. Surface lattice resonances in THz metamaterials. *Photonics*, 6(3), 2019.

[58] Ruopeng Liu, Tie Jun Cui, Da Huang, Bo Zhao, and David R. Smith. Description and explanation of electromagnetic behaviors in artificial metamaterials based on effective medium theory. *Physical Review E - Statistical, Nonlinear, and Soft Matter Physics*, 76(2):1–8, 2007.

[59] Abdallah Dhouibi, Shah Nawaz Burokur, André de Lustrac, and Alain Priou. Study and analysis of an electric Z-shaped meta-atom. *Advanced Electromagnetics*, 1(2):64–70, 2012.

[60] Withawat Withayachumnankul, Christophe Fumeaux, and Derek Abbott. Near-field interactions in electric inductive-capacitive resonators for metamaterials. *Journal of Physics D: Applied Physics*, 45(48), 2012.

[61] Hong Min Lee and Hyung Sup Lee. Resonant mode behavior of lumped-resistor-loaded electric-inductive- capacitive resonator and its absorber application. *AIP Advances*, 3(5), 2013.

[62] H M Lee. Absorption Bandwidth-Enhanced Metamaterial Absorber Using In-planed ELC Resonator and Cut-Wire. *Electrical and Electronic Engineering*, 4(4):73–79, 2014.

[63] Ranjan Singh, Carsten Rockstuhl, and Weili Zhang. Strong influence of packing density in terahertz metamaterials. *Applied Physics Letters*, 97(24):1–4, 2010.

[64] Andreas Bitzer, Jan Wallauer, Hanspeter Helm, Hannes Merbold, Thomas Feurer, and Markus Walther. Lattice modes mediate radiative coupling in metamaterial arrays. *Optics Express*, 17(24):22108, 2009.

[65] Gwyn P. Williams. Filling the THz gap - High power sources and applications. *Reports on Progress in Physics*, 69(2):301–326, 2006.

[66] Z. M. Zhang, B.I. Choi, M. I. Flik, and A. C. Anderson. Infrared refractive indices of alkali halides. *Journal of Optical Society of America*, 11(11):2252–2257, 1994.

[67] S. Middey, J. Chakhalian, P. Mahadevan, J. W. Freeland, A. J. Millis, and D. D. Sarma. Physics of Ultrathin Films and Heterostructures of Rare-Earth Nickelates. *Annual Review of Materials Research*, 46:305–334, 2016.

[68] Weizheng Liang, Huaming Hou, Yuan Lin, and Sheng Nian Luo. Ultrafast electron and spin dynamics of strongly correlated NdNiO 3. *Journal of Physics D: Applied Physics*, 52(7):0753031–9, 2019.

[69] Sara Catalano. Electronic properties of NdNiO 3 and SmNiO 3 thin films. *PhD Thesis*, 2016.

[70] N. F. Mott. The basis of the electron theory of metals, with special reference to the transition metals. *Proceedings of the Physical Society. Section A*, 62(7):416–422, 1949.

[71] N. F. Mott. Metal-Insulator Transitions. *Pure and Applied Chemistry*, 52(1):65–72, 1980.

[72] Sara Catalano, M. Gibert, J. Fowlie, J. Íñiguez, J. M. Triscone, and J. Kreisel. Rare-earth nickelates R NiO 3 : thin films and heterostructures. *Reports on Progress in Physics*, 81(046501):1–28, 2018.

[73] A. D. Caviglia, R. Scherwitzl, P. Popovich, W. Hu, H. Bromberger, R. Singla, M. Mitrano, M. C. Hoffmann, S. Kaiser, P. Zubko, S. Gariglio, J. M. Triscone, M. Först, and A. Cavalleri. Ultrafast strain engineering in complex oxide heterostructures. *Physical Review Letters*, 108(13):1368011–1368015, 2012.

[74] Raoul Scherwitzl, Pavlo Zubko, I. Gutierrez Lezama, Shimpei Ono, Alberto F. Morpurgo, Gustau Catalan, and Jean Marc Triscone. Electric-field control of the metal-insulator transition in ultrathin NdNiO3 films. *Advanced Materials*, 22(48):5517–5520, 2010.

[75] G. Catalan, R. M. Bowman, and J. M. Gregg. Metal-insulator transitions in NdNiO3 thin films. *Physical Review B - Condensed Matter and Materials Physics*, 62(12):7892–7900, 2000.

[76] G. Mattoni, P. Zubko, F. Maccherozzi, A. J.H. Van Der Torren, D. B. Boltje, M. Hadjimichael, N. Manca, S. Catalano, M. Gibert, Y. Liu, J. Aarts, J. M. Triscone, S. S. Dhesi, and A. D. Caviglia. Striped nanoscale phase separation at the metal-insulator transition of heteroepitaxial nickelates. *Nature Communications*, 7(April 2018), 2016.

[77] Xingquan Zou, Mi He, Daniel Springer, Dongwook Lee, Saritha K. Naiz, Siew Ann Cheong, Tom Wu, C. Panagopoulos, D. Talbayev, and Elbert E.M. Chia. Effect of annealing on the temperature-dependent dielectric properties of LaAlO3 at terahertz frequencies. *AIP Advances*, 2(1), 2012.

[78] Jiaguang Han, Boon Kuan Woo, Wei Chen, Mei Sang, Xinchao Lu, and Weili Zhang. Terahertz dielectric properties of MgO nanocrystals. *Journal of Physical Chemistry C*, 112(45):17512–17516, 2008.

[79] Giordano Mattoni. *Metal–Insulator Transitions in Heterostructures of Quantum Materials*. 2017.

[80] P. H. Xiang, N. Zhong, C. G. Duan, X. D. Tang, Z. G. Hu, P. X. Yang, Z. Q. Zhu, and J. H. Chu. Strain controlled metal-insulator transition in epitaxial NdNiO3 thin films. *Journal of Applied Physics*, 114(24):2437131–2437135, 2013.

[81] Adam J. Hauser, Evgeny Mikheev, Nelson E. Moreno, Jinwoo Hwang, Jack Y. Zhang, and Susanne Stemmer. Correlation between stoichiometry, strain, and metal-insulator transitions of NdNiO3 films. *Applied Physics Letters*, 106(9):0–5, 2015.

[82] P. C. Canfield, J. D. Thompson, S. W. Cheong, and L. W. Rupp. Extraordinary pressure dependence of the metal-to-insulator transition in the charge-transfer compounds NdNiO3 and PrNiO3. *Physical Review B*, 47(18):12357–12360, 1993.

[83] Mengkun Liu, Harold Y. Hwang, Hu Tao, Andrew C. Strikwerda, Kebin Fan, George R. Keiser, Aaron J. Sternbach, Kevin G. West, Salinporn Kittiwatanakul, Jiwei Lu, Stuart A. Wolf, Fiorenzo G. Omenetto, Xin Zhang, Keith A. Nelson, and Richard D. Averitt. Terahertz-field-induced insulator-to-metal transition in vanadium dioxide metamaterial. *Nature*, 487(7407):345–348, 2012.

[84] J. Zaanen, G. A. Sawatzky, and J. W. Allen. Band Gaps and Electronic Structure of Transition-Metal Compounds. *Physical Review Letters*, 55(4):418–421, 1985.